Copyright 2015 Garrett J. Pataky

ADVANCED EXPERIMENTAL MEASUREMENTS OF HETEROGENEOUS STRAIN AND TEMPERATURE CHANGE IN METALS

BY

GARRETT JAMES PATAKY

DISSERTATION

Submitted in partial fulfillment of the requirements
for the degree of Doctor of Philosophy in Mechanical Engineering
in the Graduate College of the
University of Illinois at Urbana-Champaign, 2015

Urbana, Illinois

Doctoral Committee:

Professor Huseyin Sehitoglu, Chair and Director of Research
Professor Petros Sofronis
Professor Elif Ertekin
Professor John Lambros

Abstract

This work investigates elevated temperature deformation in the nickel-based superalloy Haynes 230 and elastocaloric cooling in shape memory alloys. Three loading conditions were examined in the elevated temperature portion: fatigue crack growth, creep, and tension. Measurements were made on varying length scales using digital image correlation depending on the intended purpose of the study. The elastocaloric cooling study examines the temperature change in the reverse martensitic transformation utilizing infrared thermography and digital image correlation.

The fatigue crack growth of Haynes 230 was investigated at room temperature and 900 °C using digital image correlation. As expected, the crack growth rates at high temperature were much faster than at room temperature. However, the crack closure levels, which were determined using digital image correlation analysis techniques, were found to be similar for the two cases studied. DIC strain fields and the corresponding plastic zone sizes were compared between the two cases. From these strain fields, the slip irreversibility, the difference between forward and reversed strains at the crack tip, was quantitatively measured. The high temperature case had an order of magnitude higher amount of slip irreversibility. Slip irreversibility measurements were determined to be an effective method to compare fatigue crack growth of cases with differing temperatures.

Creep was studied in Haynes 230 at 800 °C and 900 °C. This study focused on the differences in the creep mechanisms and damage at the two temperatures. Using the microstructure, grain boundary serrations and triple junction strain concentrations were quantitatively identified. There was significant damage in the 900 °C samples and the creep was almost entirely tertiary. In contrast, the 800 °C sample exhibited secondary creep. Using an Arrhenius equation, the minimum creep rate exponents were found to be $n \approx 3$ and $n \approx 5$ for 900 °C and 800 °C respectively. The creep mechanisms were identified as solute drag for $n \approx 3$ and dislocation climb for $n \approx 5$. Strain concentrations were identified at triple junctions and grain boundary serrations using high resolution digital image correlation overlaid on the

microstructure. The grain boundary serrations restrict grain boundary sliding which may reduce the creep damage at triple junctions and extend the creep life of Haynes 230 at elevated temperatures.

An experimental methodology has been developed to study materials deformed at high temperatures using high resolution *ex-situ* digital image correlation. This study is an advancement of techniques that have used sub-grain level strain measurements and linked them to microstructural data obtained with electron back-scatter diffraction. The approach utilized air blasting particles that were capable of remaining unchanged onto a sample surface and loading the sample at elevated temperatures in vacuum to prevent oxidation. Two tensile experiments were performed at temperatures of 700 °C and 800 °C on Haynes 230 using digital image correlation at high magnifications in order to study the heterogeneous strain fields. Overlaying the strain fields and microstructure data, global trends and areas of high strain were studied. This study represents an advancement of the usefulness of high resolution digital image correlation by expanding the loading conditions that can be studied and provided experimental results to further physics-based modeling.

Solid state elastocaloric cooling, the endothermic reversible martensitic phase transformation in shape memory alloys, has the potential to replace vapor compression refrigeration. NiTi, Ni_2FeGa, and CoNiAl shape memory alloys were experimentally investigated to measure the magnitude of temperature change using thermography during uniaxial tensile experiments. Consecutive tensile cycles were also performed, and they revealed a symmetric temperature profile between the two cycles. The unique, dual camera technique of digital image correlation and infrared thermography was utilized to track the transformation bands and temperature gradients to gain insight about the unloading, endothermic process. Fatigue implications, elevated temperature environments, and the theoretical maximum temperature based on entropy change were discussed.

Acknowledgements

I would like to thank the people who have supported me during my graduate studies at the University of Illinois. First I would like to thank my advisor, Prof. Huseyin Sehitoglu. During my time here he has been continuously supportive, even during the times when performing certain experiments have been extreme uphill battles. He has graciously shared his wealth of knowledge and his eagerness to conduct research has been truly inspiring. His advice has helped me expand my understanding of material behavior and grow into the researcher I have become. I am deeply grateful for all the time he has spent encouraging and teaching me.

I would also like to thank my committee members. Prof. Petros Sofronis was an exceptionally challenging instructor but presented the material beautifully and inspired me to throw myself into the world of solid mechanics. I appreciate Prof. John Lambros for his useful discussions and feedback on experimental mechanics. Thank you to Prof. Elif Ertekin for broadening my understanding of vibrations and opening my eyes to the usefulness of quantum mechanics.

A very sincere thank you goes to Peter Kurath, Gavin Horn, and Rick Rottet. The amount of time these three spent diagnosing and fixing equipment issues probably saved me from at least a year's worth of frustration and tinkering. I've grown to think that Peter has a secret magic wrench for whacking the load frames to put everything back in order. Gavin was instrumental in setting up a space for me in AMTEL and training me on the infrared camera used in the shape memory alloy study. He always made a few minutes to answer my questions despite his busy schedule. I would also like to thank the machine shop (Keith Parrish, Cliff Gulyash, Kyle Cheek, and Gary Sedberry) for their quick turnaround on requested parts and samples to keep my research moving. I appreciated the time that Dr. Stephen Downing spent with me during my semester teaching and helping me grow as an instructor. Thank you to Prof. Dr.-Ing Hans Maier for his extremely beneficial microscopy and detailed description of micrographs.

I also appreciate the time I've shared with the people I've seen every day: my labmates. A big thank you goes out to Reggie Hamilton for quickly bringing me up to speed on experimental techniques. Jay Carroll was always patient and willing to talk through research issues to grind towards the solution. Those discussions and the ones we still have today are fruitful, and I always appreciate them. Thanks to Wael Abuzaid for helping me strategize and talking about games and the world when breaks were needed. Piyas Chowdhury always provided me an opportunity to learn about the simulation side of our world. Thank you to Mallory Casperson for always being so cheerful and introducing me to my fiancée. Thank you to Luca Patriarca for his humor and model of hard working. I also thank the others who I have had the pleasure to work with: Yan Wu, Sertan Alkan, Avinesh Ojha, Alpay Oral, Emanuele Sgambitterra, Silvio Rabbolini, Pietro Giovanni, Mike Sangid, Tawhid Ezaz, and Jifeng Wang.

I would like to acknowledge the financial support for my studies. The support from the Department of Energy's Nuclear Energy University Program allowed for all the Haynes 230 work to be possible. The National Science Foundation allowed me to expand into the world of shape memory alloys and study their unique behavior.

I have to thank my parents Gloria and Henry Pataky for their unrelenting love. They have always been encouraging and inquisitive of my work. Their motivating words have gotten me through the tough times and their constant support is always felt. I also thank my sister Stephanie for her laughter, phone calls, and words of wisdom. I am also very thankful for my fiancée Emily Ward. Her patience, understanding, and support have been immeasurable. Her smile has an incessantly soothing presence and has helped me overcome my most stressed moments. Oh, and thanks to my dog Blue for always being willing to play with me in the snow!

Table of Contents

List of Figures ix
List of Tables xii
Chapter 1. Introduction 1
1.1 Motivation 1
1.2 Methodology and Materials 4
1.2.1 Digital Image Correlation 5
1.2.1.1 In-situ DIC 6
1.2.1.2 Ex-situ DIC 6
1.2.2 Materials 7
1.2.2.1 Haynes 230 7
1.2.2.2 NiTi 10
1.2.2.3 Ni_2FeGa 10
1.2.2.4 CoNiAl 10
1.3 Objectives 11
1.4 Thesis Outline 12
1.5 References 13
Chapter 2. High Temperature Fatigue Crack Growth in Haynes 230 15
2.1 Background 15
2.2 Material Preparation and Experimental Procedure 17
2.2.1 Material Preparation 17
2.2.2 Experimental Procedure 18
2.3 Results 20
2.3.1 Fatigue Crack Growth 20
2.3.2 Slip Irreversibility 23
2.3.3 Scanning Electron Microscope and Transmission Electron Microscopy Analysis 26
2.4 Discussion 29
2.4.1 Crack Closure Effects 29
2.4.2 Slip Irreversibility 30
2.5 Summary 32
2.6 References 32
Chapter 3. Creep of Haynes 230 at 800 °C and 900 °C 36
3.1 Background 36
3.2 Material Preparation and Experimental Procedure 38
3.2.1 Material Preparation 38

3.2.2 Experimental Procedure 38
3.3 Results 40
3.3.1 Creep Results 40
3.3.2 SEM of Crept Material 43
3.4 Discussion 45
3.4.1 Grain Boundary Serrations and Triple Junctions 45
3.4.2 Creep Exponents 49
3.5 Summary 50
3.6 References 51
Chapter 4. Elevated Temperatures *ex-situ* Procedure 53
4.1 Background 53
4.2 Sample Preparation 54
4.3 Experimental Procedure 56
4.3.1 Magnifications and Image Capture 57
4.3.2 Vacuum and Loading Procedure 57
4.3.3 Stitching and Aligning DIC and EBSD 59
4.4 Measurement Error 61
4.5 References 62
Chapter 5. Incremental Tensile Experiments 64
5.1 Experimental Details 64
5.2 Results and Discussion 66
5.2.1 800 °C Tensile Experiment 66
5.2.2 700 °C Tensile Experiment 70
5.3 Summary 77
5.4 References 77
Chapter 6. Shape Memory Alloy Elastocaloric Cooling. 78
6.1 Background 78
6.2 Experimental Details 81
6.2.1 Materials 81
6.2.2 Preparation and Experimental Procedure 81
6.3 Results 82
6.3.1 Stress-Strain Response 82
6.3.2 Temperature Change 83
6.3.3 Temperature Change and Strain Relationship 85
6.3.4 Transformation Bands 86
6.4 Discussion 89

6.4.1 Fatigue Considerations for Elastocaloric Cooling 89
6.4.2 Theoretical Temperature Change Considerations 90
6.4.3 Ambient Temperature Impact 93
6.5 Summary 94
6.6 References 94
Chapter 7. Conclusions and Future Work 96
7.1 Conclusions 96
7.2 Future Work 98
Appendix: Least Squares Regression 101

List of Figures

Fig. 1.1 - History of world primary energy use 1

Fig. 1.2 - Schematic of the VHTR. The intermediate heat exchanger, where outlet temperatures will reach up to 1000 °C, is circled in red. 2

Fig. 1.3 - Schematics demonstrating magnetocaloric cooling. A magnetic field causes the aligning of spins and a rise in temperature. Removal of this magnetic field induces a large temperature drop upon disordering of the spins. 4

Fig. 1.4 - a) A section of the Haynes 230 grain orientation map obtained from EBSD. b) The CSL boundary frequency for the 0.39 mm^2 area scanned showing a high percentage of $\sum 3$ boundaries. 8

Fig. 1.5 - Schematic of the dog-bone specimen geometry. 8

Fig. 1.6 - Stress-strain data for Haynes 230 at room temperature, 700 °C, 800 °C, and 900 °C. 9

Fig. 2.1 - A schematic of a fatigue crack with plasticity-induced crack closure in the crack wake and slip irreversibility at the crack tip. The shaded grey region in the inset provides a measure of the irreversible slip strain (or irreversible displacements). 16

Fig. 2.2 - Microstructure of the as-received Haynes 230 material showing annealing twins and a wide range of grain sizes. 18

Fig. 2.3 - The crack growth rate as a function of the stress intensity factor range for room temperature (RT) and 900 °C experiments. The insets are displacement contour plots showing the experimental (blue) and regression (red) vertical displacements in increments of 1 micron with the black dot indicating the crack tip location. 21

Fig. 2.4 - A comparison between the local (digital extensometer) and full-field (regression) crack opening levels for the RT specimen at a crack length of 0.994 mm and the HT specimen at a crack length of 0.964 mm. Symbols represent the digital extensometer values at various points along the crack while lines represent the regression found value for the full-field. The schematic depicts the digital extensometer technique and placement along the crack flanks. 23

Fig. 2.5 - Plots of vertical displacement contours and plastic zones for a selected a) room temperature and b) 900 °C fatigue crack cycle. Blue contours represent the experimental DIC displacements and red contours represent the regression found displacement contours. a) At a crack length of 0.994 mm, the room temperature specimen had a ΔK value of 22.64 MPa$\sqrt{m}$, a regression found ΔK_{eff} value of 16.55 MPa$\sqrt{m}$, and a plastic zone radius of 0.337 mm. b) At a crack length 0.964 mm, the 900 °C specimen had a ΔK value of 14.08 MPa$\sqrt{m}$, a regression found ΔK_{eff} value of 9.39 MPa$\sqrt{m}$, and a plastic zone radius of 0.666 mm. 24

Fig. 2.6 - Strain irreversibility as a function of the maximum stress intensity factor during the fatigue crack growth experiments. The schematic shows the two minimum load points (A and B) where the strain measurements were taken. DIC strain plots for both the room temperature and 900 °C experiments are shown and the higher strains in the B plots compared to the A plots indicated irreversible strains during the fatigue cycle. 26

Fig. 2.7 - a) A high magnification SEM micrograph showing the fatigue striations on the 900 °C specimen. b) The post-fracture surface of the 900 °C specimen showing a low level of oxidation and a smooth surface indicative of intragranular fatigue crack growth. 27

Fig. 2.8 - Planar slip in the Haynes 230 material. 28

Fig. 2.9 - An SEM micrograph showing the heterogeneity in Haynes 230. A stacking fault separates areas of low carbide density and high carbide density. The cutout shows a dense area of carbide-dislocation interactions. 28

Fig. 3.1 - The experimental setup. A - Specimen in the load frame, B - Induction coils, C - Type-K thermocouple, D – White Light Illumination, E - Lens and Camera. 39

Fig. 3.2 - Strain versus time data for creep tests of Haynes 230 at 800 °C and 900 °C at several load levels. Steady state creep is more readily observed in the 800 °C samples while both temperatures show localized strains greater than 30%. 41

Fig. 3.3 – Axial strain magnitudes as a function of distance found at serrated grain boundaries and triple junctions. The red dot in the schematics shows the 0 μm measurement point for a) triple junctions and b) serrated grain boundaries. 42

Fig. 3.4 - The minimum creep rate plotted as a function of the applied loading for creep of Haynes 230. The creep at 800 °C corresponds to a creep exponent of $n \approx 5$ (dislocation climb mechanism) and the 900 °C results produce a creep exponent of $n \approx 3$ (solute drag mechanism). 43

Fig. 3.5 - SEM micrographs of the fracture surface from samples crept at 900 °C. a) Intergranular cracking and voids are evident. b) A cracked triple junction on the fracture surface. 44

Fig. 3.6 - SEM micrographs of the fracture surface and a secondary crack from a sample crept at 800 °C. a) The fracture surface of the sample showing high levels of ductility and a mixture of intergranular and transgranular cracking. b) A secondary crack below the failed section showing intergranular cracking. . 44

Fig. 3.7 - DIC axial strain field (average strain of 0.26%) after 2 hours of creep at 900 °C with a load of 50 MPa overlaid on an optical micrograph of the microstructure at a magnification of 10x. Two areas of localized strain were observed: on a serrated grain boundary and at the triple junction of a twin and two grain boundaries. 46

Fig. 3.8 - DIC axial strain field (average strain of 0.88%) after 10 hours of creep at 900 °C with a load of 50 MPa overlaid on an optical micrograph of the microstructure at 10x. High levels of localized strain were found at a triple junction and a serrated grain boundary. 47

Fig. 3.9 - A TEM micrograph from a sample crept at 900 °C at a stress of 100 MPa showing dislocation-carbide interactions with carbides present in the boundary. The carbides in the grain boundary are the cause of serrated grain boundaries. 48

Fig. 3.10 - A TEM micrograph showing a subgrain formed during creep at 800 °C at a stress of 75 MPa. 50

Fig. 4.1 - Speckle patterns of air blasted a) Si particles (10x magnification) and b) alumina particles (25x magnifications) before heating taken using an optical microscope. c) The pattern with the Si particles changed drastically after being heated to 800 °C while the d) alumina particle pattern remained consistent with the unheated pattern. 56

Fig. 4.2 - A picture of the experimental setup showing: A – load cell, B – vacuum chamber, C – type-K thermocouple, D – induction heating coils, and E – grips where specimen was placed. The additional copper coiling is to provide cooling during the experiments at elevated temperatures. The inset shows the specimen glowing while heated in the sealed vacuum chamber. 59

Fig. 5.1 - A schematic of the dog-bone specimen with the location of the area studied defined by the Vickers indentation marks. The EBSD scan results showing grain orientations of the 700 °C sample with the Vickers marks accentuated. 65

Fig. 5.2 - Images from the optical microscope showing the 0.6 mm by 0.6 mm area and speckle patterns of the sample tested at 800 °C a) undeformed and b) after the first step of heating and deformation at a

magnification of 25x with the Vickers indentation marks visible. c) The ε_{yy} strain field found using DIC. The white arrows in c) show high strained areas that crack in the next deformation step (shown in Fig. 5.3c). 67

Fig. 5.3 - a) and b) Images taken with the optical microscope depicting the lack of focus in certain areas of each image. c) The combined image created using the images in a) and b) and eliminating the out of focus regions. d) The ε_{yy} strain field found using DIC with cracks on the sample showing strain magnitudes of 15% or greater. The red box is the region correlated using the image in c). The white arrows in c) show cracked regions that were the highly strained areas in the previous deformation step.. 69

Fig. 5.4 - a) The stress-strain response of Haynes 230 experimented at 700 °C with the 10 steps of deformation indicated when the experiment was halted to image for DIC. The ε_{yy} strain field of the 1.05 mm by 0.525 mm area studied with the grain and twin boundaries overlaid at mean strains of a) 1.22%, b) 1.59%, and c) 2.51%. Note the scale bar changes for each strain field. 71

Fig. 5.5 - a) Histogram of the ε_{yy} strain values for four deformation steps showing the increasing strain values. b) The trends of the minimum, maximum, and mean values of the ε_{yy} strain field. c) The standard deviation of the ε_{yy} strain field showing an increasing heterogeneity in the strain field..... 73

Fig. 5.6 - a) Slip system 7 and b) slip system 8 shear increments after deformation step 4. The dark blue areas are where the system has not been activated. a) Slip transmission between a grain and twin is depicted in the magnified box. b) Blockage of slip from the grain to the twin is shown in the magnified box. See Table 5.1 for the Schmid factor values..... 76

Fig. 6.1 – A schematic of the elastocaloric cooling effect. Upon loading, austenite (grey on the specimen) is transformed into stress-induced martensite (black on the specimen) and a rise of temperature is measured. Upon removal of the stress, the material returns to the austenite phase with a simultaneous large temperature drop. 78

Fig. 6.2 - Tensile stress-strain curves for the shape memory alloys 83

Fig. 6.3 - Temperature change, ΔT, of each experiment for each material..... 84

Fig. 6.4 - Temperature versus time plots for the a) [011] oriented Ni_2FeGa specimen and b) [148] oriented NiTi specimen. c) Schematic describing the experiment of two consecutive cycles with a hold period between tensile cycles..... 85

Fig. 6.5 - The temperature change, ΔT, as a function of maximum tensile strain. The inset shows the stress-strain curves for maximum strains of 8.35% and 10% 86

Fig. 6.6 - Tensile stress-strain curves of the a) [011] oriented Ni_2FeGa specimen and b) [112] oriented NiTi specimen with selected DIC strain fields and temperature gradient of the gage section. c) During the reverse martensitic transformation in the [148] NiTi single crystal, the transformation band edges corresponded to a localized undercooling as indicated by the dotted black lines. d) Schematic of the two camera setup with the DIC camera in front and the IR camera behind the sample. 88

Fig. 6.7 - Critical stress (0.1% strain) as a function of temperature used to find the Clausius-Clapeyron slopes. 91

List of Tables

Table 1.1 - Magnifications and corresponding measurement resolutions 6

Table 1.2 – Chemical composition (wt%) of the Haynes 230 sheet studied. 8

Table 2.1 - Paris law coefficients for Haynes 230 at RT and 900 °C (da/dN in mm/cycle and ΔK in MPa√m). 21

Table 3.1 - Creep constants summary of Haynes 230 43

Table 4.1 - A comparison of the DIC mean ε_{yy} strain values over the entire area of interest correlated to each of the two 10x magnification reference images. 62

Table 5.1 - Schmid factors for the 12 slip systems of the grain and twin shown in Fig. 5.7. 75

Table 6.1 - ΔT_{th} calculated using the Clausius-Clapeyron slope 92

Table 6.2 - ΔT_{th} calculated using the enthalpy change during transformation 93

Chapter 1. Introduction

1.1 Motivation

The rapidly increasing worldwide demand for energy and the current reliance on fossil fuels has created the necessity for innovative energy solutions. China increased its total energy consumption by 159% from 1,161 Mtoe in 2000 to 3,013 Mtoe in 2013 while India's total energy consumption grew by 80% in the same time period [1]. A majority of energy produced today is still exhaustible fossil fuels as indicated in Fig. 1.1. Energy infrastructures depend on reliable, accessible sources of energy in order to consistently accommodate the needs of consumers and the economy.

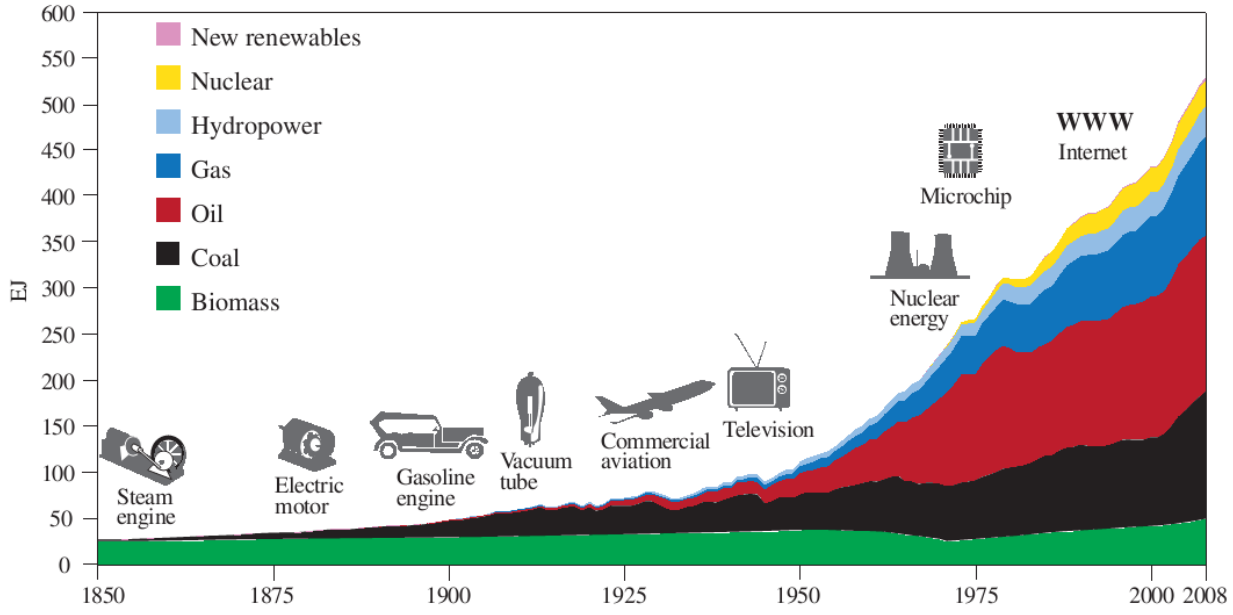

Fig. 1.1 - History of world primary energy use [2]

The U.S. follows this same trend of reliance on fossil fuels. In 2008, energy consumption was comprised of approximately 40% of liquid fuels and 46% of natural gas and coal with the other 14% being divided between nuclear power and renewable energies. At a rate of approximately 9 million barrels of crude oil a day, a large amount of the liquid fuel was imported [3]. This high reliance on

foreign sources for energy can create volatility in the economy if prices become unpredictable due to international crises or political instability. This has led to the renewed interests in nuclear energy, especially if the additional benefit of hydrogen production is achieved.

The Generation-IV (Gen-IV) initiative was established in 2000 as a cooperative international research and development program to work towards the next generation of nuclear reactors. The goals of Gen-IV are sustainability, safety, reliability, economic, and proliferation resistance. The High Temperature Gas Reactor (HTGR) has been identified as the prototype for the Next Generation Nuclear Plant (NGNP). The production of hydrogen requires high temperatures, thus the Very High Temperature Reactor (VHTR) is a leading candidate design. Specifically, the intermediate heat exchanger (IHX), circled in Fig. 1.2, is planned to have outlet temperatures up to 1000 °C [4].

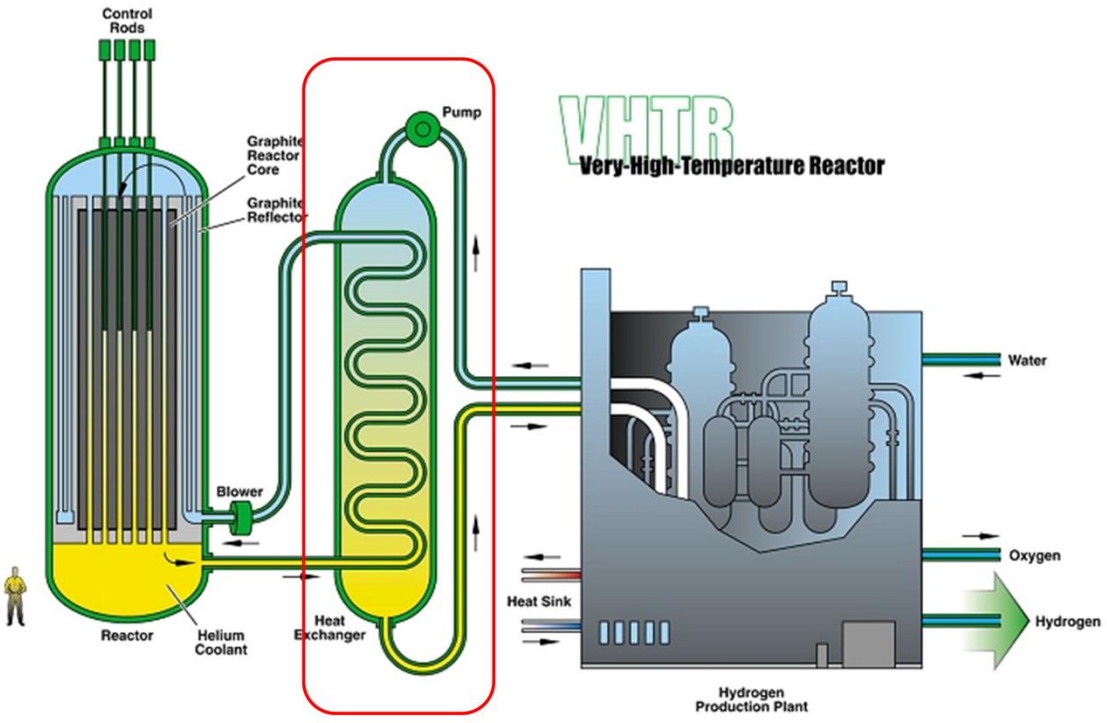

Fig. 1.2 - Schematic of the VHTR. The intermediate heat exchanger, where outlet temperatures will reach up to 1000 °C, is circled in red.

These extremely elevated temperatures will put a large demand on the materials employed. For the IHX, nickel-based superalloys are the leading candidate materials. Haynes 230, a focus of this thesis,

is one of the candidate materials being considered. A current issue in the development of the VHTR is the lack of an ASME code covering the nuclear service of Haynes 230. Other superalloys being considered (Alloy 800H and Alloy 617) currently have the same issue, as the code is nonexistent or rated below the operational temperatures of the VHTR [5]. In order to receive serious consideration for service, material characterization must be undertaken. In addition, furthering the scientific communities' understanding of local deformation with respect to the microstructure can assist the development of physics-based models to predict material behavior at elevated temperatures.

A second concern with the abundant usage of fossil fuels is the amount of greenhouse gases (GHGs) produced. To prevent further climate change, GHG emissions must be reduced. The U.S. accounts for approximately 33% of worldwide GHGs. An increase of nuclear power will help alleviate some of the energy sector produced emissions, but hydrofluorocarbons (HFCs) still represent a serious challenge.

HFCs are regularly used as refrigerants in vapor compression cooling systems. Although not ozone depleting, HFCs have a high global warming potential (GWP). The GWP indicates how much a chemical will contribute to global warming compared to the same mass of carbon dioxide. Their impact is so large that they are commonly referred to as "super greenhouse gases". One such example is the common HFC-134a which has a GWP of 1,430 (100-year) [6]. The Montreal Protocol has had a significant impact by phasing out chlorofluorocarbons (CFCs) and hydrochlorofluorocarbons (HCFCs), but the progression from these to HFCs indicates the need to explore other refrigerants.

Materials have been recognized since the 1850s as having the potential to undergo thermal changes as a response to an applied field [7]. Magnetocaloric solid state refrigeration was proposed in the 1970s to take advantage of the magnetocaloric effect (MCE) [8]. The MCE is when an applied magnetic field causes a reversible thermal change, but significant issues persist limiting its performance [9]. Normally a material exhibits disordered magnetic spins. When a ferromagnetic material is exposed to a magnetic field, the magnetic spins align and a temperature increase occurs. Upon removal of this

magnetic field, a large temperature change is achieved due to the entropy change. A schematic demonstrating MCE is given in Fig. 1.3. Elastocaloric cooling has emerged as an alternative solid state refrigeration solution without the necessity of a large magnetic field.

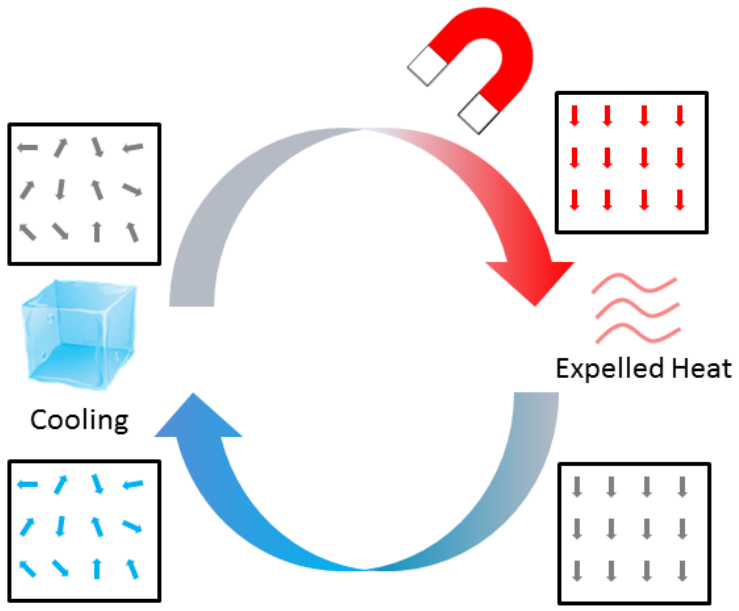

Fig. 1.3 - Schematics demonstrating magnetocaloric cooling. A magnetic field causes the aligning of spins and a rise in temperature. Removal of this magnetic field induces a large temperature drop upon disordering of the spins.

The phase transformation present in shape memory alloys (SMAs) during deformation produces a temperature change due to the entropy change. The temperature change during the reverse martensitic transformation is of particular interest since it is an endothermic reaction. Elastocaloric cooling is currently in its infancy, thus a large amount of work will need to be devoted to fully exploit this phenomenon. Solid state refrigeration represents an environmentally friendly alternative to vapor compression systems and the resulting reduction of GHGs can be significant.

1.2 Methodology and Materials

Digital image correlation (DIC) was used extensively throughout this work. This section will elaborate on the DIC technique and discuss the differences between the *in-situ* and *ex-situ* techniques employed. The four metals studied will also be introduced.

1.2.1 Digital Image Correlation

DIC is a non-contacting, optical technique which relies on tracking light intensities to compare a deformed image to a reference image. The reference image is typically of the undeformed state, but this is not necessary. In order to properly track the displacements, there must be a variance in the pixel light intensities on the surface [10]. The specimen surface itself may be used, but speckles are usually applied to the surface for a more consistent, uniform pattern. A grid method has been employed by several researchers [11-14], but a random pattern has been shown to perform better. Individually, a single pixel's intensity is not unique, requiring the breaking up of the pattern into discrete sub-regions.

The sub-regions used in DIC are referred to as subsets. A subset is a square group of pixels which create a unique pattern. The subset sizes and spacing are user-defined. A higher quality speckle pattern will permit the use of a smaller subset size, increasing the resolution of the correlation. As a 2-D technique, which was used in this work, horizontal and vertical displacements will be measured by the correlation. The tracking and optimization algorithms are given in detail in [10]. Depending on the subset size, a full-field image is usually broken down into thousands of subsets, and thus thousands of displacements are measured. Strain fields can then be calculated through differentiation. This provides a wealth of information for studying both full-field and local deformation. The versatility of DIC means that it can be used at different magnifications for multiscale measurements (a higher magnification yields a higher measurement resolution but a reduced field of view) and in a variety of environments (vacuum, high temperature, etc).

The same DIC equipment was used throughout this work. An IMI-202FT digital camera was used to capture images during the experiments. The camera resolution was 1600 pixels by 1200 pixels, and the maximum frame rate was 15 fps. For *in-situ*, an adjustable lens with a 12x magnification range and 2x adapter was used to achieve different magnifications. For *ex-situ*, the camera was attached to an Olympus BX51M optical microscope. The four camera magnifications in this study range from 1.5x to 25x, with the measurement resolution increasing with higher magnifications. The corresponding

resolutions to each magnification are given in Table 1.1 including the corresponding measurement method.

Table 1.1 - Magnifications and corresponding measurement resolutions

Magnification	Resolution (µm/pix)	Method
1.5x	2.95	*in-situ*
2.35x	1.85	*in-situ*
10x	0.437	*ex-situ*
25x	0.175	*ex-situ*

1.2.1.1 In-situ DIC

To study a material while it is being loaded, an *in-situ* DIC method is used. Since the images are captured during deformation, lower magnifications typically work best. This is due to the sensitivity of higher magnifications to blur with any movement. *In-situ* magnifications typically range from 2x to 5x, but other studies have included higher magnifications up to 10x [15]. This method of DIC is conducted by setting the DIC equipment on a tripod in front of the load frame and focusing on the sample.

The benefits of capturing full-field deformations during loading are numerous. For the case of fatigue crack growth, the capturing of images during a fatigue cycle provides the opportunity to determine the crack closure level. This is a case where the reference image would not be of the undeformed state. For a loading condition such as creep, *in-situ* is necessary to determine the creep strains as cooling and then reheating can have an effect on the material behavior.

1.2.1.2 Ex-situ DIC

The *ex-situ* method employed in this work is performed with an optical microscope after interrupting the experiment. By utilizing a microscope, images at 10x and 25x can be obtained. This is crucial for obtaining sub-grain measurement resolution. When used in conjunction with microstructural information, conclusions can be made about the influence of slip, grain boundaries, twin boundaries, and precipitates.

The limiting factor of the higher magnification images is the field of view. The *ex-situ* measurements require capturing multiple images in order to cover the entire region of interest. Previous high resolution studies have defined a repeatable technique in order to perform these experiments and stitch together the full-field information [16]. The study performed by Carroll *et al.* also defined a criterion for successful sub-grain level measurements: approximately one fourth the grain diameter [16]. Expounded on in Section 1.2.2.1, the average grain diameter of Haynes 230 is 50 μm. This verifies that both the 10x and 25x magnifications will be sub-grain level measurements.

1.2.2 Materials

Four materials were studied in this thesis. The nickel-based superalloy Haynes 230 was the focus of the elevated temperature work. The three SMAs utilized as possible solid-state refrigerants were NiTi, Ni_2FeGa, and CoNiAl. Details about each material are provided below.

1.2.2.1 Haynes 230

The nickel-based superalloy Haynes 230 was deemed a candidate material for the IHX in the Gen-IV initiative. Commercially available Haynes 230 was used in this work. Haynes 230 is a solid-solution strengthened alloy developed for high temperature applications. It has additions of chromium, tungsten, and molybdenum with a full chemical composition given in Table 1.2. The microstructure of the plate utilized in this study had a wide range of grain sizes, from 30 μm to 250 μm. Using the lineal intercept method, as outline lined in ASTM E-112, the average grain size was found to be about 50 μm. A large amount of annealing twins was observed in the material. Electron back-scatter diffraction (EBSD) was performed on an area of approximately 0.39 mm^2 to obtain statistical information. A portion of the EBSD data is shown in Fig. 1.4a. Fig. 1.4b has a histogram of the coincident lattice notation (CSL) grain boundary types for the entire area scanned. 573 out of the 1249 grain boundaries were described using the CSL criterion and almost two-thirds were Σ3 boundaries.

Table 1.2 – Chemical composition (wt%) of the Haynes 230 sheet studied.

Al	B	C	Co	Cr	Cu	Fe	La	Mn
0.35	0.005	0.1	0.16	22.14	0.04	1.14	0.015	0.5
Mo	Ni	P	S	Si	Ti	W	Zr	
1.25	bal	0.005	0.002	0.49	0.01	14.25	0.01	

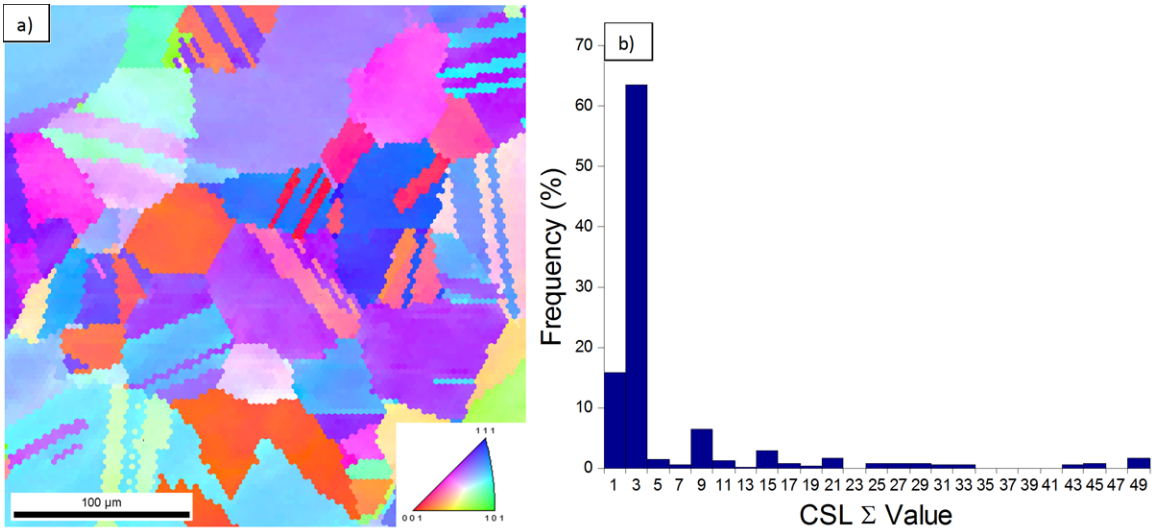

Fig. 1.4 - a) A section of the Haynes 230 grain orientation map obtained from EBSD. b) The CSL boundary frequency for the 0.39 mm^2 area scanned showing a high percentage of ∑3 boundaries.

The Haynes 230 sheet received was 2.38 mm (3/32”) thick, and dog-bone specimens were electrical discharge machined (EDM) with a gauge length of 25.00 mm and width of 4.00 mm. For the fatigue crack growth experiments, a 0.5 mm deep notch was EDM in the center of the gauge length to facilitate pre-cracking. A schematic of the specimen is shown in Fig. 1.5.

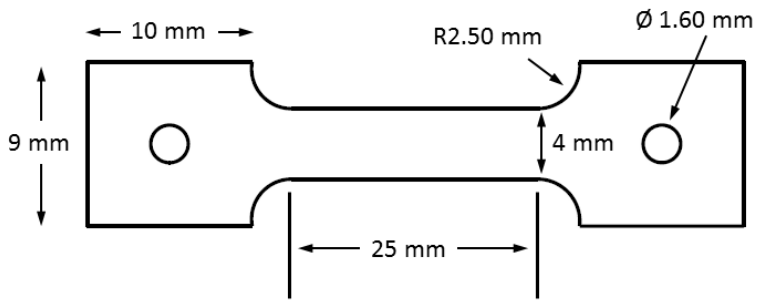

Fig. 1.5 - Schematic of the dog-bone specimen geometry.

To determine the mechanical properties of Haynes 230, tensile experiments were performed at room temperature, 700 °C, 800 °C, and 900 °C. The results are given in Fig. 1.6. All four experiments were run at a strain rate of 10^{-4} s^{-1}. The yield stress for each temperature was found using a 0.2% offset. These values were found to be 415 MPa at room temperature, 302 MPa at 700 °C, 197 MPa at 800 °C, and 123 MPa at 900 °C. Hardening was observed in the room temperature results and initially in the 700 °C results, while the 800 °C and 900 °C results showed softening. Serrations in the 700 °C stress-strain curve were attributed to the Portevin-Le Chatelier effect. This has also been found in other similar nickel-based superalloys, such as Hastelloy X [17]. The specimens fractured at 50% strain at room temperature, 61% strain at 700 °C, 51% strain at 800 °C, and 32% at 900 °C. At all temperatures, the failure depicted the classic cup and cone fracture.

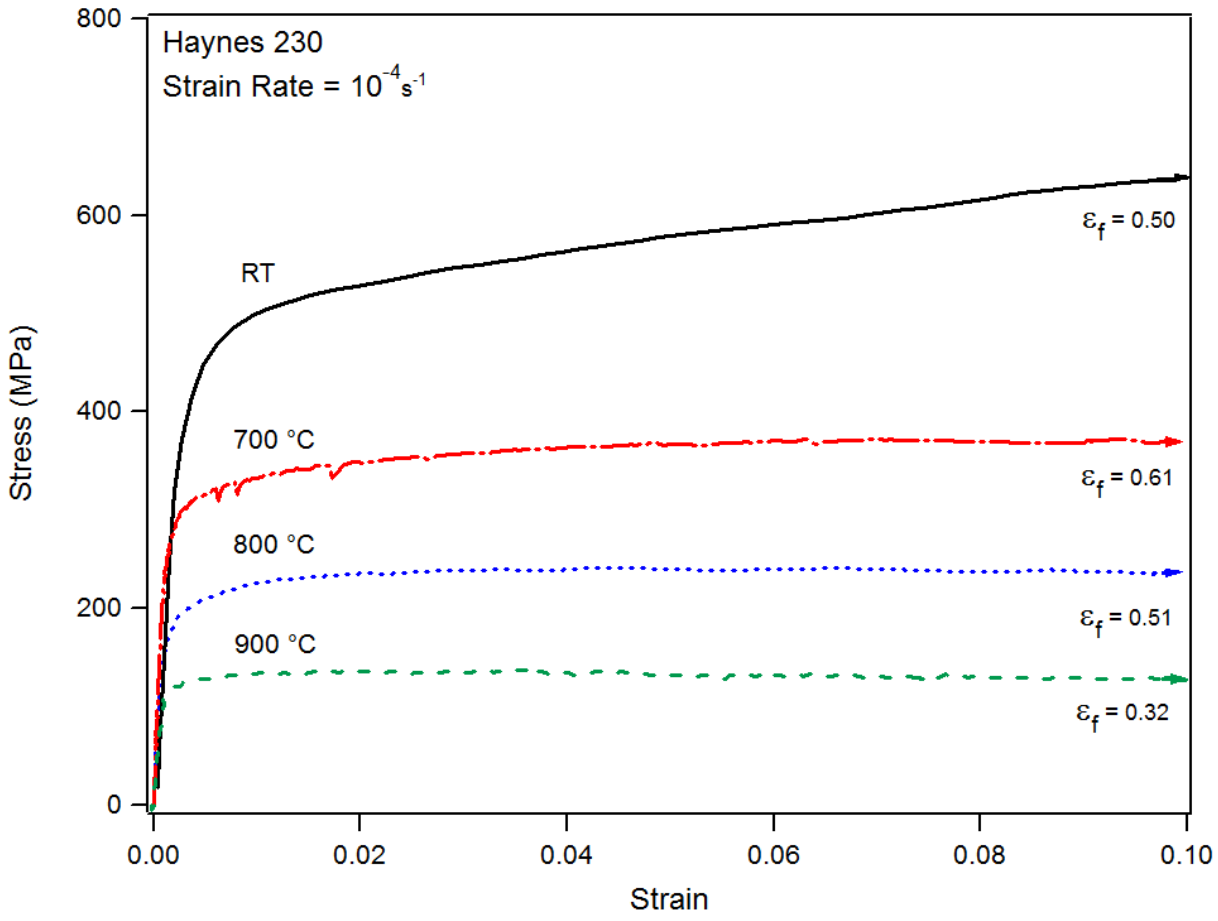

Fig. 1.6 - Stress-strain data for Haynes 230 at room temperature, 700 °C, 800 °C, and 900 °C.

1.2.2.2 NiTi

The NiTi material was nickel rich with a composition of 50.375 at%. Single crystals were grown in an inert environment using a Bridgman technique in order to produce [148] and [112] orientations. The material was solutionized at 920 °C for 24 hours in a vacuum furnace and quenched. The specimens were then aged at 550 °C for 1.5 hours to produce a microstructure with precipitates of size near 400 nm [18]. This aging also resulted in room temperature (25 °C) pseudoelasticity. Differential scanning calorimetry (DSC) results were obtained by thermally scanning samples at 40 °C/min using a Perkin-Elmer Pyris 1. The characteristic temperatures were found to be A_f = 0 °C, A_s = -15 °C, M_s = -55 °C, and M_f = -75 °C. This analysis was repeated on 3 additional samples and consistent results were found. Using ASTM standard E1269, the specific heat was determined to be C_p = 590 J/kg K. The parent phase was B2 and upon loading transformed to B19' martensite. A full review of NiTi can be found in [19].

1.2.2.3 Ni_2FeGa

This alloy was cast at a nominal composition of $Ni_{54}Fe_{19}Ga_{27}$ (at%). Single crystals were also grown using a Bridgman technique to create the [001] and [011] oriented single crystals. The samples were kept unaged and also exhibited pseudoelastic behavior at room temperature. A DSC analysis on 3 samples provided characteristic temperature values of A_f = 22 °C, A_s = 14 °C, M_s = 6 °C, and M_f = -3 °C with a specific heat of C_p = 460 J/kg K. The Ni_2FeGa undergoes $L1_2 \rightarrow 10M \rightarrow 14M \rightarrow L1_0$ transformation upon stressing. More information concerning Ni_2FeGa is detailed in [20].

1.2.2.4 CoNiAl

The third SMA studied was $Co_{40}Ni_{33.17}Al_{26.83}$ (at%). Single crystals were grown using the same technique as the previous two materials. The [115] oriented single crystals were aged for 4.5 hours at 1275 °C. These specimens produced pseudoelastic results at 100 °C. Other subsequent heat treatments consisting of 1, 2, and 3 hours at 1250 °C did not result in room temperature pseudoelasticity. The DSC results showed consistent characteristic temperatures of A_f = 45 °C, A_s = 22 °C, M_s = 16 °C, and M_f = 0

°C and a specific heat of C_p = 279 J/kg K. At 100 °C, CoNiAl undergoes transformation from B2 to $L1_0$ martensite with further details presented in [21].

1.3 Objectives

The overall objective of this body of work is to quantitatively advance the state of knowledge concerning metals which can reduce the reliance on fossil fuels and HFC refrigerants. Nuclear energy has been revitalized as an alternative to fossil fuels for energy production, and the NGNP will be much more demanding on materials. A solid state refrigeration solution may be the novel solution to scaling back harmful vapor compression refrigerants. Both goals would expand the usefulness of metals and studying them will further our understanding of deformation phenomena.

The specific contributions of this work are to:

- Develop experimental techniques to measure and quantify strain fields during elevated temperature experiments. It was a priority to combat the radiation of light and surface oxidation in order to use digital image correlation while maintaining low measurement error.
- Advance the established high resolution, sub-grain level digital image correlation with supporting microstructural characterization technique to study elevated temperature deformations. The sub-grain measurement resolution allows for linking deformation to the microstructure producing results which are beneficial to the development of physics-based models.
- Utilize the developed experimental techniques to analyze the deformation of Haynes 230 at elevated temperatures. Three specific cases of deformation have been investigated and related to microstructural phenomena: fatigue crack growth, creep, and an interrupted tensile experiment.
- Develop an experimental setup using infrared thermography and digital image correlation in order to measure the temperature change in shape memory alloys during the reverse

martensitic transformation. The dual camera technique provides the ability to relate the local temperature gradients to the transformation bands.

- Establish the temperature change magnitudes of three SMAs: NiTi, Ni_2FeGa, and CoNiAl. Experimentally measured temperature changes using an IR camera during tensile experiments and results found using the measured value of entropy change for each alloy will provide a basis for examining the potential of SMAs as solid-state refrigerants.

1.4 Thesis Outline

This thesis consists of seven chapters and details about each chapter will be summarized in the following:

Chapter 2 will focus on the experimental study of fatigue crack growth in Haynes 230 at room temperature and 900 °C. A significant increase in the fatigue crack growth rates at 900 °C is presented. Results and discussions about the crack closure, measured strain irreversibilities, and reasons for the increased fatigue crack growth rates are given.

Chapter 3 focuses on the creep of Haynes 230 at 800 °C and 900 °C. Differences between the creep curves and mechanisms will be discussed. Also, local strain concentrations, their connections to the microstructure, and their impact on creep life are included.

In Chapter 4, a high resolution *ex-situ* DIC technique for elevated temperatures is presented. This technique adopts a previously established high resolution DIC technique and advances it for use with materials deformed at elevated temperatures. Focus is given to the sample preparation and experimental procedure.

Using the technique described in the previous chapter, Chapter 5 consists of the study of interrupted tensile experiments on Haynes 230 at 700 °C and 800 °C. The global trends are compared to room temperature results from another nickel-based superalloy. Localized strain fields and the influence of the microstructure are discussed.

The elastocaloric cooling potential of SMAs is examined in Chapter 6. Temperature change measurements during the reverse martensitic transformation are given for NiTi and Ni_2FeGa at room temperature and CoNiAl at 100 °C. A discussion about the essential traits for an SMA refrigerant, including the fatigue life, and the potential to increase the temperature change are incorporated.

Finally in Chapter 7, the main conclusions of this work are detailed and future work suggestions are given.

1.5 References

[1] World Development Indicators 2014. Washington, DC: World Bank, 2014.

[2] G. E. A. Writing Team, Global Energy Assessment, Cambridge University Press, 2012.

[3] L.E. Demick. Transforming the U.S. Energy Infrastructure, Idaho National Laboratory INL/EXT-09-17436 (2010).

[4] T. Burchell, R.L. Bratton, R.N. Wright, J. Wright. Next generation nuclear plant materials research and development program plan, Idaho National Laboratory INL/EXT-06-11701 (2007).

[5] NGNP High Temperature Materials White Paper, Idaho National Laboratory INL/EXT-09-17187 (2010).

[6] G.J.M. Velders, D.W. Fahey, J.S. Daniel, M. McFarland, S.O. Andersen. The large contribution of projected HFC emissions to future climate forcing, Proceedings of the National Academy of Sciences 106 (2009) 10949-10954.

[7] X. Moya, S. Kar-Narayan, N.D. Mathur. Caloric materials near ferroic phase transitions, Nature Materials 13 (2014) 439-450.

[8] G.V. Brown. Magnetic heat pumping near room temperature, Journal of Applied Physics 47 (1976) 3673-3680.

[9] L. Mañosa, S. Jarque-Farnos, E. Vives, A. Planes. Large temperature span and giant refrigerant capacity in elastocaloric Cu-Zn-Al shape memory alloys, Applied Physics Letters 103 (2013).

[10] M. Sutton, J.-J. Orteu, H. Schreier. Image Correlation for Shape Motion and Deformation Measurements: Basic Concepts, Theory and Applications, Spring Media, 2009.

[11] C. Badulescu, M. Grediac, H. Haddadi, J.D. Mathias, X. Balandraud, H.S. Tran. Applying the grid method and infrared thermography to investigate plastic deformation in aluminium multicrystal, Mechanics of Materials 43 (2011) 36-53.

[12] F. Delaire, J.L. Raphanel, C. Rey. Plastic heterogeneities of a copper multicrystal deformed in uniaxial tension: experimental study and finite element simulations, Acta Materialia 48 (2000) 1075-1087.

[13] E. Héripré, M. Dexet, J. Crépin, L. Gélébart, A. Roos, M. Bornert, D. Caldemaison. Coupling between experimental measurements and polycrystal finite element calculations for micromechanical study of metallic materials, International Journal of Plasticity 23 (2007) 1512-1539.

[14] P. Rastogi, Y. Surrel. Fringe Analysis. Photomechanics, vol. 77. Springer Berlin Heidelberg, 2000. pp. 55-102.

[15] J.D. Carroll, W.Z. Abuzaid, J. Lambros, H. Sehitoglu. On the interactions between strain accumulation, microstructure, and fatigue crack behavior, International Journal of Fracture 180 (2013) 223-241.

[16] J. Carroll, W. Abuzaid, J. Lambros, H. Sehitoglu. An experimental methodology to relate local strain to microstructural texture, Review of Scientific Instruments 81 (2010) 083703.

[17] B. Swaminathan, J. Lambros, H. Sehitoglu. Digital image correlation study of mechanical response of nickel superalloy Hastelloy X under thermal and mechanical cycling: Uniaxial and biaxial stress states, The Journal of Strain Analysis for Engineering Design (2013).

[18] H. Sehitoglu, R. Hamilton, D. Canadinc, X.Y. Zhang, K. Gall, I. Karaman, Y. Chumlyakov, H.J. Maier. Detwinning in NiTi alloys, Metallurgical and Materials Transactions A 34 (2003) 5-13.

[19] K. Otsuka, X. Ren. Physical metallurgy of Ti-Ni-based shape memory alloys, Progress in Materials Science 50 (2005) 511.

[20] R.F. Hamilton, C. Efstathiou, H. Sehitoglu, Y. Chumlyakov. Thermal and stress-induced martensitic transformations in NiFeGa single crystals under tension and compression, Scripta Materialia 54 (2006) 465.

[21] R.F. Hamilton, H. Sehitoglu, C. Efstathiou, H.J. Maier, Y. Chumlyakov, X.Y. Zhang. Transformation of Co-Ni-Al single crystals in tension, Scripta Materialia 53 (2005) 131.

Chapter 2. High Temperature Fatigue Crack Growth in Haynes 230

[Note: The material in this chapter has been published as Pataky *et al.*, Materials Characterization, doi:10.1016/j.matchar.2012.09.012]

2.1 Background

Fatigue crack growth is extremely detrimental to the life of engineering components and has been the focal point of much research. Traditionally, there have been two distinct areas of concern when studying fatigue cracks: the crack wake and the crack tip. Crack closure is a phenomenon which occurs in the wake of the fatigue crack and has been used to describe the reduction of load seen by a crack during a fatigue loading cycle [1]. Plasticity-induced crack closure is shown in Fig. 2.1. A variety of methods to measure the level of crack closure have been employed historically including displacement gages, lasers, and potential drop measurements [2]. The advent of DIC provided a method to assess crack closure locally at the crack tip using digital (virtual) extensometers and globally using full field displacements [3-5]. The reduction of the stress intensity factor range due to crack closure provides a more general relationship to describe crack growth rates by removing the influence of loading factors such as the load ratio, R [6]. Although this modification has been very beneficial to describing fatigue crack growth behavior, it does not provide a complete explanation to crack growth rate variations. Alternatively, other studies of fatigue crack growth have focused on the fatigue crack tip, the plastic zone, and the dislocation interactions with the microstructure.

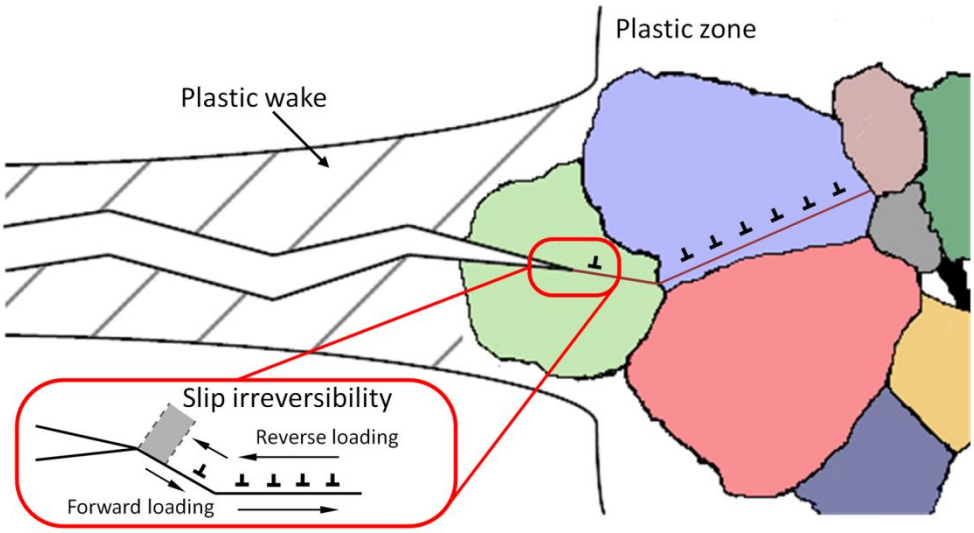

Fig. 2.1 - A schematic of a fatigue crack with plasticity-induced crack closure in the crack wake and slip irreversibility at the crack tip. The shaded grey region in the inset provides a measure of the irreversible slip strain (or irreversible displacements).

Models which describe fatigue crack growth rates as a crack tip phenomenon have been continually refined to smaller scales as new developments were made. Tomkins was the first to relate crack tip plasticity to the crack growth rate using Dugdale's plastic cohesive stress model [7]. During the unloading portion of a fatigue cycle, reverse plasticity occurs due to the reversal of loading. This creates a reversed (or cyclic) plastic zone ahead of the crack tip within the monotonic plastic zone [8, 9]. Further works relating the fatigue crack growth rate to plastic zones relied on using this ideology of a reversed plastic zone [10, 11]. It was determined that a larger reversed plastic zone size would cause an increase in the fatigue crack growth rate. Using a finite element analysis, McClung and Sehitoglu were able to demonstrate that crack closure can affect the reversed plastic zone size [12].

With evolution of crack tip plasticity being the major driving force in fatigue crack growth in ductile materials, light had to be shed on the role played by dislocations. Early discoveries included the finding that cross slip had a direct influence on the rate of crack propagation [13]. Forsyth explored crack initiation and observed that as dislocations cross slipped, extrusions formed. As the cross slipping of dislocations occurred at the extruded material, a crack formed [14]. Building upon this observation, Fong

and Tromans developed a model of restricted slip reversal to describe crack growth in terms of dislocations emitted from the crack tip during cyclic loading [15]. This concept introduced slip irreversibility and is shown in Fig. 2.1. Pippan studied the force required to emit dislocations at the crack tip and related the quantity of emitted dislocations that do not fully reverse to the crack growth rate [16, 17]. Wu *et al*. related the plastic strain ahead of the crack tip, due to slip irreversibility, to the fatigue crack growth rate [18]. A technique using DIC has been developed to determine the quantity of residual crack tip plastic strain and has been demonstrated for several materials at room temperature [6, 19].

The current study will provide further experimental insight into fatigue crack growth at elevated temperatures. Haynes 230 was studied due to its good corrosion resistance and properties at elevated temperatures making it a viable candidate for structures under extreme conditions. The analysis encompasses both the previously discussed phenomena of crack closure and slip irreversibility. Using novel techniques to employ DIC at 900 °C, it will be shown that slip irreversibility at the crack tip is the key damage mechanism driving fatigue crack growth.

2.2 Material Preparation and Experimental Procedure

2.2.1 Material Preparation

The experiments in this study were performed on the commercially available nickel-based superalloy Haynes 230. Details about the material utilized are given in Section 1.2.2.1. To emphasis the typical microstructure of this sheet, an optical micrograph is displayed in Fig. 2.2. Single-edge notched dog-bone specimens (Fig. 1.5) with a 0.5 mm deep notch EDM in the center of the gauge length to facilitate pre-cracking were used.

In order to prepare the specimens for DIC, two separate procedures were required depending on the temperature condition. For the room temperature (RT) experiment, the specimens were mechanically polished to a mirror finish using abrasive paper up to P2400 grit size. Black paint was then airbrushed onto the specimen surface to create a speckled pattern. The high temperature (HT) experiment required a

different preparation since at 900 °C the sample glowed. The front of the sample was painted white with a thin layer of very high temperature paint. The paint was then cured using a three-step process, exposing it to a maximum temperature of 315 °C. A layer of black paint was then airbrushed onto the specimen as was done with the room temperature experiment. The white paint was required for the HT sample to reduce the brightness that comes with the glowing and to prevent the speckle pattern from changing due to oxidation.

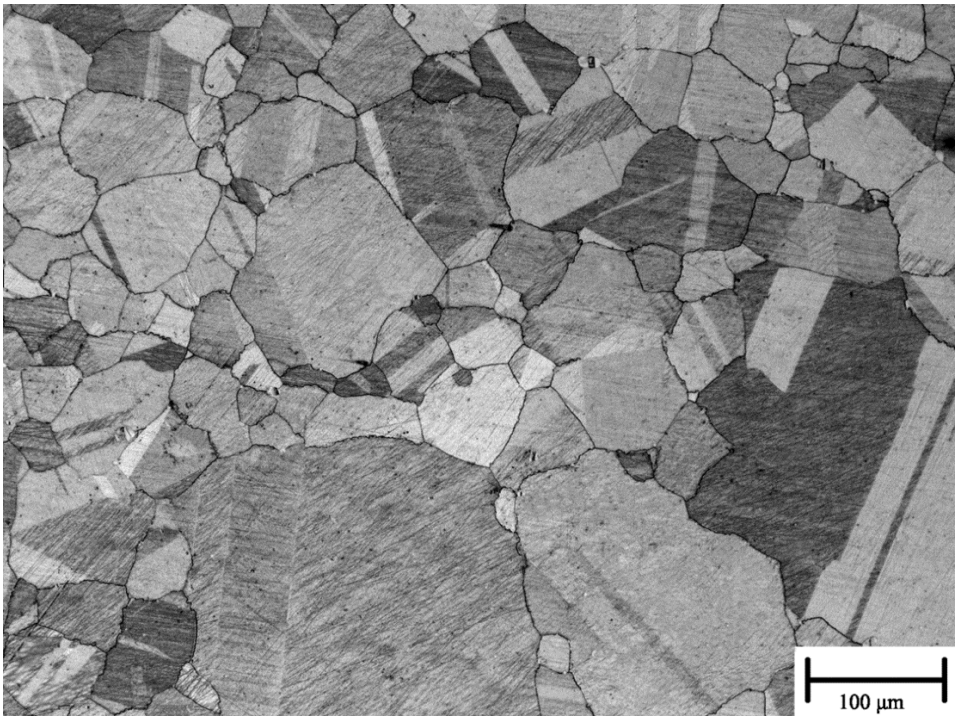

Fig. 2.2 - Microstructure of the as-received Haynes 230 material showing annealing twins and a wide range of grain sizes.

2.2.2 Experimental Procedure

A servo-hydraulic load frame was used during the experiments. The HT specimen was heated using induction heating. A type-K thermocouple was spot welded on the middle of the back of the specimen approximately 2 mm above the notch plane. While at zero load, the specimen was heated at a rate of 75 °C per minute until the sample reached 900 °C. The temperature was kept within ±3 °C for the entirety of the experiment. The specimens were cyclically loaded at a load ratio, R, of 0.05 at a frequency

of 3 Hz. The RT specimens were fatigue loaded with a stress range of 270 MPa. The stress range had to be reduced due to the lower yield stress at 900 °C, and the HT specimen was fatigue loaded with a stress range of 104.5 MPa. A computer program controlled the servo-hydraulic load frame and captured images and their corresponding loads measured by a 7.5 kN load cell during the test. Once a crack was visually identified, measurement cycles were periodically run at a frequency of 0.25 Hz in order to capture a greater number of images per cycle to provide an in-depth analysis into the fatigue cycles.

A commercially available image correlation program was used to perform DIC analysis. For the crack closure analysis, the first image of each measurement cycle, captured at minimum load, was used as the reference image for that cycle. When studying slip irreversibility, the first image of the experiment, again captured at minimum load, was used as the reference image since strains due to the crack were not present yet. The full field of displacements, both behind and ahead of the crack tip, was used for correlations. The displacements were used in the least-squares regression, as briefly described in the Appendix, in order to determine the effective stress intensity factor ranges and crack closure levels. At each correlated point, the horizontal (Δx) and vertical (Δy) displacements were calculated and differentiated to obtain the strains assuming a small strain approximation.

For transmission electron microscopy (TEM) 1 mm thick discs were sectioned with a low-speed diamond saw parallel to the loading axis from the failed specimens, and then mechanically ground and polished down to 0.15 mm foil thickness. Large electron transparent areas were obtained in these foils by conventional twin jet polishing using a solution consisting of 5% perchloric acid in ethanol at -20 °C and 15 V. The TEM was operated at a nominal voltage of 200 kV and a double-tilt specimen holder was employed for imaging under two-beam conditions.

2.3 Results

2.3.1 Fatigue Crack Growth

Images were continuously taken during the fatigue crack growth tests to use digital image correlation to capture the full field displacements. Crack growth rates were determined by using these images to follow the crack tip advancement. As indicated in Fig. 2.3, both RT and HT fatigue crack growth tests were run. The solid symbols in Fig. 2.3 represent the isotropic stress intensity factor range calculation

$$\Delta K = \Delta\sigma\sqrt{\pi \cdot a} \cdot f(a/w) \tag{2-1}$$

where $\Delta\sigma$ is the stress range, a is the current crack length, and $f(a/w)$ is the geometric correction factor which can be found in [22]. Eq. (2-1) does not account for crack closure though. The least-squares regression code explained in [3] and the Appendix was used to extract the effective stress intensity factor range from the experiments by considering the full field crack tip displacements which inherently are effected by crack closure during a fatigue cycle. The effective stress intensity factor results which consider crack closure are shown as hollow symbols in Fig. 2.3. The insets included in this figure show the experimental and regressed vertical displacement contours corresponding to the RT and HT specimens. The Paris law coefficients and exponents for both tests are shown in Table 2.1. The Paris law exponent is about 2 for both test results which is in the common range of 2 to 4 for metals [23]. The following form of the Paris law was used to find the effective results which considered crack closure

$$da/dN = C(\Delta K_{eff})^m \tag{2-2}$$

where

$$\Delta K_{eff} = \Delta\sigma_{eff}\sqrt{\pi \cdot a} \cdot f(a/w) \tag{2-3}$$

C and m are the Paris coefficient and exponent respectfully, $\Delta\sigma_{eff}$ is the effective stress range (the portion of the loading cycle the crack is open), and a is the crack length.

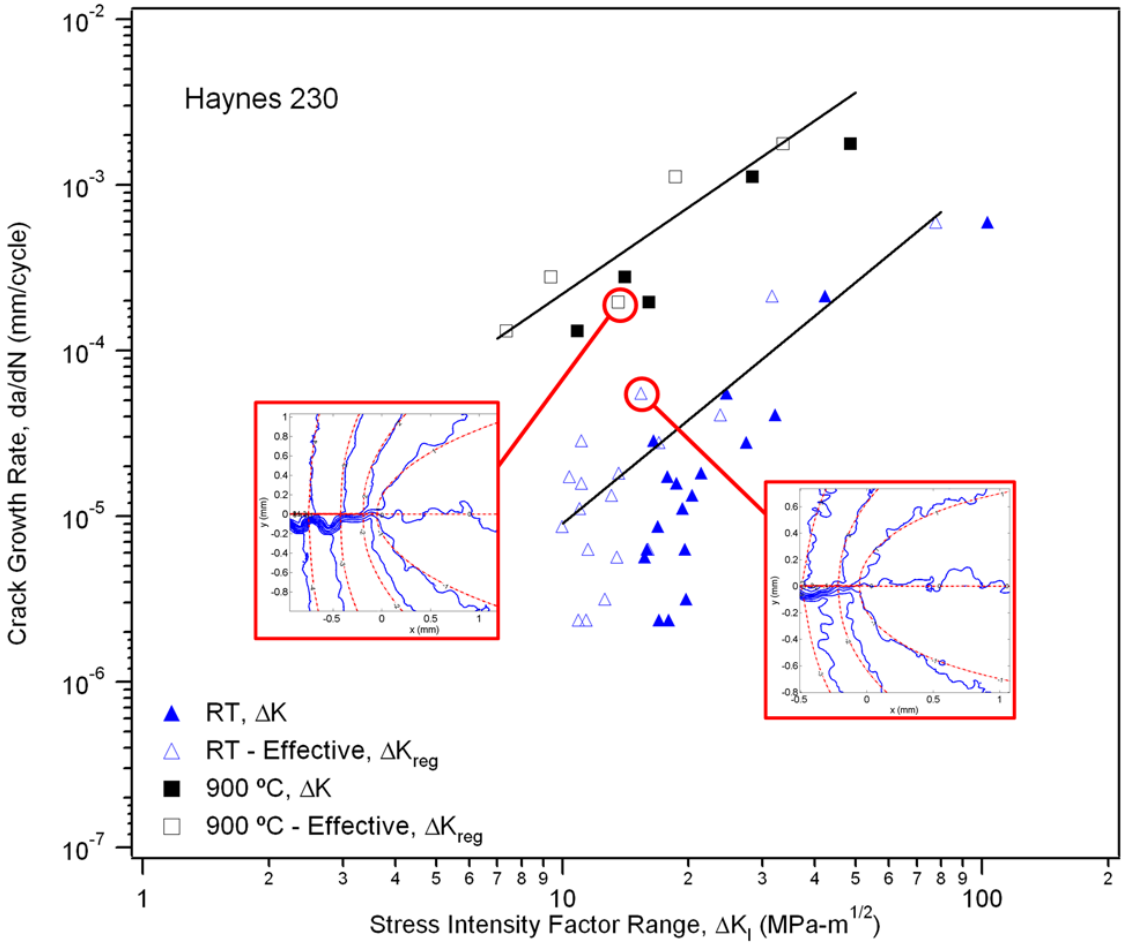

Fig. 2.3 - The crack growth rate as a function of the stress intensity factor range for room temperature (RT) and 900 °C experiments. The insets are displacement contour plots showing the experimental (blue) and regression (red) vertical displacements in increments of 1 micron with the black dot indicating the crack tip location.

Table 2.1 - Paris law coefficients for Haynes 230 at RT and 900 °C (da/dN in mm/cycle and ΔK in MPa√m).

	C	m
RT Theoretical	1.34E-08	2.38
RT Effective	7.54E-08	2.08
900 °C Theoretical	1.81E-06	1.82
900 °C Effective	4.20E-06	1.74

The crack growth rate for the HT experiment was over an order of magnitude higher than in the RT experiment, being in the range of 10^{-3} to 10^{-2} mm/cycle. This is an extremely high rate of fatigue crack growth and could lead to failure in a component before the crack is initially detected. Comparing the isotropic and effective stress intensity factor values, the crack closure level for both experiments was an average of 30% of the load. To show the effectiveness of the regression technique in determining the closure level, two-point digital extensometers, which measure local crack opening levels, were used to find closure values along the crack length for both the RT and HT specimens. The comparison results are provided in Fig. 2.4. The regression technique, also referred to as the full-field method, proved to be efficient in estimating the crack closure levels at the crack tip. The two-point digital extensometers also provided insight into the reduction of crack closure at distances away from the crack tip. The similarity in the closure levels between the two specimens is a surprising result and provides no conclusion about the faster crack growth rate at HT, thus, slip irreversibility was investigated.

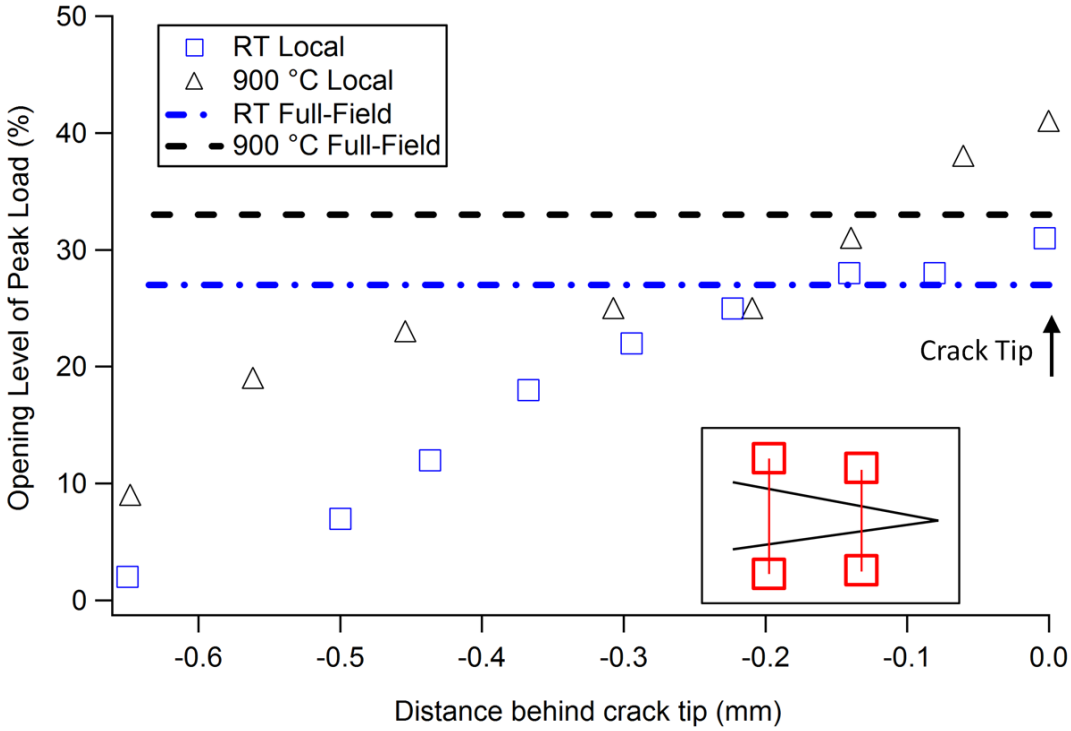

Fig. 2.4 - A comparison between the local (digital extensometer) and full-field (regression) crack opening levels for the RT specimen at a crack length of 0.994 mm and the HT specimen at a crack length of 0.964 mm. Symbols represent the digital extensometer values at various points along the crack while lines represent the regression found value for the full-field. The schematic depicts the digital extensometer technique and placement along the crack flanks.

2.3.2 Slip Irreversibility

With the stress intensity factors known, a plane stress assumption was used to approximate the plastic zone size [24]. Shown in Fig. 2.5a is the plastic zone for the RT specimen at crack length of 0.994 mm at maximum load. The blue contours represent the experimental displacement contours in micrometers, and the red contours are the displacement contours in micrometers found using the values from the least-squares regression. Using the effective stress intensity factor of 16.55 MPa√m, the plastic zone radius was determined to be 0.337 mm. Strains found from digital image correlation were inserted into the plastic zone and high values of strain are found throughout the plastic zone. To compare, a HT specimen cycle at a crack length of 0.964 mm was used as shown in Fig. 2.5b. The effective stress intensity factor for this crack length was 9.39 MPa√m and the corresponding plastic zone radius was found to be 0.664 mm. The strains in the plastic zone show a concentration around the crack tip. Even

though the HT specimen had a much smaller effective stress intensity factor range, the lower yield stress caused the plastic zone size to be approximately twice that of the RT specimen at the same crack length.

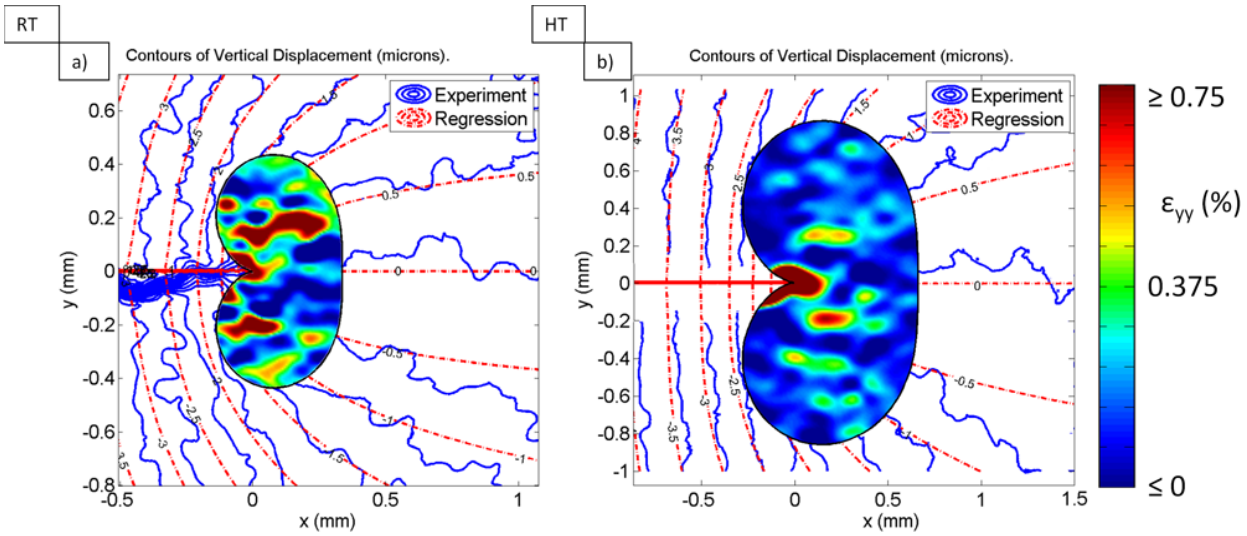

Fig. 2.5 - Plots of vertical displacement contours and plastic zones for a selected a) room temperature and b) 900 °C fatigue crack cycle. Blue contours represent the experimental DIC displacements and red contours represent the regression found displacement contours. a) At a crack length of 0.994 mm, the room temperature specimen had a ΔK value of 22.64 MPa$\sqrt{m}$, a regression found ΔK_{eff} value of 16.55 MPa$\sqrt{m}$, and a plastic zone radius of 0.337 mm. b) At a crack length 0.964 mm, the 900 °C specimen had a ΔK value of 14.08 MPa$\sqrt{m}$, a regression found ΔK_{eff} value of 9.39 MPa$\sqrt{m}$, and a plastic zone radius of 0.666 mm.

Although these plastic zone approximations give much insight into the plasticity caused by the fatigue crack growth, the crack tip slip irreversibility was of great interest due to its correlation with the crack growth rate. As dislocations are emitted from the crack tip during a fatigue cycle and do not fully reverse to the crack tip, strain is accumulated. In order to capture this behavior, measurements of the strain were made at the beginning and end of the cycle. Thus, the difference between the reversed plastic zone ε_{yy} strain magnitude in points A and B, shown in the bottom right of Fig. 2.6, can be considered the slip irreversibility for one cycle. To quantitatively measure this at the meso-scale, DIC has been utilized. The DIC strain plots in Fig. 2.6 are used as an example of this technique. The two strain plots are one cycle apart, with the image labeled "A" being recorded at the beginning of the cycle and the image labeled "B" being at the end. The isotropic and effective stress intensity factor ranges were 24.6 MPa$\sqrt{m}$

and 15.4 MPa√m respectively with a crack closure level of 37% for the RT example and 13.86 MPa√m and 9.39 MPa√m respectively with a crack closure level of 32% for the HT example. The strain plots show strain at the crack tips before the cycle for point "A" (referring to Fig. 2.6) and then after the cycle for point "B" which shows residual strains at the crack tip. Strain measurements of the reversed plastic zone in front of the crack at points "A" and "B" were compared and irreversible strains of 6.35×10^{-4} for the RT sample and 5.36×10^{-3} for the HT specimen were measured. This technique was applied for multiple crack lengths of the RT and HT specimens. As with the two examples provided, the trend of the HT specimen having irreversible strain an order of magnitude higher than the RT specimen was consistent throughout as shown in Fig. 2.6.

As these measurements are quite small, the error of the measurements must be determined. In order to find the average and maximum errors, four images of the undeformed surface were captured and correlated. For the HT specimen, the images were captured after the specimen had been heated to 900 °C. The mean ε_{yy} error for the HT case was 9.49×10^{-5}, while the maximum (which occurred ~0.25 mm above the crack path) was found to be 0.00235. For the RT specimen, the mean ε_{yy} error was higher, 3.47×10^{-4}. The maximum error found was in the crack path, with a magnitude of 0.00473. The RT error is on the order of the strain irreversibility measurements. The results of the HT strain irreversibility are an order of magnitude higher than the error. This indicates that the finding of strain irreversibility being significantly higher at HT compared to RT is valid.

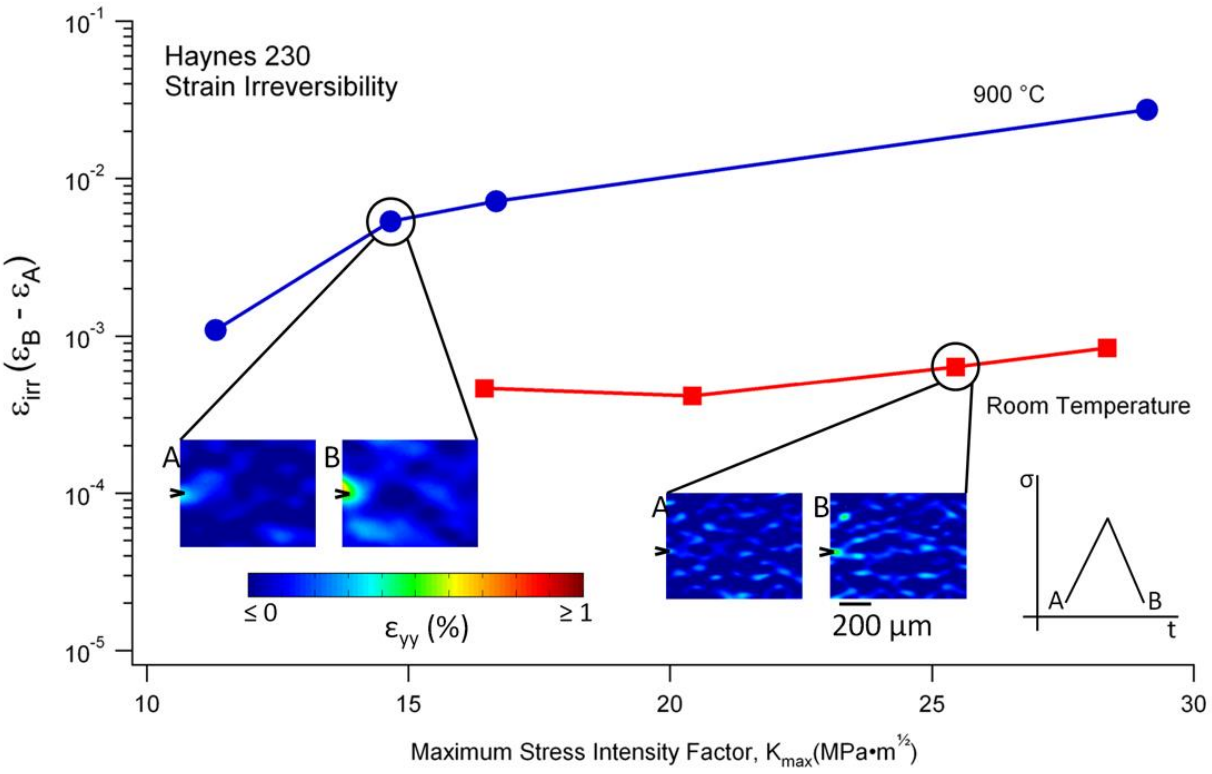

Fig. 2.6 - Strain irreversibility as a function of the maximum stress intensity factor during the fatigue crack growth experiments. The schematic shows the two minimum load points (A and B) where the strain measurements were taken. DIC strain plots for both the room temperature and 900 °C experiments are shown and the higher strains in the B plots compared to the A plots indicated irreversible strains during the fatigue cycle.

2.3.3 Scanning Electron Microscope and Transmission Electron Microscopy Analysis

In order to further understand the microstructural response of the Haynes 230 sample fatigued at 900 °C, images of the fracture surface were taken with a scanning electron microscope (SEM) and the dislocation arrangements were observed with transmission electron microscopy (TEM). The first SEM micrograph, shown in Fig. 2.7a, shows the classic striations attributed to cyclic fatigue crack growth. This verifies that the external loading was responsible for the propagation of the crack and ultimately the failure of the material. Also evident in this micrograph is the effects of the high temperature damage as it was taken in a region that experienced a high *K*. Fig. 2.7b provides an example of the smoothness of the surfaced signifying the low amount of oxidation present. This is consistent with the Haynes International, Inc. data and previously completed research [25, 26].

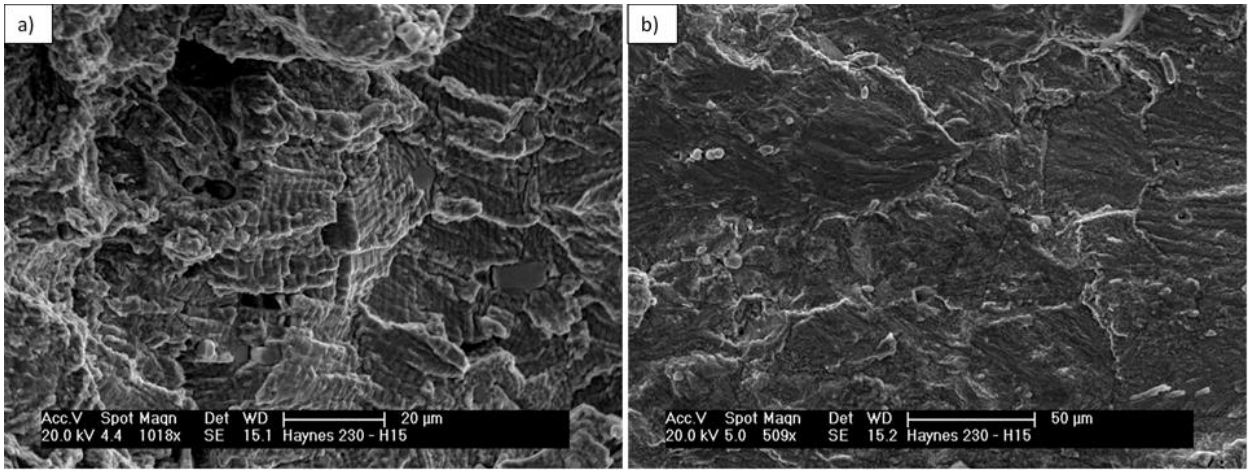

Fig. 2.7 - a) A high magnification SEM micrograph showing the fatigue striations on the 900 °C specimen. b) The post-fracture surface of the 900 °C specimen showing a low level of oxidation and a smooth surface indicative of intragranular fatigue crack growth.

A TEM analysis was then performed to observe the dislocations and any other phenomena present. As shown in Fig. 2.8, planar slip was observed. This is consistent with other solid-solution hardened fcc alloys [27] and other nickel-based superalloys fatigued at high frequencies at high temperatures [28]. Also of particular interest was the formation of subgrains with several being present in the image. This was seen throughout the specimen with another example being given in Fig. 2.9. Obvious from this TEM image is a large heterogeneity in the microstructure. On the left, dislocations are present with nothing to impede their motion. Dividing the image in half is a stacking fault. On the right half of the image, intense dislocation-carbide interactions are observed providing for substantial resistance to dislocation motion. There are two types of carbides present in this image which are assumed to be M_6C and $M_{23}C_6$. The larger of the two found along the stacking fault is believed to be of the M_6C type and has far less interaction with dislocations than the $M_{23}C_6$ carbides.

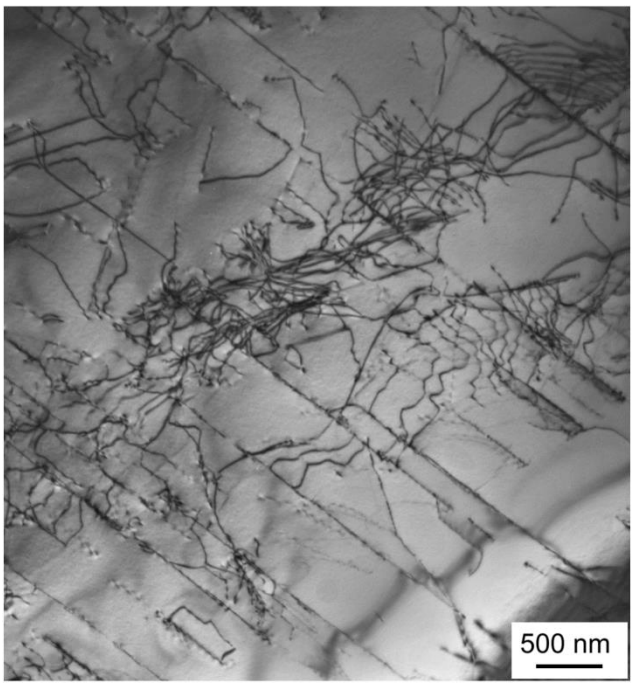

Fig. 2.8 - Planar slip in the Haynes 230 material.

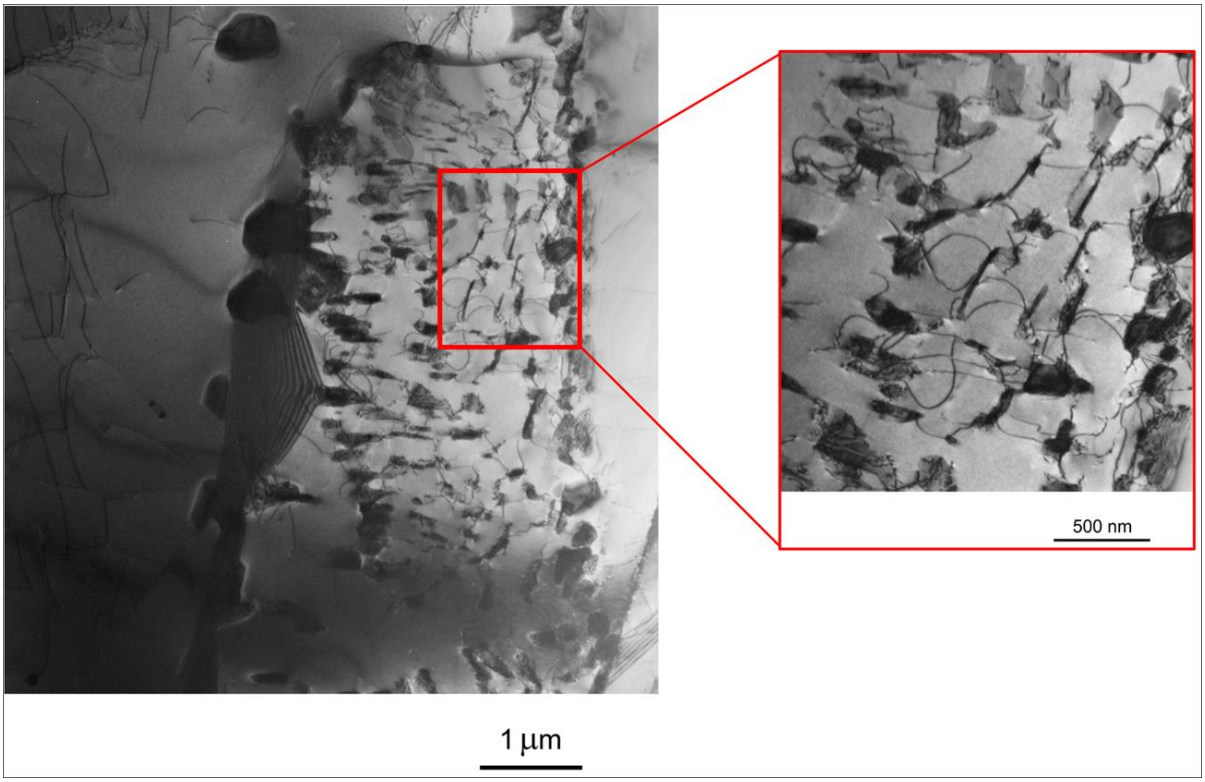

Fig. 2.9 - An SEM micrograph showing the heterogeneity in Haynes 230. A stacking fault separates areas of low carbide density and high carbide density. The cutout shows a dense area of carbide-dislocation interactions.

2.4 Discussion

2.4.1 Crack Closure Effects

As reported in Section 2.3.1, crack closure was present for both cases. Crack closure phenomena have been extensively studied beginning with Christensen who discovered roughness induced crack closure in 1963 [29]. Due to the pure Mode I loading on the specimens tested in this study, roughness induced crack closure was concluded not to be the main crack closure phenomenon. Mode II loading is typically necessary to see roughness effects. By observing the crack faces on the failed specimens, very little deviations and asperities were seen supporting this conclusion. Thus, other forms of crack closure had to be considered.

By first taking into account the RT and HT cases together, plasticity induced crack closure was the most likely form of crack closure present in this study. Elber first discovered this phenomenon and found that the residual plasticity stretching from the crack tip across the entire crack face provided a shielding mechanism from the remote loading [30, 31]. The DIC strain fields showed residual plasticity behind the crack tip and in shear bands extending from the crack tip. From this result it can be gleaned that plasticity induced crack closure is present and is the dominating form of crack closure. Previously, studies have concluded that load ratio effects are minimized when considering the effective stress intensity factor range [32]. Other studies have looked at the crystallography of single crystals and found that the effective stress intensity factor range can also be used to eliminate scatter in fatigue crack growth data [6]. The usefulness of taking into account crack closure is evident for removing the dependence on the loading conditions, but does not account for the differences in RT and HT fatigue crack growth rates seen in this investigation.

At high temperatures, the propagation rate of cracks can be several orders of magnitude higher than at room temperature. This has also been shown in previous fatigue crack growth studies of Haynes 230 [33, 34]. Under these conditions, the crack tip might experience creep and environmental attack.

Oxidation and hold times have been shown to increase the crack growth rate of Haynes 230 at highly elevated temperatures [25, 26, 34]. In order to determine the effects of these high temperature phenomena, oxide-induced crack closure must be considered in the HT case.

Although this nickel-based superalloy has excellent oxidation resistance and a high frequency was chosen in an effort to minimize environmental effects, the freshly exposed material due to the crack growth still oxidized. Investigations were performed in the 1980s to determine the effect that oxides have on fatigue crack growth in steels [35], copper [36], and nickel-based superalloys [37]. Ritchie, Suresh, and Moss commented that the oxide films forming at the crack tip and any fretting of this film due to the roughness induced crack closure will increase the closure and decrease ΔK [38]. Although this information sheds light onto the role of crack closure on the fatigue crack growth in this study, both specimens in this current study show the same level of crack closure of about 30%. Also, an important finding in the literature is that oxide thickness needs to exceed or equal the crack tip opening displacement (CTOD) to have an effect. This is not the case for the crack growth condition studied here. Therefore, crack closure provides no explanation for the much faster crack growth rates in the HT case.

2.4.2 Slip Irreversibility

As discussed in the Introduction, the crack tip is the other area of interest for understanding the mechanics of fatigue crack growth. Dislocation interactions with the microstructure features, whether these are grain/twin boundaries or defects, control the slip irreversibility during a fatigue cycle. This occurs when dislocations interact with boundaries and a residual dislocation is left within that boundary [39]. Certain types of boundaries can play a significant role in increasing the resistance to fatigue crack growth and have been the focus of "grain boundary engineering". These boundaries are typically described as low sigma numbered, as defined in terms of coincidence site lattice theory [40]. Of particular interest have been annealing twins or $\Sigma 3$ boundaries and studies have shown that a greater number of $\Sigma 3$ boundaries leads to increased fatigue crack growth resistance. The twin boundary acts as a barrier to slip leading to a dislocation pile-up and a stress field that prevents dislocations from being

emitted from the crack tip [19]. The microstructure of the Haynes 230 used in this study was described in Section 1.2.2.1 and the very high amount of $\Sigma 3$ boundaries found in this nickel-based alloy contributes to its good fatigue crack growth resistance (Paris exponent of $m \sim 2$).

As seen in Fig. 2.8, Haynes 230 demonstrated planar slip. Planar slip is commonly associated with solid solution hardened nickel-based superalloys and is encouraged by the inclusion of tungsten which reduces the stacking fault energy. This characteristic of the alloy leads to decreased slip irreversibility which reduces the fatigue crack growth rate [41]. Mughrabi quantified the cyclic slip irreversibility as the ratio between the irreversible plastic shear slip and the total cumulative plastic shear slip [42]. This idea was the basis of the measurements made in Section 2.3.2. The results concurred with Mughrabi and showed increasing fatigue crack growth rates with increasing slip irreversibility.

A relationship exists between the slip irreversibilites, crack growth rates, and temperature as the irreversibilities and growth rates were an order of magnitude higher for the HT case compared to the RT case. Since the cyclic frequency was high enough to minimize creep effects, the high temperature effects on dislocation motion must be elucidated. Increased temperature increases the cross-slip of screw dislocations and reduces the reversible slip since they will no longer return on that glide plane [42]. Dislocation climb, vacancies, and the annihilation of dislocations all prevent the return of dislocations to the crack tip [43, 44]. The addition of this high temperature plastic flow has a direct influence on the slip irreversibility and therefore directly impacts the fatigue crack growth rate. It has also been well established that subgrain formation occurs at high temperatures since the first observations in 1935 [45]. Since subgrains have a slightly different orientation compared to the surrounding material, the slip planes will be realigned. This creates a discontinuity of slip [46]. Previous research has indicated that the presence of barriers which prohibit the reverse of slip during the unloading portion of a fatigue cycle will increase the amount of slip [19]. The increased amount of subgrains present at HT compared to RT would indicate a much higher amount of slip irreversibility as was found. This is evident by the much higher fatigue crack growth rate of the HT specimen compared to the RT specimen as shown in Fig. 2.3.

This study provided quantitative, experimental evidence that slip irreversibility is able to describe the fatigue crack growth rate differences between experiments with differing temperatures.

2.5 Summary

- The fatigue crack growth of Haynes 230 was studied at room temperature (RT) and high temperature (HT). Analysis focused on the significance of any crack closure and the crack tip slip irreversibility and how these two phenomena related to the crack growth rates.
- The material showed good fatigue crack growth resistance both in the RT and HT tests ($m \sim 2$) although the HT fatigue crack grew at an appreciably faster rate. The role of microstructure is manifested through the irreversibility of slip at the crack tip.
- Crack closure levels of approximately 30% of the load were determined at both test temperatures. Plasticity-induced crack closure was the main form of crack closure present and oxide-induced crack closure was not a significant factor in the HT case.
- Slip irreversibility was quantitatively measured as the difference in accumulated strain per cycle at the crack tip, and it was over an order of magnitude higher in the HT case compared to the RT case.
- Dislocations emitted at the crack tip were influenced by high temperature effects as reflected in the slip irreversibility measurements. Quantitative measurements of slip irreversibility were found to be an accurate method to distinguish the differences between the differences of crack growth rates at HT and RT.

2.6 References

[1] A.J. McEvily Jr. On Crack Closure in Fatigue Crack Growth, Mechanics of Fatigue Crack Closure, ASTM STP - 982 (1988) 35-43.

[2] J. Schijve. Fatigue crack closure: observations and technical significance, ASTM STP - 982 (1988) 5-34.

[3] J. Carroll, C. Efstathiou, J. Lambros, H. Sehitoglu, B. Hauber, S. Spottswood, R. Chona. Investigation of fatigue crack closure using multiscale image correlation experiments, Engineering Fracture Mechanics 76 (2009) 2384.

[4] W.T. Riddell, R.S. Piascik, M.A. Sutton, W. Zhao, S.R. McNeill, J.D. Helm. Determining fatigue crack opening loads from near-crack-tip displacement measurements, ASTM STP - 1343 (1999) 157.

[5] M.A. Sutton, W. Zhao, S.R. McNeill, J.D. Helm, R.S. Piascik, W.T. Riddell. Local crack closure measurements: Development of a measurement system using computer vision and a far-field microscope, ASTM STP - 1343 (1999) 145.

[6] M.D. Sangid, G.J. Pataky, H. Sehitoglu, R.F. Hamilton, H.J. Maier. High resolution analysis of opening and sliding in fatigue crack growth, International Journal of Fatigue 37 (2011) 134.

[7] B. Tomkins. Fatigue crack propagation-an analysis, Philosophical Magazine 18 (1968) 1041.

[8] F.A. McClintock. On the plasticity of the growth of fatigue cracks, Fracture of Solids (1963) 65-102.

[9] J.R. Rice. The mechanics of crack tip deformation and extension by fatigue, Fatigue Crack Propagation, ASTM STP - 415 (1967).

[10] M.W. Brown, K.J. Miller. Mode I Fatigue Crack Growth under Biaxial Stress at Room and Elevated Temperature, ASTM STP - 853 (1985) 135.

[11] H. Gao, N. Alagok, M.W. Brown, K.J. Miller. Growth of Fatigue Cracks under Combined Mode I and Mode II Loads, ASTM STP - 853 (1985) 184.

[12] R.C. McClung, H. Sehitoglu. On the finite element analysis of fatigue crack closure--2. Numerical results, Engineering Fracture Mechanics 33 (1989) 253.

[13] A.J. McEvily Jr, R.G. Boettner. On fatigue crack propagation in F.C.C. metals, Acta Metallurgica 11 (1963) 725.

[14] P.J.E. Forsyth. Fatigue damage and crack growth in aluminium alloys, Acta Metallurgica 11 (1963) 703.

[15] C. Fong, D. Tromans. High frequency stage I corrosion fatigue of austenitic stainless steel (316L), Metallurgical and Materials Transactions A 19 (1988) 2753.

[16] R. Pippan. Dislocation emission and fatigue crack growth threshold, Acta Metallurgica et Materialia 39 (1991) 255.

[17] R. Pippan. The condition for the cyclic plastic deformation of the crack tip: the influence of dislocation obstacles, International Journal of Fracture 58 (1992) 305.

[18] X. Wu, A. Koul, A. Krausz. A transgranular fatigue crack growth model based on restricted slip reversibility, Metallurgical and Materials Transactions A 24 (1993) 1373.

[19] M.D. Sangid, G.J. Pataky, H. Sehitoglu, R.G. Rateick, T. Niendorf, H.J. Maier. Superior fatigue crack growth resistance, irreversibility, and fatigue crack growth microstructure relationship of nanocrystalline alloys, Acta Materialia 59 (2011) 7340.

[20] M. Sutton, J.-J. Orteu, H. Schreier. Image Correlation for Shape Motion and Deformation Measurements: Basic Concepts, Theory and Applications, Spring Media, 2009.

[21] M.A. Sutton, W.J. Wolters, W.H. Peters, W.F. Ranson, S.R. McNeill. Determination of displacements using an improved digital correlation method, Image and Vision Computing 1 (1983) 133.

[22] H. Tada, P.C. Paris, G.R. Irwin. The stress analysis of cracks handbook, Del Research Corp., Hellertown, Pa, 1973.

[23] S. Suresh. Fatigue of materials, Cambridge University Press, Cambridge, UK, 1991.

[24] T.L. Anderson. Fracture Mechanics: Fundamentals and Applications, second ed., CRC Press, Boca Raton, 1994.

[25] D. Kim, C. Jang, W. Ryu. Oxidation Characteristics and Oxide Layer Evolution of Alloy 617 and Haynes 230 at 900 °C and 1100 °C, Oxidation of Metals 71 (2009) 271.

[26] M. Kun, L. Gianfranco, T. Hsiao-Ming, C. Xiang, F.S. James. High Temperature Aging and Corrosion Study on Alloy 617 and Alloy 230, Journal of Engineering for Gas Turbines and Power 133 (2011) 052908.

[27] V. Gerold, H.P. Karnthaler. On the origin of planar slip in f.c.c. alloys, Acta Metallurgica 37 (1989) 2177.

[28] M. Gell, G.R. Leverant. Mechanisms of High-Temperature Fatigue, Fatigue at Elevated Temperatures ASTM STP - 520 (1973) 37-67.

[29] R.H. Christensen. Fatigue crack growth affected by metal fragments wedged between opening-closing crack surfaces, Applied Materials Research 2 (1963) 207.

[30] W. Elber. Fatigue crack closure under cyclic tension, Engineering Fracture Mechanics 2 (1970) 37.

[31] W. Elber. The Significance of Fatigue Crack Closure, ASTM STP - 486 (1971) 230.

[32] H.U. Staal, J.D. Elen. Crack closure and influence of cycle ratio R on fatigue crack growth in type 304 stainless steel at room temperature, Engineering Fracture Mechanics 11 (1979) 275.

[33] S. Lee, Y. Lu, P. Liaw, H. Choo, S. Thompson, J. Blust, P. Browning, A. Bhattacharya, J. Aurrecoechea, D. Klarstrom. High-temperature tensile-hold crack-growth behavior of Hastelloy X alloy compared to HAYNES 188 and HAYNES 230 alloys, Mechanics of Time-Dependent Materials 12 (2008) 31.

[34] Y.L. Lu, L.J. Chen, P.K. Liaw, G.Y. Wang, C.R. Brooks, S.A. Thompson, J.W. Blust, P.F. Browning, A.K. Bhattacharya, J.M. Aurrecoechea, D.L. Klarstrom. Effects of temperature and hold time on creep-fatigue crack-growth behavior of HAYNES 230 alloy, Materials Science and Engineering: A 429 (2006) 1.

[35] S. Suresh, G. Zamiski, D. Ritchie. Oxide-Induced Crack Closure: An Explanation for Near-Threshold Corrosion Fatigue Crack Growth Behavior, Metallurgical and Materials Transactions A 12 (1981) 1435.

[36] P.K. Liaw, T.R. Leax, R.S. Williams, M.G. Peck. Influence of oxide-induced crack closure on near-threshold fatigue crack growth behavior, Acta Metallurgica 30 (1982) 2071.

[37] J.E. King. Surface damage and near-threshold fatigue crack growth in a Ni-base superalloy in vacuum, Fatigue & Fracture of Engineering Materials & Structures 5 (1982) 177.

[38] R.O. Ritchie, S. Suresh, C.M. Moss. Near-Threshold Fatigue Crack Growth in 2 1/4 Cr-1Mo Pressure Vessel Steel in Air and Hydrogen, Journal of Engineering Materials and Technology 102 (1980) 293.

[39] T. Ezaz, M.D. Sangid, H. Sehitoglu. Energy barriers associated with slip-twin interactions, Phil. Mag. 91 (2007) 1464.

[40] Y. Gao, R. Ritchie, M. Kumar, R. Nalla. High-cycle fatigue of nickel-based superalloy ME3 at ambient and elevated temperatures: Role of grain-boundary engineering, Metallurgical and Materials Transactions A 36 (2005) 3325.

[41] N.F. Mott. A theory of the origin of fatigue cracks, Acta Metallurgica 6 (1958) 195.

[42] H. Mughrabi. Cyclic Slip Irreversibilities and the Evolution of Fatigue Damage, Metallurgical and Materials Transactions A 40 (2009) 1257.

[43] A. Pineau, S.D. Antolovich. High temperature fatigue of nickel-base superalloys - A review with special emphasis on deformation modes and oxidation, Engineering Failure Analysis 16 (2009) 2668.

[44] F. Ellyin. Fatigue Damage, Crack Growth and Life Prediction, Springer, 1996.

[45] C.H.M. Jenkins, G.A. Mellor. Investigation of behaviour of metals under deformation at high temperatures -- 1, J. Iron Steel Inst. 132 (1935) 179.

[46] S. Manson. Fatigue: A complex subject—Some simple approximations, Experimental Mechanics 5 (1965) 193.

Chapter 3. Creep of Haynes 230 at 800 °C and 900 °C

[Note: The material in this chapter has been published as Pataky *et al.*, Journal of Nuclear Materials, doi:10.1016/j.jnucmat.2013.08.009]

3.1 Background

The intermediate heat exchangers in the NGNP must be able to operate at temperatures of 900 °C and above, putting a huge demand on the materials employed. A great amount of knowledge is still needed to understand how Haynes 230 creeps before it can be implemented to operate at these high temperatures. Of particular interest is the deterioration of the material between 800 °C and 900 °C.

Voids were first identified in crept materials over a half century ago [1, 2]. Further studies by Greenwood found these cavities, based on the sliding of the grain boundaries, led to the failure of the material [3, 4]. Using a comprehensive collection of data, isothermal fracture maps separating intergranular and transgranular fracture based on temperature and loading were constructed [5]. These maps were also able to indicate what creep mechanism was most likely to be dominant. In the present study, the creep damage created voids, which subsequently led to large localized deformation in the material, and thus the material exhibited mostly intergranular failure, as predicted due to the temperatures and stresses the samples were subjected to.

Two main areas of focus for failure along grain boundaries are triple junctions and precipitates. Both of these can lead to stress concentrations caused by grain boundary sliding during creep conditions [6]. Argon, Chen, and Lau modeled these two forms of grain boundary decohesion which had been previously experimentally observed [7]. Precipitates on the grain boundaries restrict the sliding of the grain boundaries during transient loading, while triple junctions tend to dominate as stress concentrations once the load supported by these precipitates reaches a critical limit. Using stress functions and power-law creep, singularities around the triple junctions and precipitates were modeled [8]. This was also implemented in a finite element model study [9]. The presence of carbides in nickel-based superalloys, in

particular Haynes 230, on grain boundaries can cause serrations of grain boundaries [10], acting as particles restricting grain boundary sliding.

Haynes 230 has been the focus of many studies and its deformation behavior is still being characterized. Since the material will be used at elevated temperatures, oxidation rates were studied and Haynes 230 was found to have a high oxidation resistance [11, 12]. Fatigue crack growth behavior has been studied at room temperature and elevated temperatures, showing a decrease in the crack growth resistance as temperature rises [13-15]. The creep-fatigue behavior was recently discussed by Chen *et al.* and Haynes 230 exhibited greater fatigue-creep life than Alloy 617 [16]. At increased hold times during the creep-fatigue cycle, the life was observed to decrease in Haynes 230. The creep behavior was recently investigated and compared to that of Haynes 282 up to 815 °C [17]. Haynes 282 showed significantly greater creep resistance than Haynes 230.

The current study advances our understanding of the creep behavior that Haynes 230 exhibits by comparing experimental results at 800 °C and 900 °C. The minimum creep rates were used to contrast the two temperatures in terms of deformation mechanisms. To better understand how the microstructure deforms, high resolution digital image correlation, along with optical images of the microstructure, was utilized to identify the areas of the microstructure prone to developing strain concentrations during deformation. Other studies have shown that grain boundary serrations lead to a lower creep rate in nickel-based superalloys [18, 19]. The present study has found a concentration of strain at these serrations, which may impede grain boundary sliding. Strain concentrations were also identified at triple junctions. The current study quantifies these strain concentrations and discusses the large difference in the creep behavior between 800 °C and 900 °C.

3.2 Material Preparation and Experimental Procedure

3.2.1 Material Preparation

This study used commercially available Haynes 230 with details about the alloy provided in Section 1.2.2.1.

Since DIC was used to capture the displacements of the deformed specimens, the specimen surfaces had to be prepared with a speckle pattern. Two separate procedures were used since this study included both *in-situ* and *ex-situ* experiments. For the *in-situ* samples, the preparation was the same as the HT specimen preparation in Section 2.2.1.

For the *ex-situ*, high resolution DIC samples, the surface was mechanically polished to a mirror finish using abrasive paper and a final step of 0.3 micron silica powder. The sample was then heated in an oven at 900 °C for 7 minutes and water quenched. The small layer of oxidation that formed allowed for the grain boundaries to be visible under an optical microscope. An area was marked off, and optical images were taken using the microscope at a magnification of 10x, with a resolution of 0.437 µm/pix, to provide insight into the microstructure. The sample was then prepared using the *in-situ* procedure. Another set of optical images at 10x were captured as the reference images for DIC. This type of sample will be referred to as the *ex-situ* sample.

3.2.2 Experimental Procedure

A servo-hydraulic load frame with a 7.5 kN load cell was used during the experiments and the specimens were heated using induction heating. A type-K thermocouple was welded in the middle of the back of the gauge section. All experiments were performed in air. The temperature of the specimens was raised from room temperature to either 800 °C or 900 °C at a rate of 75 °C per minute. The temperate was kept within a tolerance of ±3 °C for the duration of the experiments using a temperature controller connected to the induction heater. The specimen surface was illuminated using white light. DIC images were captured at a rate of an image every 30 seconds. The camera field of view was 4.00 mm by 3.00

mm. For the *in-situ* experiments, images were captured throughout the entire experiment until failure or the test was suspended. A photograph of the experimental setup is shown in Fig. 3.1. The *ex-situ* tests were halted after a predetermined time in order to capture images using the optical microscope. These images were captured in the same area as the pre-test images. The entire visible area of the deformed images was correlated back to the original, undeformed reference images using a commercially available image correlation program. The horizontal and vertical displacements were differentiated using a small strain assumption in order to find the strain fields. By correlating two undeformed images, an estimation of the experimental errors was made. The average measure of noise in the strain was 5×10^{-4} with a maximum local noise value of 0.002. For more information on the high resolution, *ex-situ* DIC, see reference [20].

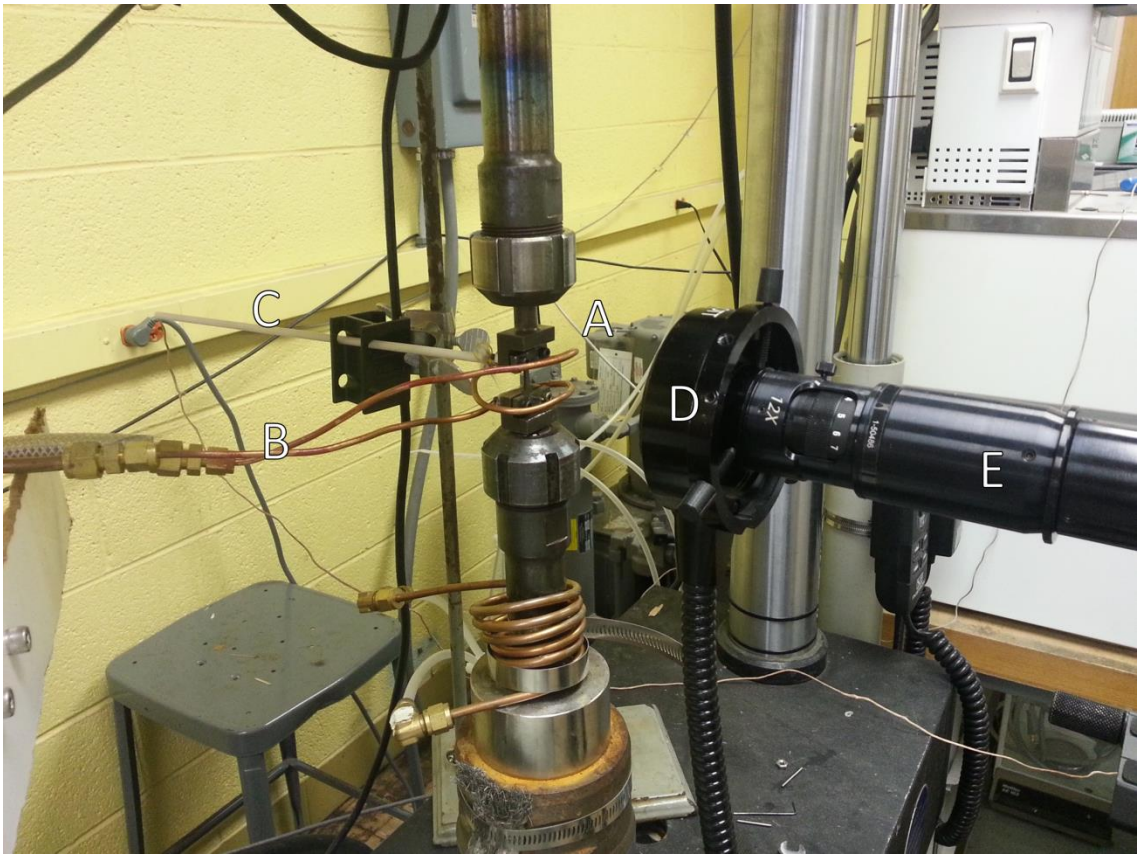

Fig. 3.1 - The experimental setup. A - Specimen in the load frame, B - Induction coils, C - Type-K thermocouple, D – White Light Illumination, E - Lens and Camera.

For transmission electron microscopy (TEM) 1 mm thick discs were sectioned with a low-speed diamond saw parallel to the loading axis from the failed specimens, and then mechanically ground and polished down to 0.15 mm foil thickness. Large electron transparent areas were obtained in these foils by conventional twin jet polishing using a solution consisting of 5% perchloric acid in ethanol at -20 °C and 15 V. The TEM was operated at a nominal voltage of 200 kV and a double-tilt specimen holder was employed for imaging under two-beam conditions.

3.3 Results

3.3.1 Creep Results

The creep tests were conducted at relatively high stresses for the temperatures considered in order to produce creep strains in a reasonable time period. The results of these creep tests are presented in Fig. 3.2. The strains in this figure are the averaged DIC axial strains found in the area imaged during the experiments. There is a noticeable difference in behavior between the two high temperatures. In the 900 °C experiments (Fig. 3.2a), the secondary creep lasts for a few minutes in each of the tests. Almost the entire creep curve consists of tertiary creep. Surface damage and voids were visible early on in the experiments, consistent with the damage expected. Contrary to these results, the 800 °C experiments (Fig. 3.2b) had prolonged periods of secondary creep. The tests performed at stresses of 50 and 75 MPa were halted before the samples failed. The visible surface damage that was present in the 900 °C experiments was not present in the 800 °C experiments.

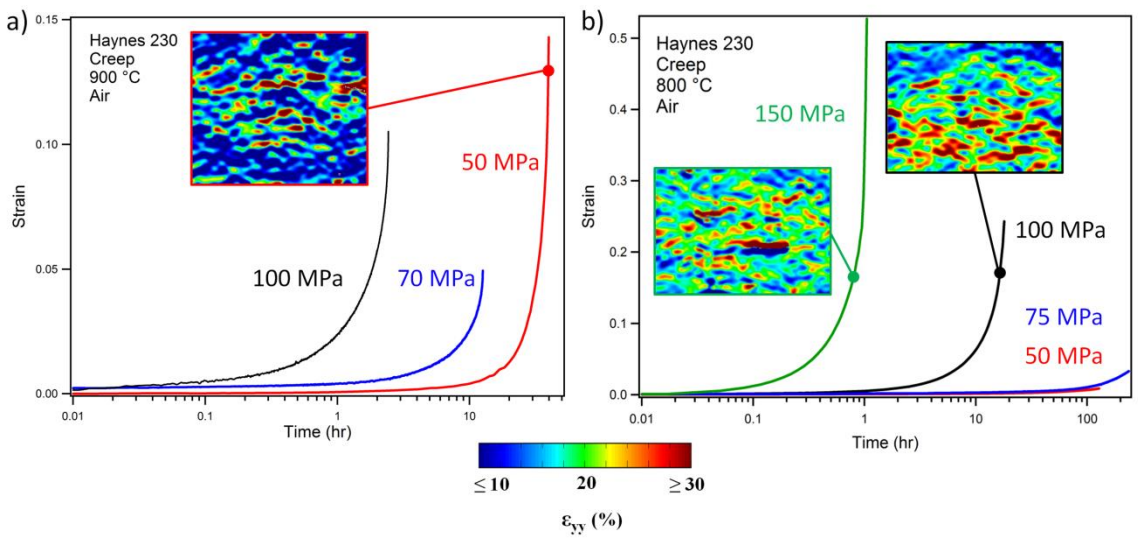

Fig. 3.2 - Strain versus time data for creep tests of Haynes 230 at 800 °C and 900 °C at several load levels. Steady state creep is more readily observed in the 800 °C samples while both temperatures show localized strains greater than 30%.

Further information concerning the strains developed during creep was found using high resolution *ex-situ* DIC. Two samples of Haynes 230 were crept at 900 °C with a stress of 50 MPa for 2 hours and 10 hours each. After the test was suspended, the material was unloaded and cooled to room temperature leaving residual plastic strains to be measured with DIC. The average axial strain was 0.26% for the 2 hours sample and 0.88% for the 10 hours sample. The two main areas of strain concentration were focused around serrated grain boundaries and triple junctions. The sample suspended at 2 hours showed less strain concentration than the 10 hours sample, consistent with the increasing average strain. DIC was used to quantitatively obtain the trend of strain distribution at these two points, and showed a peak at the serrated grain boundary and triple junction, as indicated in Fig. 3.3. The strains measured were tensile strains aligned with the loading direction and were found to be orders of magnitude higher than the average strain of the area. These results showed that there was a trend of increasing strain concentration at magnitudes much higher than the average strain as time progresses, with the peak remaining at the serrated grain boundary or triple junction.

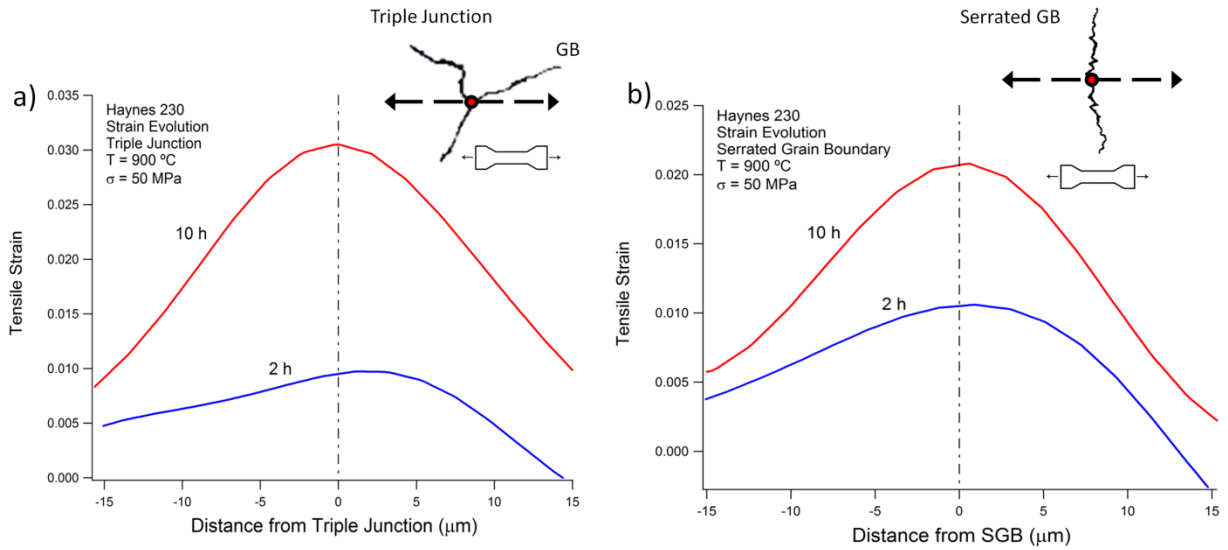

Fig. 3.3 – Axial strain magnitudes as a function of distance found at serrated grain boundaries and triple junctions. The red dot in the schematics shows the 0 μm measurement point for a) triple junctions and b) serrated grain boundaries.

The minimum secondary creep rates, $\dot{\varepsilon}_{ss,min}$, were assumed to follow the fundamental Arrhenius equation,

$$\dot{\varepsilon}_{ss,min} = A(\sigma)^n \tag{3-1}$$

where A is the creep constant, σ is the nominal stress, and n is the creep exponent. In order to better distinguish which mechanism of creep was active, the minimum strain rates for each experiment were plotted against the nominal stress at which the sample was loaded in Fig. 3.4. The constants fitted are given in Table 3.1. Consistent with the creep results, the strain rates also show a difference in behavior between the two high temperatures. At 900 °C, the creep exponent was found to be n = 3.4. This can be approximated to n = 3 where the rate limiting mechanism is dislocation glide, also known as solute drag [21]. At 800 °C, the creep exponent was found to be n = 5.17, which is representative of dislocation climb (n = 5) being the rate limiting creep mechanism [22].

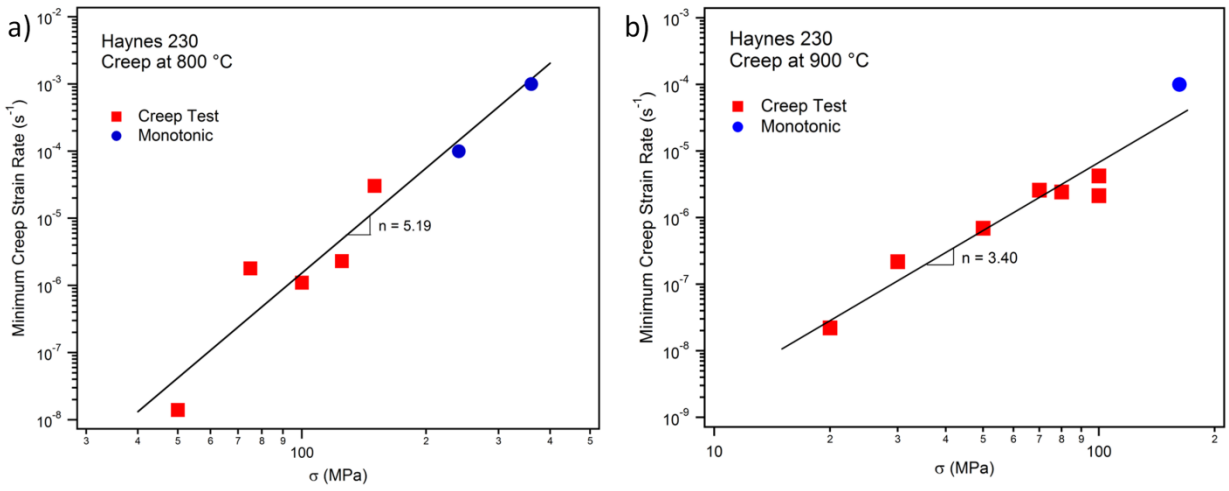

Fig. 3.4 - The minimum creep rate plotted as a function of the applied loading for creep of Haynes 230. The creep at 800 °C corresponds to a creep exponent of n ≈ 5 (dislocation climb mechanism) and the 900 °C results produce a creep exponent of n ≈ 3 (solute drag mechanism).

Table 3.1 - Creep constants summary of Haynes 230

Temp. (°C)	Creep coefficient (A)	Creep exponent (n)
800	6.38E-17	5.19
900	1.89E-09	3.40

3.3.2 SEM of Crept Material

After the samples of Haynes 230 had been crept, scanning electron microscopy (SEM) was performed to analyze the fracture surfaces. First, in analyzing the micrographs in Fig. 3.5 from samples experimented at 900 °C, it is evident that the samples show intergranular failure. In Fig. 3.5a, despite the oxidation, the cracking can be observed along the grain boundaries and several large voids are depicted. In Fig. 3.5b, cracking at a triple junction is apparent. Cracking along grain boundaries is also visible in the upper right portion of the micrograph. This result was to be expected due to the temperature and stresses the sample was subjected to.

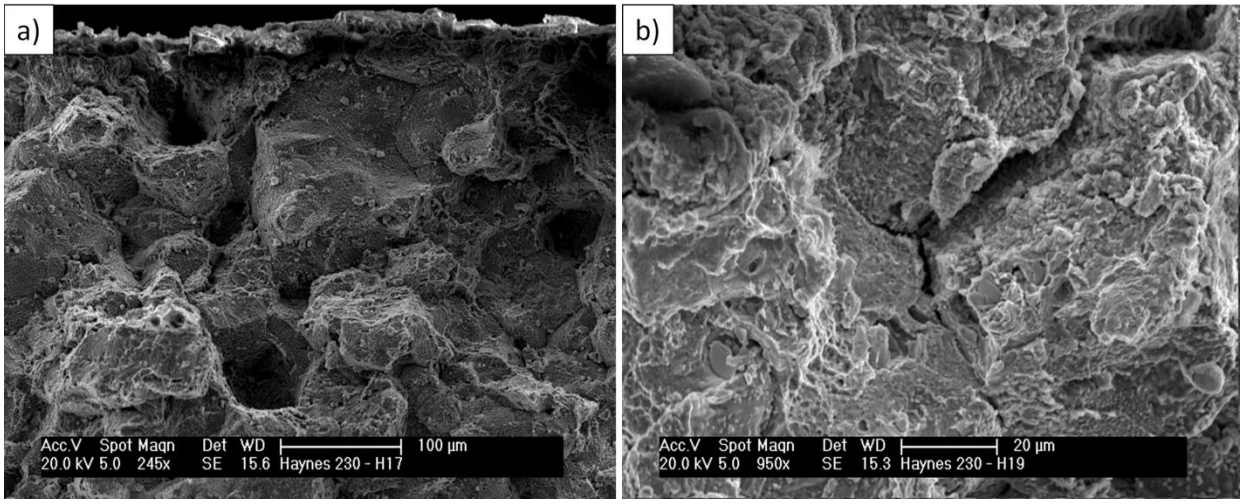

Fig. 3.5 - SEM micrographs of the fracture surface from samples crept at 900 °C. a) Intergranular cracking and voids are evident. b) A cracked triple junction on the fracture surface.

The samples crept at 800 °C showed mainly intergranular fracture, but there was also evidence of transgranular failure along the fracture surface, shown in Fig. 3.6a. Fig. 3.6b depicts a secondary, intergranular crack that formed below the area of failure. This sample had much more ductility than the 900 °C sample, which could contribute to the longer observed creep life. There was also less damage, specifically a lack of large voids, found along the fracture plane in this specimen.

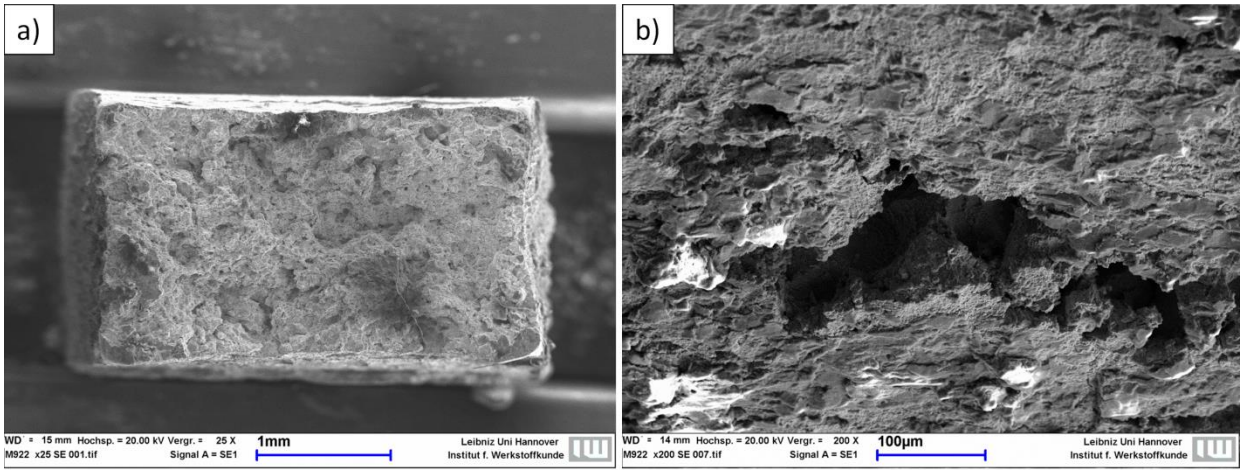

Fig. 3.6 - SEM micrographs of the fracture surface and a secondary crack from a sample crept at 800 °C. a) The fracture surface of the sample showing high levels of ductility and a mixture of intergranular and transgranular cracking. b) A secondary crack below the failed section showing intergranular cracking.

3.4 Discussion

3.4.1 Grain Boundary Serrations and Triple Junctions

The strain heterogeneity at the microscale was investigated for areas of strain concentrations. This was performed using high resolution digital image correlation and observing the strain fields overlaid on the microstructure. The advantage of DIC is that as the magnification is increased, the spatial resolution improves allowing for strain measurements on the microscale [20].

As indicated in the Background (Section 3.1), precipitates in the grain boundaries and triple junctions are known to be sources of failure during creeping conditions. In Haynes 230, these are M_6C and $M_{23}C_6$ carbides. In order to investigate these as potential points of failure, high resolution DIC had to be performed on the sample using the *ex-situ* procedure with preliminary results given in Section 3.3.1. The samples of interest were used in a creep test performed at 900 °C with a nominal stress of 50 MPa and were arrested after 2 hours and 10 hours. DIC was performed, the strain fields were overlaid on the microstructure, and strain concentrations were investigated. The axial strains were investigated as shear strain values were of much lower magnitude.

The resulting strain fields are presented for 2 hours and 10 hours in Fig. 3.7 and Fig. 3.8, respectively. Both figures show strain concentrations on serrated grain boundaries and at triple junctions. This result is consistent with the review presented by Argon [6]. As the grain boundaries slide during creep, the pinning of the serrated grain boundaries by carbides leads to an increase in the stress fields. The triple junctions act as sites of void formation, and if allowed to creep further, the voids would grow and merge with cavitations on the grain boundaries leading to cracks. These are competing processes since the grain boundaries are restricted from sliding by the carbides delaying damage, while the triple junctions indicate the formation of voids.

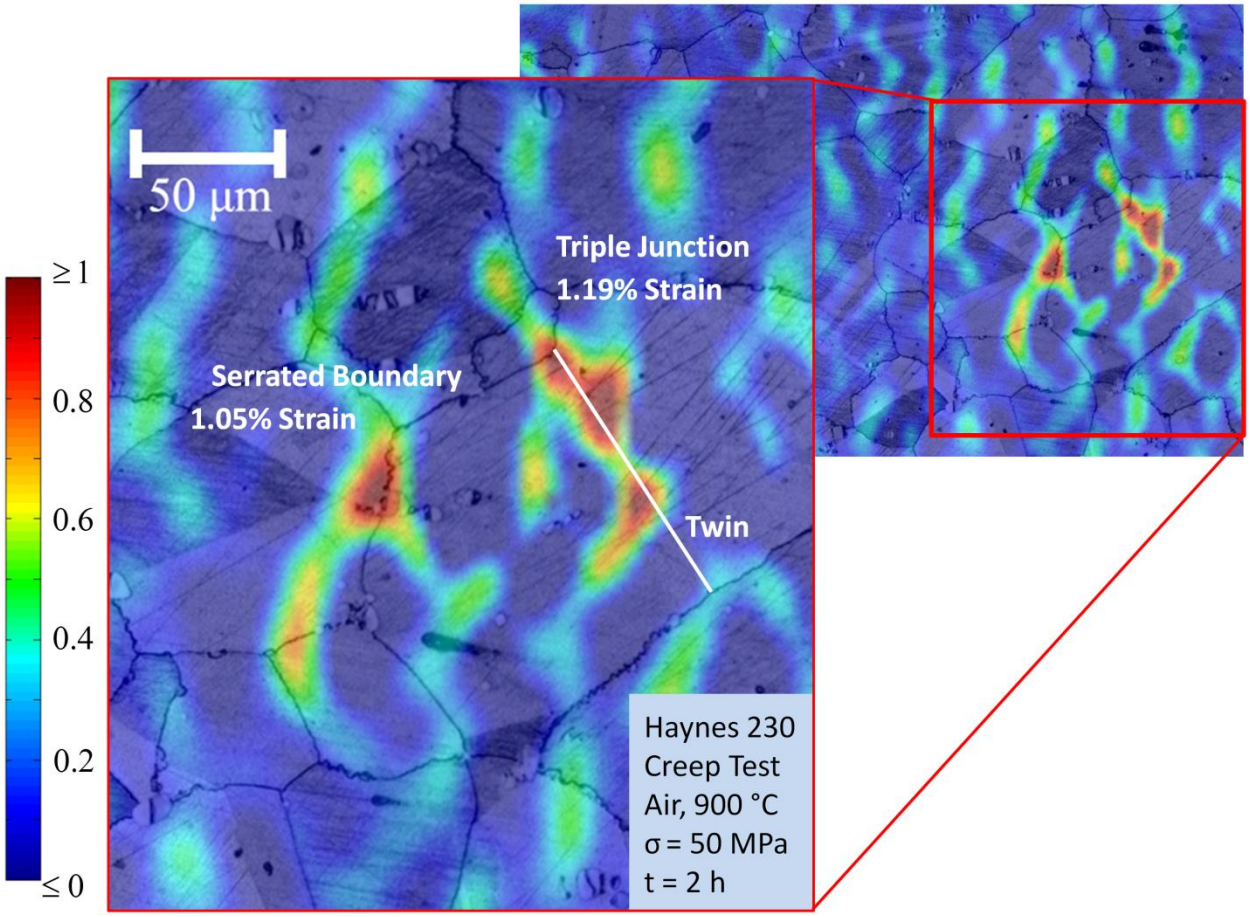

Fig. 3.7 - DIC axial strain field (average strain of 0.26%) after 2 hours of creep at 900 °C with a load of 50 MPa overlaid on an optical micrograph of the microstructure at a magnification of 10x. Two areas of localized strain were observed: on a serrated grain boundary and at the triple junction of a twin and two grain boundaries.

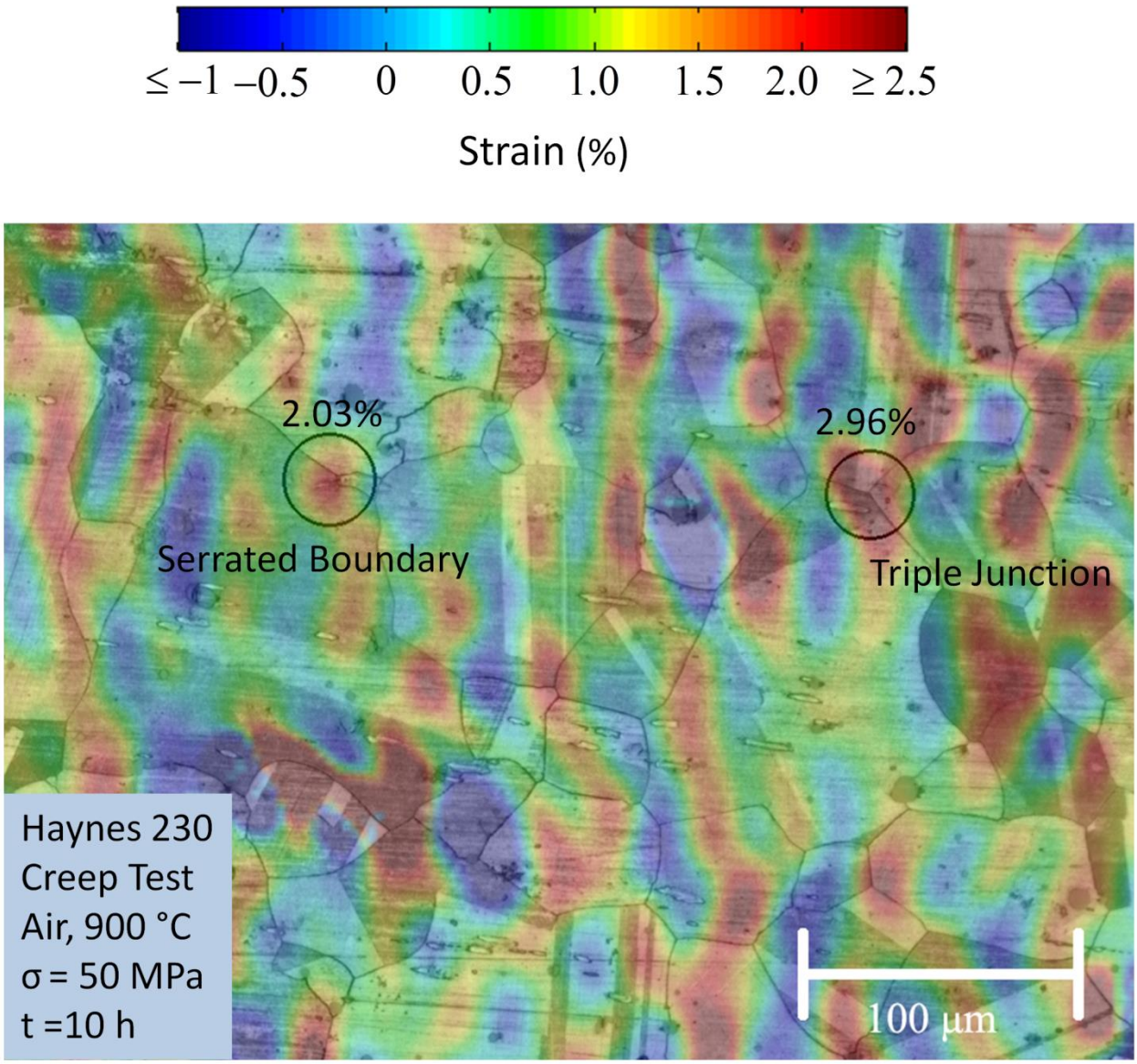

Fig. 3.8 - DIC axial strain field (average strain of 0.88%) after 10 hours of creep at 900 °C with a load of 50 MPa overlaid on an optical micrograph of the microstructure at 10x. High levels of localized strain were found at a triple junction and a serrated grain boundary.

Further discussion of the grain boundaries serrations (GBS) is needed. In a previous study, the serrations in Haynes 230 were found to be caused by $M_{23}C_6$ carbides, where M is mostly chromium [10]. M_6C carbides, with M being mostly tungsten, are also present in Haynes 230, but at solutionizing temperatures, these carbides dissolve introducing a supersaturation of C into the matrix. The supersaturation of C can lead to further nucleation and growth of the $M_{23}C_6$ carbides [10]. Literature

concerning GBS has found that they can lower the creep rate and reduce crack propagation since grain boundary sliding is restricted [18, 19]. This is experimentally observed in the crept Haynes 230 sample as the strains present on the GBS may be due to this restriction of sliding. TEM supporting the presence of carbides at the boundaries is shown in Fig. 3.9. This micrograph depicts dislocation-carbide interactions while the carbides are pinned in the (sub-) grain boundary. Future studies of Haynes 230 are needed to observe how these strains develop during the life of a creeping sample. A heat treatment encouraging the creation of GBS for Haynes 230 by increasing the nucleation and growth of granular $M_{23}C_6$ carbides [10] may lead to decreased creep rates, especially at 900 °C, which could lead to prolong the secondary creep life and expand the use of this superalloy. Further statistical studies of samples with varying amounts of GBS are needed to fully understand their impact on creep life.

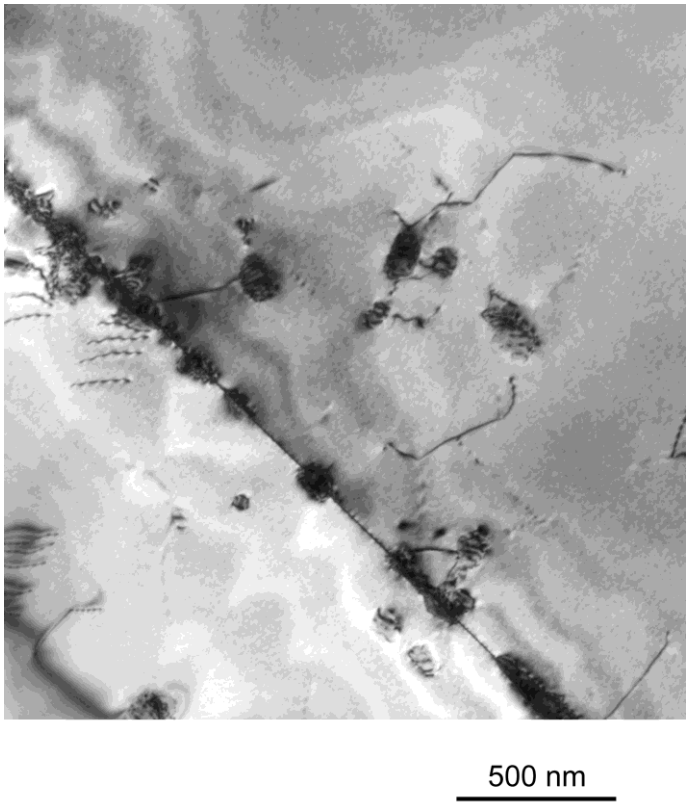

Fig. 3.9 - A TEM micrograph from a sample crept at 900 °C at a stress of 100 MPa showing dislocation-carbide interactions with carbides present in the boundary. The carbides in the grain boundary are the cause of serrated grain boundaries.

3.4.2 Creep Exponents

As previously indicated, Haynes 230 exhibits different mechanisms limiting the creep rate at the different elevated temperatures. Weertman was the first to describe the dislocation activities that led to these two creep mechanisms [21, 22]. Much work has been performed since his discovery in order to describe the differences between the solute drag mechanism and the dislocation climb mechanism. A brief explanation of the two mechanisms is presented below.

A creep exponent of $n \approx 3$, found for the 900 °C creep, is synonymous with solute drag during creep, as originally found by Cottrell and Jawson [23]. In this case, dislocations that are gliding are dragging solute atoms with them limiting the velocity of the gliding. The rate of glide is assumed proportional to the applied stress, and the stress a dislocation applies on its neighbor is inversely proportional to the dislocation density. The three power law proportionality of the creep rate to the applied stress is approximated by the product of the dislocation density, Burgers vector, and the rate of glide [24]. A review of the dragging processes responsible for this mechanism can be found in [25]. Of special note is the proposed dragging process which is due to the segregation of atoms at stacking faults [26]. In Haynes 230, the addition of tungsten lowers the stacking fault energy which could reduce the recovery rate and in consequence, reduce the creep rate [27].

For the creep rate to be proportional to the fifth power, $n \approx 5$, an additional σ^2 must be introduced. Recall that this is representative of the creep occurring at 800 °C. This behavior involves the formation of dislocation networks and sub-grains. As dislocation loops expand by glide and climb, they eventually annihilate, and the interaction of edge and screw dislocations forms dislocation networks. The resulting mixed dislocations in the networks, or subgrain networks, control the rate that vacancies are absorbed and emitted [28]. The diffusion coefficient for the vacancies is then higher in the dislocation network than that of the bulk. Due to the cross-sectional area of the dislocation pipes, distance between the pipes, and differences in diffusion coefficients between the network and bulk, the addition proportionality was acquired [24]. Now if the sub-grain bowing is added as the internal stress, the creep

exponent for power-law creep can be found to be 5 [29]. TEM was performed to identify the presence of subgrains in the specimen crept at 800 °C, shown in Fig. 3.10. In this figure, dislocations have formed a sub-grain boundary. From the previous analysis, it can be stated that the addition of dislocation networks and sub-grains are possible reasons for the difference between the creep mechanisms in the two elevated temperature experiments.

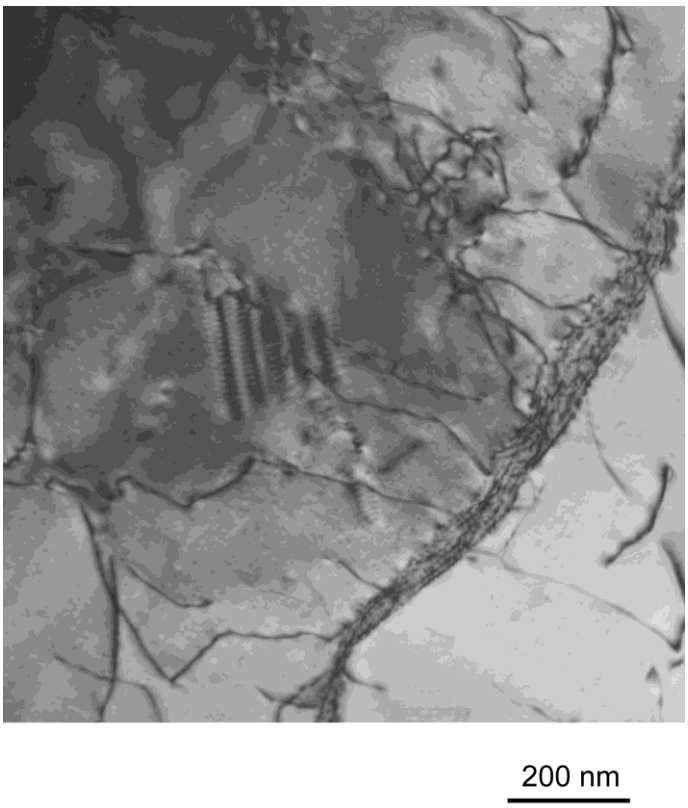

Fig. 3.10 - A TEM micrograph showing a subgrain formed during creep at 800 °C at a stress of 75 MPa.

3.5 Summary

The creep behavior of Haynes 230 was investigated in this study at two elevated temperatures. The main findings can be summarized as follows:

- At the stresses employed, at 900 °C the material spent a majority of its life in the tertiary creep regime, while the 800 °C results had periods of prolonged secondary creep. Intergranular failure was observed in all samples.
- The stress exponent was found to be $n \approx 3$ at 900 °C, indicating solute drag as the creep mechanism, and $n \approx 5$ at 800 °C, indicating dislocation climb as the main creep mechanism.
- Using high resolution digital image correlation overlaid on the microstructure, strain concentrations were found at triple junctions and grain boundary serrations.
- The grain boundary serrations restrict grain boundary sliding and may be an effective tool to prolong the life of Haynes 230 in creeping conditions.

3.6 References

[1] C.H.M. Jenkins, E.H. Bucknall, E.A. Jenkinson. The inter-relation of age-hardening and creep performance. Part II - The behavior in creep of an alloy containing 3 percent nickel and silicon in copper, Journal of the Institute of Metals 70 (1944).

[2] M.E. Whitaker, E. Voce, A.R. Bailey. Intercrystalline failure of brasses and aluminum brasses in air, ammonia, and certain aqueous solutions and molten metals, Metallurgia 39 (1948).

[3] J.N. Greenwood. Intercrystalline cracking of metals, Journal of the Iron and Steel Institute 171 (1952).

[4] J.N. Greenwood, D.R. Miller, J.W. Suiter. Intergranular cavitation in stressed metals, Acta Metallurgica 2 (1954) 250.

[5] M.F. Ashby, C. Gandhi, D.M.R. Taplin. Overview No. 3 Fracture-mechanism maps and their construction for f.c.c. metals and alloys, Acta Metallurgica 27 (1979) 699.

[6] A.S. Argon. Mechanics and mechanisms of fracture in creeping alloys. in: Owen BWaDRJ, (Ed.). Recent Advances in Creep and Fracture of Engineering Materials and Structures. Pineridge Press, Swansea, 1982. pp. 1.

[7] A.S. Argon, I.W. Chen, C.W. Lau. Intergranular cavitation in creep: theory and experiments. Creep-Fatigue-Environment Interations. Milwaukee, WI, 1979. p.46-83.

[8] C.W. Lau, A.S. Argon. Stress concentration caused by grain boundary sliding in metals undergoing power-law creep. In: Taplin DMR, (Ed.). Proc. Int. Fracture Conference, vol. 2. Waterloo, Canada: Univeristy of Waterloo Press, 1977. p.595.

[9] C.W. Lau, A.S. Argon, F.A. McClintock. Application of the finite method in micromechanical analyses of creep fracture problems, Computers & Structures 17 (1983) 923-931.

[10] L. Jiang, R. Hu, H. Kou, J. Li, G. Bai, H. Fu. The effect of M23C6 carbides on the formation of grain boundary serrations in a wrought Ni-based superalloy, Materials Science and Engineering: A 536 (2012) 37.

[11] D. Kim, C. Jang, W. Ryu. Oxidation Characteristics and Oxide Layer Evolution of Alloy 617 and Haynes 230 at 900 °C and 1100 °C, Oxidation of Metals 71 (2009) 271.

[12] M. Kun, L. Gianfranco, T. Hsiao-Ming, C. Xiang, F.S. James. High Temperature Aging and Corrosion Study on Alloy 617 and Alloy 230, Journal of Engineering for Gas Turbines and Power 133 (2011) 052908.

[13] P.K. Liaw, T.R. Leax, R.S. Williams, M.G. Peck. Influence of oxide-induced crack closure on near-threshold fatigue crack growth behavior, Acta Metallurgica 30 (1982) 2071.

[14] Y.L. Lu, P.K. Liaw, G.Y. Wang, M.L. Benson, S.A. Thompson, J.W. Blust, P.F. Browning, A.K. Bhattacharya, J.M. Aurrecoechea, D.L. Klarstrom. Fracture modes of HAYNES 230 alloy during fatigue-crack-growth at room and elevated temperatures, Materials Science and Engineering: A 397 (2005) 122.

[15] G.J. Pataky, H. Sehitoglu, H.J. Maier. High temperature fatigue crack growth of Haynes 230, Materials Characterization 75 (2013) 69.

[16] X. Chen, M.A. Sokolov, S. Sham, D.L. Erdman Iii, J.T. Busby, K. Mo, J.F. Stubbins. Experimental and modeling results of creep-fatigue life of Inconel 617 and Haynes 230 at 850 °C, Journal of Nuclear Materials 432 (2013) 94.

[17] C.J. Boehlert, S.C. Longanbach. A comparison of the microstructure and creep behavior of cold rolled HAYNES 230 alloy and HAYNES 282 alloy, Materials Science and Engineering: A 528 (2011) 4888.

[18] J.M. Larson, S. Floreen. Metallurgical factors affecting the crack growth resistance of a superalloy, Metallurgical Transactions A 8 (1977) 51-55.

[19] M. Zhiping, Y. Ruizeng, G. Liang. Effect of zigzag grain boundary on creep and fracture behaviours of wrought γ' strengthened superalloy, Materials Science and Technology 4 (1988) 540.

[20] J. Carroll, W. Abuzaid, J. Lambros, H. Sehitoglu. An experimental methodology to relate local strain to microstructural texture, Review of Scientific Instruments 81 (2010) 083703.

[21] J. Weertman. Theory of Steady-State Creep Based on Dislocation Climb, Journal of Applied Physics 26 (1955) 1213-1217.

[22] J. Weertman. Steady-State Creep through Dislocation Climb, Journal of Applied Physics 28 (1957) 362-364.

[23] A.H. Cottrell, M.A. Jawson. Distribution of Solute Atoms Round a Slow Dislocation, Proceedings of the Royal Society A 199 (1949) 104-114.

[24] F.R.N. Nabarro, H.L. de Villiers. The Physics of Creep: Creep and Creep-resistant Alloys, Taylor & Francis, London, 1995.

[25] M.E. Kassner, M.-T. Pérez-Prado. Five-power-law creep in single phase metals and alloys, Progress in Materials Science 45 (2000) 1-102.

[26] H. Suzuki. Segregation of Solute Atoms to Stacking Faults, Journal of the Physical Society of Japan 17 (1962) 322-325.

[27] C.K.L. Davies, P.W. Davies, B. Wilshire. The effect of variations in stacking-fault energy on the creep of nickel-cobalt alloys, Philosophical Magazine 12 (1965) 827.

[28] M.M. Myshlyaev. Dislocation Creep, Annual Review of Materials Science 11 (1981) 31-50.

[29] A.S. Argon, S. Takeuchi. Internal stresses in power-law creep, Acta Metallurgica 29 (1981) 1877.

Chapter 4. Elevated Temperatures *ex-situ* Procedure

4.1 Background

Chapter 3 contains the first high resolution DIC results for Haynes 230. Although informative about local strain concentrations, the study lacked the addition of microstructural information from EBSD. In addition, the speckle pattern was not applied to the surface itself, but onto a thin layer of white paint. Degradation of the paint due to high temperature conditions was present, and thus a more robust procedure was required for further studies. Using this as motivation, an *ex-situ* procedure was developed that builds off the previously established method used in Carroll *et al.* [1]. Further background information follows, including a reaffirmation of why the DIC technique was chosen and the necessity for these high resolution DIC studies.

To assist the development of physically based models, there is a need to experimentally study strain heterogeneities at the sub-grain level [2-4]. There have been continual developments to increase the resolution of measurement techniques in order to meet this demand. Many studies have successfully linked strains to the microstructure using electron back-scatter diffraction (EBSD). Currently, there are few high resolution experimental studies performed on materials deformed at high temperatures [5, 6].

Two experimental, optical methods have emerged as being useful for studying strain heterogeneities. The first method is a grid method used by several researchers [7-9]. An explanation of this displacement measurement technique can be found in [10]. The problem with this measurement technique is that localized high gradients have been found to be difficult to detect [7]. The current study aims to observe the strain heterogeneities across grain boundaries, twin boundaries, and carbides, and thus the ability to measure these high gradients is extremely important. The second method to experimentally measure displacements is DIC. Instead of tracking a grid during deformation, DIC uses the light intensity of each pixel in the full-field, separated into unique boxes called subsets, to quantitatively measure displacements. There is no inherent length scale for DIC and a higher resolution measurement is

produced by increasing the magnification of the images captured. This allows for sub-grain level measurements without a large grain size.

Two approaches to the DIC experiments are possible. *In-situ* provides measurements during loading without having to remove the specimen in order to capture images. The issue with the *in-situ* approach is that it generally must be performed at lower magnifications in order to avoid being affected by vibrations causing blurring of the images. In order to circumvent this issue, special load frames have been used in conjunction with SEM or optical microscopes [9, 11, 12]. There is a limitation to this though; it is difficult to produce high temperature experiments without damaging the equipment and specimen geometries are limited. The other approach, *ex-situ*, is not limited by the experimental setup or environment, including high temperature, since the sample is removed from the testing apparatus before imaging. This method can be performed either optically or in an SEM. Optical microscopes are limited in their depth of focus, which is detrimental in the case of out of plane displacements. Using an SEM, higher magnifications can be achieved, but this is not without its own issues. Two of the major problems are drift during image capture and background noise affecting the pattern [13]. An optical microscope was used in this study in order to circumvent these drawbacks since out of plane displacements will be small.

The present study will introduce a high resolution DIC *ex-situ* experimental methodology for studying materials deformed at high temperatures. The strain fields of a predetermined area will be measured and related to the microstructure using data found from EBSD.

4.2 Sample Preparation

In order to perform EBSD and get information about the microstructure, the samples must be polished to a mirror finish. The specimens used during this study were described in Section 1.2.2.1. This procedure is not limited by the specimen shape or size, thus any specimen can be used. The samples were

mechanically polished with abrasive grinding paper up to a grit of P4000. The sample was then polished using 0.3 µm silica powder and finalized with a vibropolisher.

Before the microstructure was characterized, the area of interest on the sample surface needed to be marked. A discussion of the requirements for these marks is given by Carroll *et al.* with Vickers indentation marks being determined as ideal [1]. The main requirements of these markings were that they need to last throughout the entirety of the experiment so all data sets can be linked, and they must be small enough to align with the microstructure. A Vickers mark was made in each corner of the area of interest. A fifth mark was made next to one of the corners to discern the alignment of the area. EBSD was then able to be performed in an SEM. If necessary, multiple scans can be made and stitched together to study a larger area.

The next step of the experiment was to speckle the sample surface in order to use DIC. This was a major area of concern since anything on the surface can be destroyed by the elevated temperatures, thus destroying the speckle pattern. There are two requirements that must be met. First, the speckles of the pattern must be small enough in order to produce sub-grain quality measurements. Second, the material deposited on the surface must be able to withstand the temperature of the experiment as well. Depositing particles onto the surface using compressed air was identified as the best method, as first used by Jonnalagadda *et al* [14]. This is due to the consistency that a pattern can be made without introducing random oversized speckles, as seen with spray paint. In addition, particles come in a large range of materials allowing flexibility for selecting a deposition material in order to avoid surface reactions. Two types of particles were tested for this application: 1 µm diameter Si and 0.3 µm alumina in Fig. 4.1. Once deposited on the surface, both types of particles provided good DIC speckle patterns, Si shown in Fig. 4.1a and alumina shown in Fig. 4.1b. After heating to 800 °C in vacuum, it was immediately obvious that the Si would not be suitable for this application (Fig. 4.1c) but the alumina remained unchanged (Fig. 4.1d). This example elaborates upon the second requirement for the speckle material.

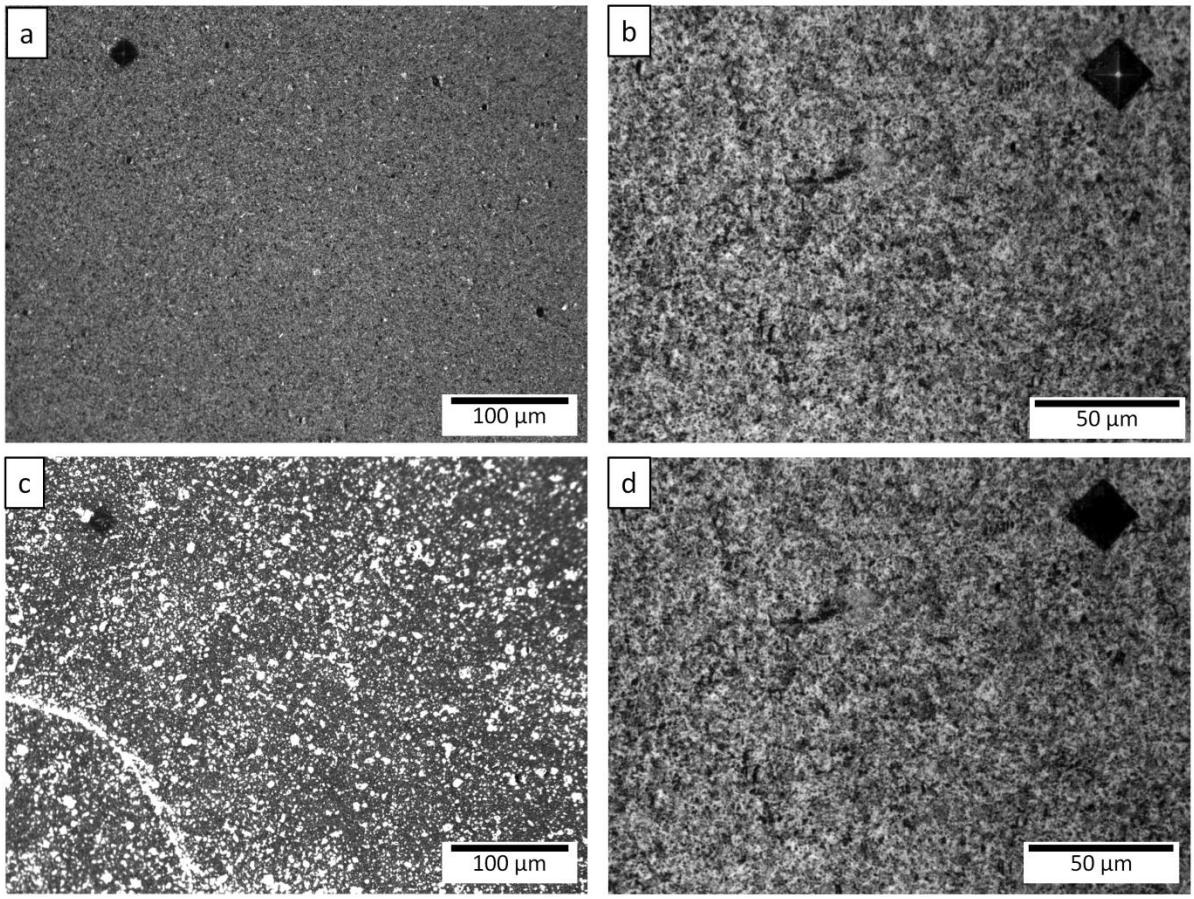

Fig. 4.1 - Speckle patterns of air blasted a) Si particles (10x magnification) and b) alumina particles (25x magnifications) before heating taken using an optical microscope. c) The pattern with the Si particles changed drastically after being heated to 800 °C while the d) alumina particle pattern remained consistent with the unheated pattern.

4.3 Experimental Procedure

The procedure outlined is for performing 2-D DIC for a material deformed under high temperature conditions. A vacuum system was employed in order to prevent oxidation which would destroy the DIC speckle pattern. Since measuring the heterogeneity of the strain field at the microstructural level was desired, a microscope has been used to capture the images. This allows for higher spatial resolution compared to previous high temperature DIC studies [15, 16]. The following section outlines the equipment used and the procedure performed.

4.3.1 Magnifications and Image Capture

An initial set of images of the sample surface with the alumina speckle pattern was taken as the DIC reference images. The five Vickers indentation marks were used to identify the area of interest. Since the DIC measurement resolution is based on the imaging magnification, consideration must be made to choose a magnification that will elucidate the desired sub-grain level measurements. A limitation to using higher magnifications was the reduced area that each image captured. In order to circumvent this issue, multiple images must be taken in order to capture the entire area of interest. In this study, the optical microscope and two magnifications described in Section 1.2.1 were used. The lower magnification used was 10x which corresponded to a scale of 0.437 μm/pix and a higher magnification of 25x which corresponded to a scale of 0.175 μm/pix. The explanation on how to handle the image array will be covered in Section 4.3.3.

4.3.2 Vacuum and Loading Procedure

After the reference images were captured, the sample was ready for the experiment. A vacuum or inert environment is necessary to safeguard against uncontrollable pattern changes once the sample is heated for testing. A vacuum chamber was utilized during this procedure to protect the sample surface from oxidation. A picture showing the vacuum chamber and load frame used during this study is given in Fig. 4.2. The load cell was moved inside the vacuum chamber in order to eliminate artificial loads due to a pressure differential, a result of the diameter of the holes at the top and bottom of the chamber being different sizes. The specimen had a type-K thermocouple spot welded onto the middle of the back once placed into the load frame. The chamber was then sealed and pulled into a vacuum of 10^{-6} Torr. Once this level was reached, which typically took pumping the system overnight, the sample was heated using induction heating at a rate of 75 °C per minute. Once the specimen had reached the desired temperature, 700 °C or 800 °C for this study, the temperature was kept to a tolerance of ± 3 °C for the duration of the deformation using a temperature controller connected to the induction heater. Temperatures higher than

the two selected presented surface damage rapidly during previous experiments. The specimen was then loaded with a servo-hydraulic load frame.

After the desired amount of deformation was reached, the system was cooled down to room temperature before returning the chamber to atmospheric pressure. This was to guarantee that there would not be any surface oxidation. The sample was then removed from the chamber and the thermocouple taken off. Images of the deformed surface were then captured with the optical microscope in the same method that the reference images were captured. The Vickers markers were used to visually identify the area of interest. It is pertinent to capture the images in the same pattern as the reference images to avoid any unnecessary post-processing changes. Once the imaging was completed, the procedure of attaching the thermocouple, pulling vacuum, heating the sample, and then deforming, if desired, was repeated.

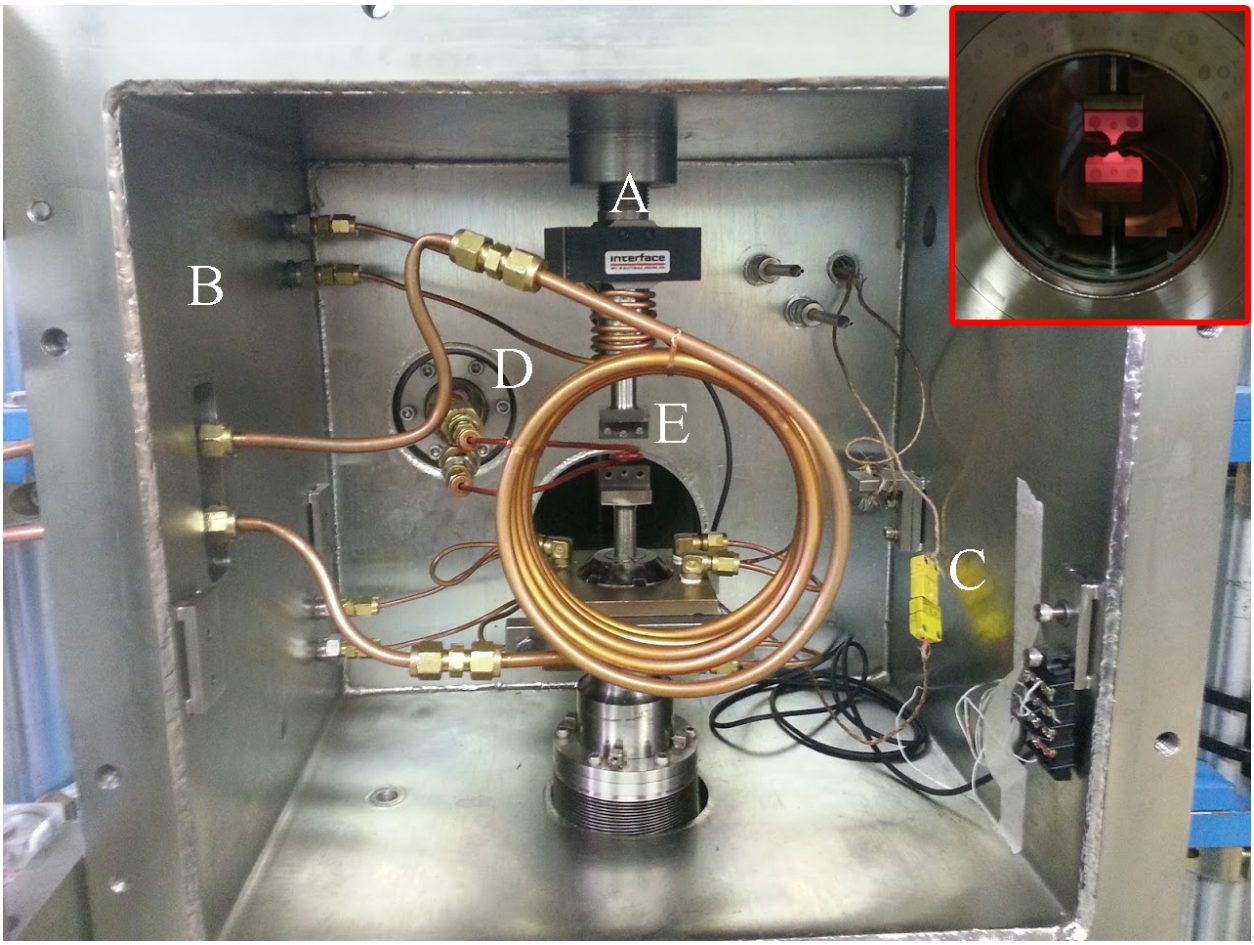

Fig. 4.2 - A picture of the experimental setup showing: A – load cell, B – vacuum chamber, C – type-K thermocouple, D – induction heating coils, and E – grips where specimen was placed. The additional copper coiling is to provide cooling during the experiments at elevated temperatures. The inset shows the specimen glowing while heated in the sealed vacuum chamber.

4.3.3 Stitching and Aligning DIC and EBSD

After deformation and image capture, the next step was to analyze the data using DIC. Since this method is an *ex-situ* technique, the strain fields found will be the residual plastic strains. There will be two methods discussed for completing this since multiple images will be required to cover the area of interest: stitching the images and stitching the DIC results.

The stitching of the images was performed with a stitching plug-in available in the open-source image processing package FIJI [17]. The plug-in uses a Fourier Shift Theorem that computes all possible translations in order to find the optimal overlapping. Each set of images stitched yields a stitched image.

The deformed images were then correlated to the reference images using Vic-2D. There are drawbacks to this technique. For instance, due to the number of images required at 25x magnification, the stitched images tend to be very large, over 100 megabytes, and this may exceed the capabilities of the correlation software. Also, the stitching seams have been found to produce artificial strains [1].

The second method to handle the image array is to perform DIC on each individual image and then combine those results as developed by Carroll *et al* [1]. Each of these images was overlapping by 40-50% to create enough overlapping data to match up the DIC results sufficiently. Deformation caused each of the strain fields to be at a slightly different location. To get a reference location for the strain fields, the reference images were stitched together using FIJI, as previously discussed, providing their original locations. Subsequently the strain fields were interpolated into an evenly spaced grid, mimicking a DIC subset grid, to produce the entire full-field strain field using these original locations. The strains were stitched to alleviate the issue of seams producing errors since this stitching occurred post-correlation. This reduced the error down to interpolation instead of artificial strains.

The final step was to align the DIC strain fields and the microstructure data from the EBSD. This was done using the Vickers marks made on the surface of the specimen at the start of the experiment. The edges of the Vickers marks are not as clear in the strain fields, thus determining their exact location and size may be difficult. The first step was to overlay each of the strain fields onto the stitched reference image since these locations are known. This was possible with software that allows layers, such as Adobe Photoshop or the open-source software GIMP. The EBSD data can then be overlaid onto the stitched reference image by aligning the Vickers marks. Manipulation of the EBSD data was required since it was skewed and possibly rotated, depending on specimen orientation differences in the SEM and optical microscope. After this was completed, the stitched reference image was removed leaving the strain fields and microstructural data aligned. An alternative method is to use a MATLAB code developed in Abuzaid's doctoral thesis [18]. This technique uses user-selected location markers based upon the Vickers marks in each set of data to scale, skew, and rotate the DIC and EBSD into alignment. It was

then possible to determine how the grain boundaries, twin boundaries, and carbides affected the strain heterogeneity. Each of the boundary types are known so it is possible to do statistical analysis such as in references [19, 20].

4.4 Measurement Error

When performing DIC, one of the major concerns is the amount of measurement error present. It was concluded in an earlier study that the image stitching technique provided a larger amount of error than the DIC stitching technique [1]. The following will cover the error determined for this experimental procedure using the images for the study in Chapter 5. The error quantification was based on the ε_{yy} strain since this was the component that will be presented.

The first step in reducing the error was to ensure that the specimen was inserted into the microscope in a consistent manner. A custom slide was designed in order to hold the specimen in the same spot and orientation each time it was placed on the microscope. The slide was designed so it could be attached to the microscope easily and was rigidly attached.

The error analysis is based on the images used for the 700 °C experiment in Chapter 5 which consists of ten tensile deformation steps. Two sets of reference images at 10x magnification were captured for the error analysis. This was done by taking one complete set of images, removing the specimen from the microscope, and then replacing the specimen and capturing the second set of images. The microscope settings (brightness, shutter speed, sharpness, etc) were kept the same. This provided a base set of two reference, stitched images in which the average strains throughout the entire experiment could be compared. Each stitched deformation image was correlated to the same area of interest on both reference images. Table 4.1 gives the comparison between the mean ε_{yy} strains found. The results showed a maximum mean error of 0.0023%. Although impressive, the local error is an important number to consider since the local strain heterogeneity is of interest. To find the local error, the entire field was analyzed for the highest strain difference between the two identical fields. The two reference images

were correlated to each other, both being undeformed, and the maximum local error was found to be two orders of magnitude higher at 0.11%. Post-experiment, the local error was determined again using the final deformation state and finding the maximum difference between correlations to each of the undeformed, reference images. The magnitude of error measured was 0.20%. It must be noted that this was determined at a region with strain over 2%.

Table 4.1 - A comparison of the DIC mean ε_{yy} strain values over the entire area of interest correlated to each of the two 10x magnification reference images.

	Reference 1	**Reference 2**	**Difference**
Step 1	0.022%	0.024%	0.0018%
Step 2	0.295%	0.297%	0.0013%
Step 3	1.061%	1.062%	0.0012%
Step 4	1.216%	1.218%	0.0020%
Step 5	1.369%	1.370%	0.0015%
Step 6	1.586%	1.587%	0.0016%
Step 7	1.872%	1.874%	0.0016%
Step 8	1.961%	1.963%	0.0020%
Step 9	2.511%	2.513%	0.0022%
Step 10	3.094%	3.096%	0.0023%

A similar error analysis was performed with the 25x magnification images. This procedure was performed with the DIC data stitching method. When comparing two undeformed sets of images, the mean ε_{yy} strain error was found to be 0.0096%. This was on the order found with the 10x magnification. The local error was found to have increased to 0.34%.

4.5 References

[1] J. Carroll, W. Abuzaid, J. Lambros, H. Sehitoglu. An experimental methodology to relate local strain to microstructural texture, Review of Scientific Instruments 81 (2010) 083703.

[2] A.S. Argon. Strengthening Mechanisms in Crystal Plasticity, Oxford University Press, Inc, New York, 2012.

[3] A.J. Wilkinson, G. Meaden, D.J. Dingley. High resolution mapping of strains and rotations using electron backscatter diffraction, Materials Science and Technology 22 (2006) 1271.

[4] S.I. Wright, M.M. Nowell, D.P. Field. A Review of Strain Analysis Using Electron Backscatter Diffraction, Microscopy and Microanalysis 17 (2011) 316-329.

[5] A. Soula, Y. Renollet, D. Boivin, J.L. Pouchou, D. Locq, P. Caron, Y. Bréchet. Analysis of high-temperature creep deformation in a polycrystalline nickel-base superalloy, Materials Science and Engineering: A 510-511 (2009) 301.

[6] K. Thibault, D. Locq, P. Caron, D. Boivin, Y. Renollet, Y. Bréchet. Influence of microstructure on local intra- and intergranular deformations during creep of a nickel-based superalloy at 700 °C, Materials Science and Engineering: A 588 (2013) 14.

[7] C. Badulescu, M. Grediac, H. Haddadi, J.D. Mathias, X. Balandraud, H.S. Tran. Applying the grid method and infrared thermography to investigate plastic deformation in aluminium multicrystal, Mechanics of Materials 43 (2011) 36-53.

[8] F. Delaire, J.L. Raphanel, C. Rey. Plastic heterogeneities of a copper multicrystal deformed in uniaxial tension: experimental study and finite element simulations, Acta Materialia 48 (2000) 1075-1087.

[9] E. Héripré, M. Dexet, J. Crépin, L. Gélébart, A. Roos, M. Bornert, D. Caldemaison. Coupling between experimental measurements and polycrystal finite element calculations for micromechanical study of metallic materials, International Journal of Plasticity 23 (2007) 1512-1539.

[10] P. Rastogi, Y. Surrel. Fringe Analysis. Photomechanics, vol. 77. Springer Berlin Heidelberg, 2000. pp. 55-102.

[11] T. Merzouki, C. Collard, N. Bourgeois, T. Ben Zineb, F. Meraghni. Coupling between measured kinematic fields and multicrystal SMA finite element calculations, Mechanics of Materials 42 (2010) 72-95.

[12] Z. Zhao, M. Ramesh, D. Raabe, A.M. Cuitino, R. Radovitzky. Investigation of three-dimensional aspects of grain-scale plastic surface deformation of an aluminum oligocrystal, International Journal of Plasticity 24 (2008) 2278.

[13] M.A. Sutton, N. Li, D.C. Joy, A.P. Reynolds, X. Li. Scanning Electron Microscopy for Quantitative Small and Large Deformation Measurements Part I: SEM Imaging at Magnifications from 200 to 10,000, Experimental Mechanics 47 (2007) 775-787.

[14] K.N. Jonnalagadda, I. Chasiotis, S. Yagnamurthy, J. Lambros, J. Pulskamp, R. Polcawich, M. Dubey. Experimental Investigation of Strain Rate Dependence of Nanocrystalline Pt Films, Experimental Mechanics 50 (2010) 25-35.

[15] J.S. Lyons, J. Liu, M.A. Sutton. High-temperature deformation measurements using digital-image correlation, Experimental Mechanics 36 (1996) 64-70.

[16] B. Pan, D. Wu, Z. Wang, X. Y. High-temperature digital image correlation method for full-field deformation measurement at 1200 °C, Measurement Science and Technology 22 (2011).

[17] S. Preibisch, S. Saalfeld, P. Tomancak. Globally optimal stitching of tiled 3D microscopic image acquisitions, Bioinformatics 25 (2009) 1463-1465.

[18] W.Z. Abuzaid. Quantitative Understanding of the Role of Grain Boundaries in Polycrystalline Deformation via Multiscale Digital Image Correlation. Mechanical Science and Engineering, vol. Ph.D. Urbana, IL: University of Illinois at Urbana-Champaign, 2012.

[19] W.Z. Abuzaid, M.D. Sangid, J.D. Carroll, H. Sehitoglu, J. Lambros. Slip transfer and plastic strain accumulation across grain boundaries in Hastelloy X, Journal of the Mechanics and Physics of Solids 60 (2012) 1201-1220.

[20] J.D. Carroll, B.G. Clark, T.E. Buchheit, B.L. Boyce, C.R. Weinberger. An experimental statistical analysis of stress projection factors in BCC tantalum, Materials Science and Engineering: A 581 (2013) 108.

Chapter 5. Incremental Tensile Experiments

The present study will focus on describing the results from incremental tensile experiments performed on Haynes 230 at 700 °C and 800 °C using the high resolution *ex-situ* technique developed in Chapter 4. The deformation was performed in increments, which will be referred to as deformation steps. The 800 °C experiment produced large scale cracking after two deformation steps. Subsequently, the 700 °C was performed and ten deformation steps were able to be produced. Strain heterogeneity, local strain concentrations, and their relations to the microstructure were the main areas of interest.

5.1 Experimental Details

Haynes 230 specimens with dimensions given in Section 1.2.2.1 were used for the experiments. The samples were prepared according to the details given in Section 4.2. The 800 °C experiment was run as a proof of method experiment for the procedure described in Chapter 4. An area of 0.6 mm by 0.6 mm was designated by Vickers marks. As noted, this sample developed cracks quickly during the experiment. The ensuing experiment was performed at 700 °C in order to produce a greater number of deformation steps before widespread cracking. Five Vickers marks were used to mark off a rectangular area of 1.05 mm by 0.525 mm for this sample. EBSD was performed in a JEOL 7000F SEM with measurement spacing of 1.0 μm. Due to the size of the area of interest, multiple EBSD scans were made. These were aligned and joined with the CHANNEL 5 software package. Fig. 5.1 shows a schematic of the sample used in the 700 °C experiment, the location of the area of interest, and the EBSD scan of the area.

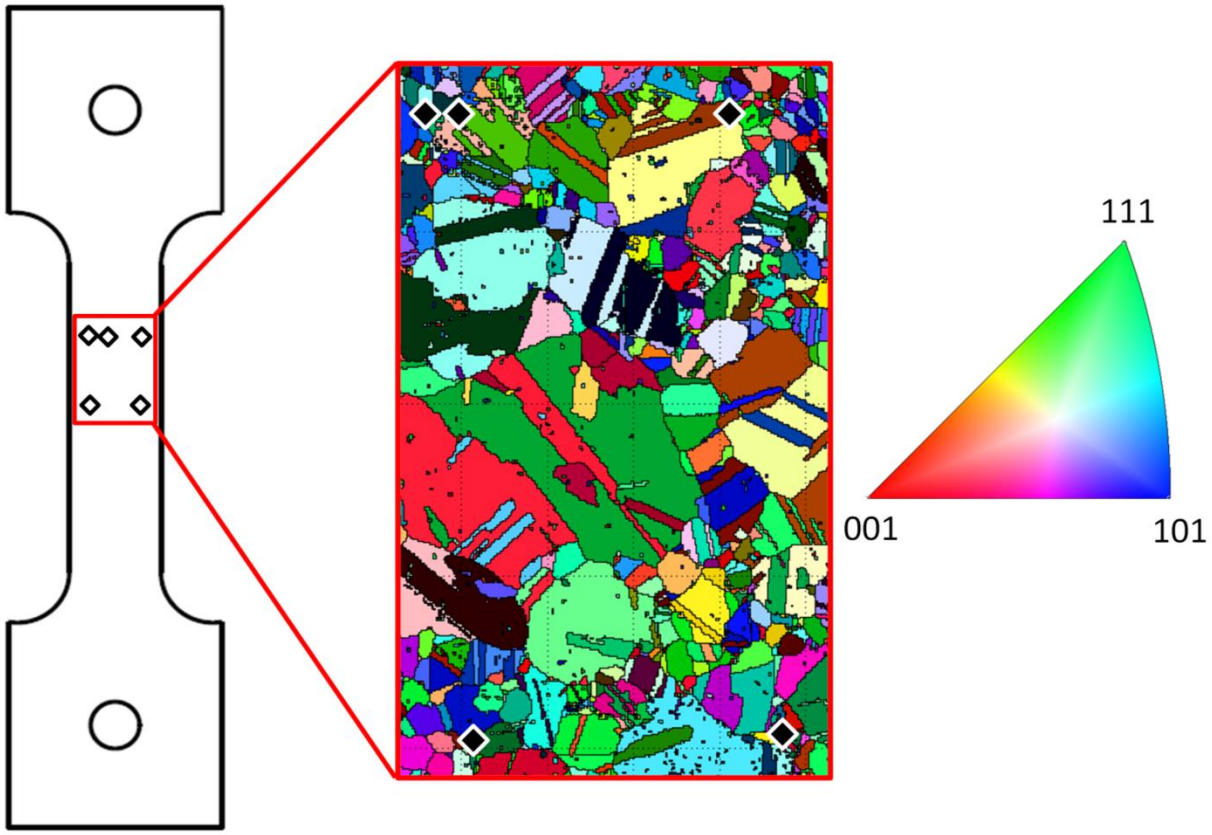

Fig. 5.1 - A schematic of the dog-bone specimen with the location of the area studied defined by the Vickers indentation marks. The EBSD scan results showing grain orientations of the 700 °C sample with the Vickers marks accentuated. The EBSD map is for an area of 1.05 mm by 0.525 mm.

Two magnifications were used. The 10x magnification was utilized to measure the average ε_{yy} and the 25x magnification was used for looking at the local strain concentrations due to its higher measurement resolution. As the most results came from the 700 °C experiment, the following will focus on that sample. In order to image the entire 1.05 mm by 0.525 mm area, three images at 10x and 27 images at 25x were needed. After the DIC speckle pattern had been applied, a set of reference images at each magnification were captured. For the 10x magnification images the image stitching technique was used while for the 25x magnification images the DIC results stitching technique was used. The samples were deformed in monotonic tension at a strain rate of 10^{-4}. For the experiment performed at 800 °C two deformation steps were made and for the 700 °C experiment ten deformation steps were made.

5.2 Results and Discussion

5.2.1 800 °C Tensile Experiment

Two steps of deformation were made at 800 °C using the experimental technique outlined in Section 2. A 51 pix by 51 pix (8.9 μm by 8.9 μm) subset size with a step of 5 pix (0.875 μm) was used for the DIC analysis. The first step was measured at a mean ε_{yy} strain of 0.8%, and the second at 5.5%. During the second step, many cracks formed on the Haynes 230 sample. These showed up as very high strains (over 15%) in DIC and thus the 5.5% of mean strain was considered to be an overestimation. The stitched reference image, stitched first step image, and the DIC results are given in Fig. 5.2a, 5.2b, and 5.2c respectively. It is clear that even with the mean strain under 1%, there was a heterogeneous strain field present. Areas with strains over 2.5% occurred throughout.

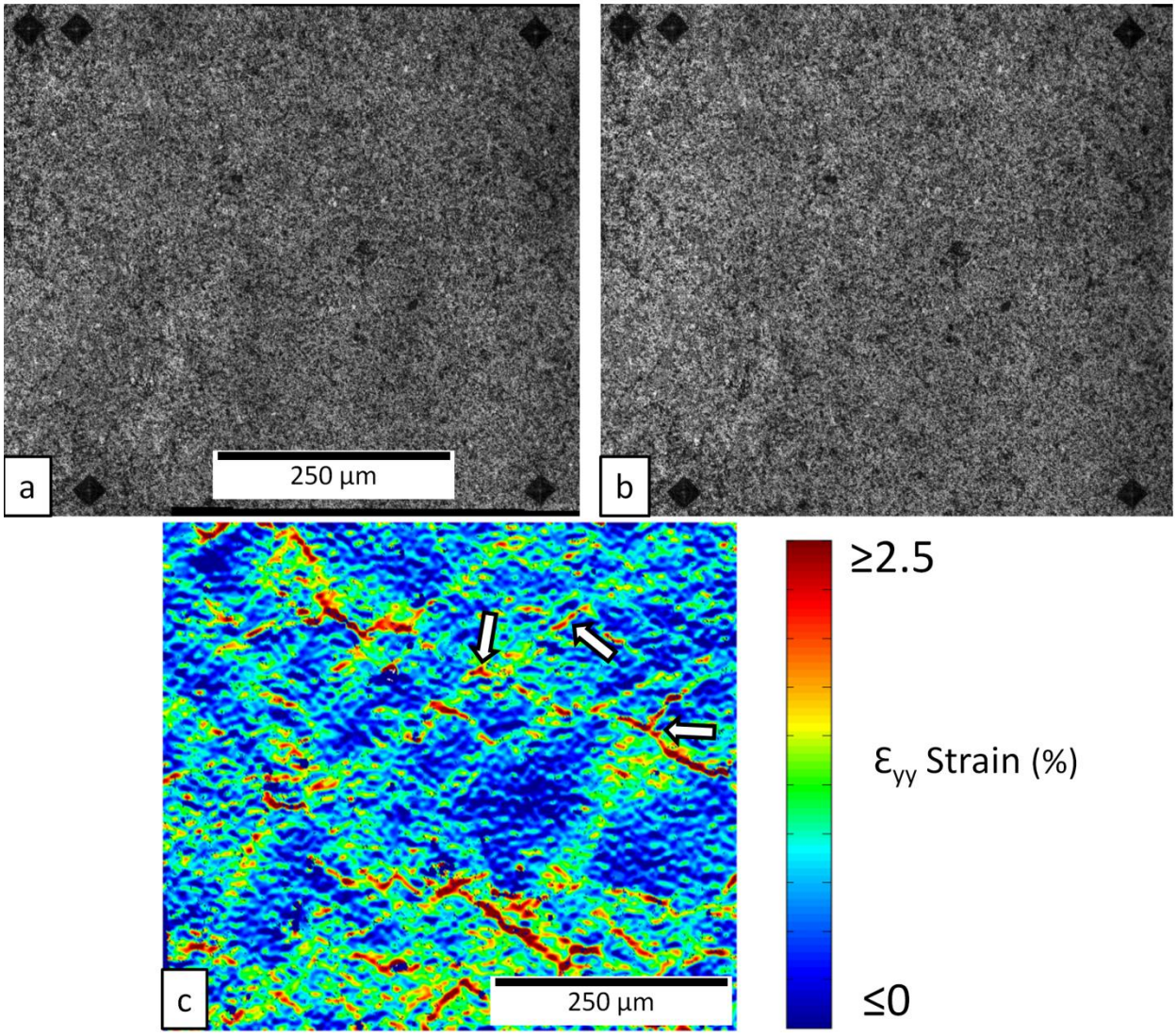

Fig. 5.2 - Images from the optical microscope showing the 0.6 mm by 0.6 mm area and speckle patterns of the sample tested at 800 °C a) undeformed and b) after the first step of heating and deformation at a magnification of 25x with the Vickers indentation marks visible. c) The ε_{yy} strain field found using DIC. The white arrows in c) show high strained areas that crack in the next deformation step (shown in Fig. 5.3c).

Due to the crack formation on the Haynes 230 sample after the second deformation step, the sample surface rose in certain areas which made it impossible to capture the complete area of interest while still in focus. This phenomenon was not present in the entire area of interest and the change in focus followed the crack paths. An example of one section is given in Fig. 5.3. In Fig. 5.3a and 5.3b, the red dotted line depicts the divide between the focuses. A simple procedure was used to resolve this issue. Capturing images at different focuses (Fig. 5.3a and 5.3b) and then combining them in software that

allows layers, such as the earlier mentioned Adobe Photoshop or GIMP, provided the base. By eliminating the areas out of focus on the top layer, an image that has full focus is obtained, as shown in Fig. 5.3c. Once this was completed, the DIC correlation was performed and the axial strain results are given in Fig. 5.3d. The red box identifies the area from Fig. 5.3c, showing the success of this technique. It must be stated that since this is a manual manipulation technique, this procedure should be limited to prevent the introduction of error or to only use the results in a qualitative manner. Comparing Fig. 5.2c and 5.3c, there was a clear correlation between the areas of high strain concentration in the first step and the eventual crack locations in the second step. Three of the high strain regions which cracked are highlighted with white arrows. A majority of these cracks were along grain boundaries.

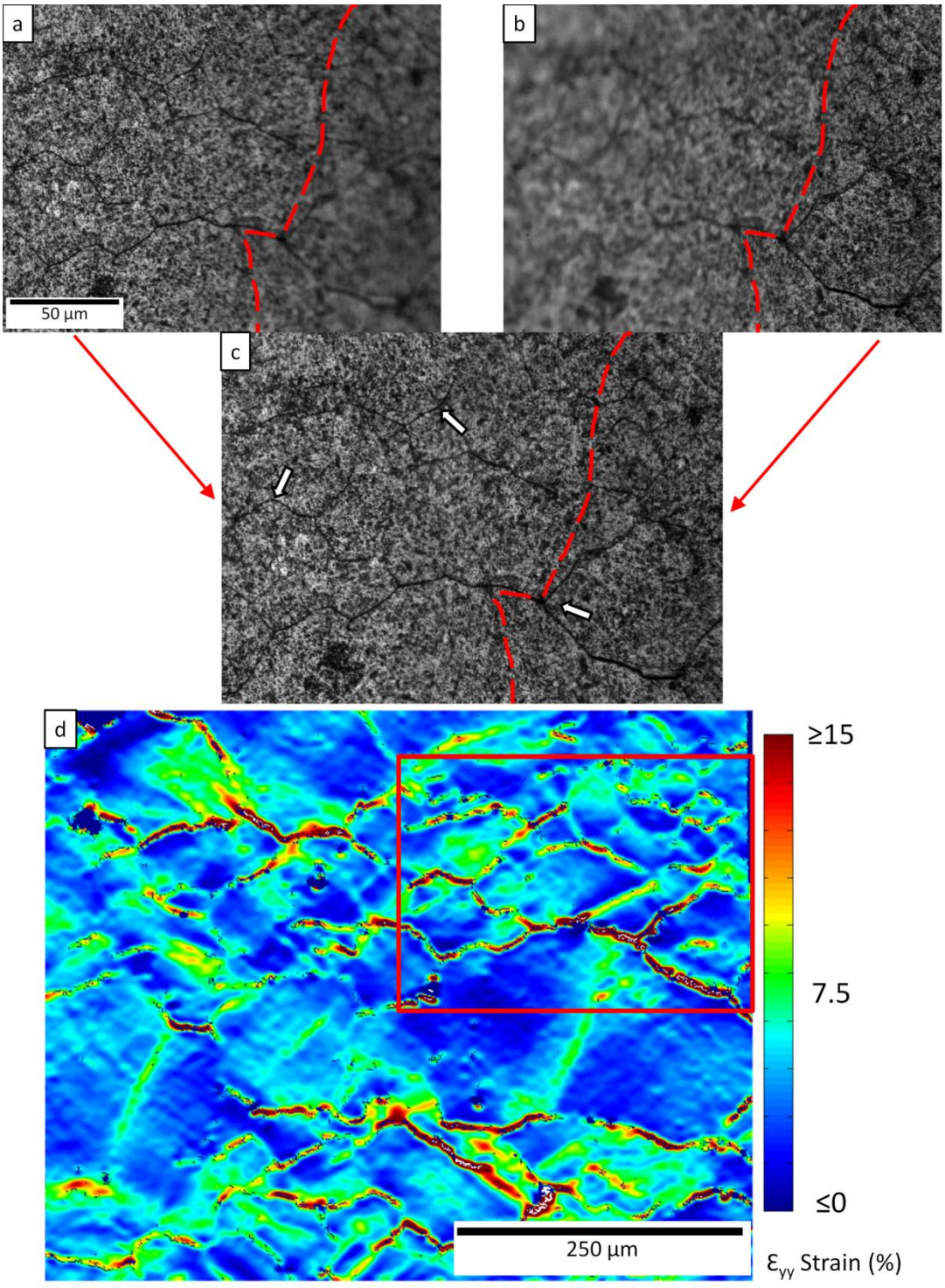

Fig. 5.3 - a) and b) Images taken with the optical microscope depicting the lack of focus in certain areas of each image. c) The combined image created using the images in a) and b) and eliminating the out of focus regions. d) The ε_{yy} strain field found using DIC with cracks on the sample showing strain magnitudes of 15% or greater. The red box is the region correlated using the image in c). The white arrows in c) show cracked regions that were the highly strained areas in the previous deformation step.

5.2.2 700 °C Tensile Experiment

This tensile experiment was performed at 700 °C and included 10 deformation steps. Two magnifications were used. The images taken at a magnification of 10x were analyzed using the image stitching technique, while the images taken at 25x magnification were analyzed using the DIC data stitching technique. The DIC analysis for the 10x magnification was performed with a 31 pix by 31 pix (13.55 μm by 13.55 μm) subset size with a step of 5 pix (2.185 μm) and the 25x magnification analysis was performed with the same subset as the 800 °C test, 51 pix by 51 pix (8.9 μm by 8.9 μm) subset size with a step size of 5 pix (0.875 μm). The reason for using the lower magnification was to be able to quickly determine the mean strains. This only required stitching 3 images together per deformation and performing the DIC analysis. The higher magnification results were used in conjunction with the microstructural data to elucidate information about its effects on the strain heterogeneity. The stress-strain curve with each of the deformation steps marked is given in Fig. 5.4a. The deformation steps in terms of the mean ε_{yy} strain were as follows: 0.02%, 0.30%, 1.06%, 1.22%, 1.37%, 1.59%, 1.87%, 1.96%, 2.51%, and 3.09%. The three DIC ε_{yy} strain fields, Fig. 5.4b-d, are the higher magnification results from the 1.22%, 1.59%, and 2.51% steps respectively. The increasing strains are obvious in Fig. 5.4 when taking into account the scales. The use of both DIC strain fields and microstructure data from EBSD provided insight into the main areas of strain concentration during the deformation.

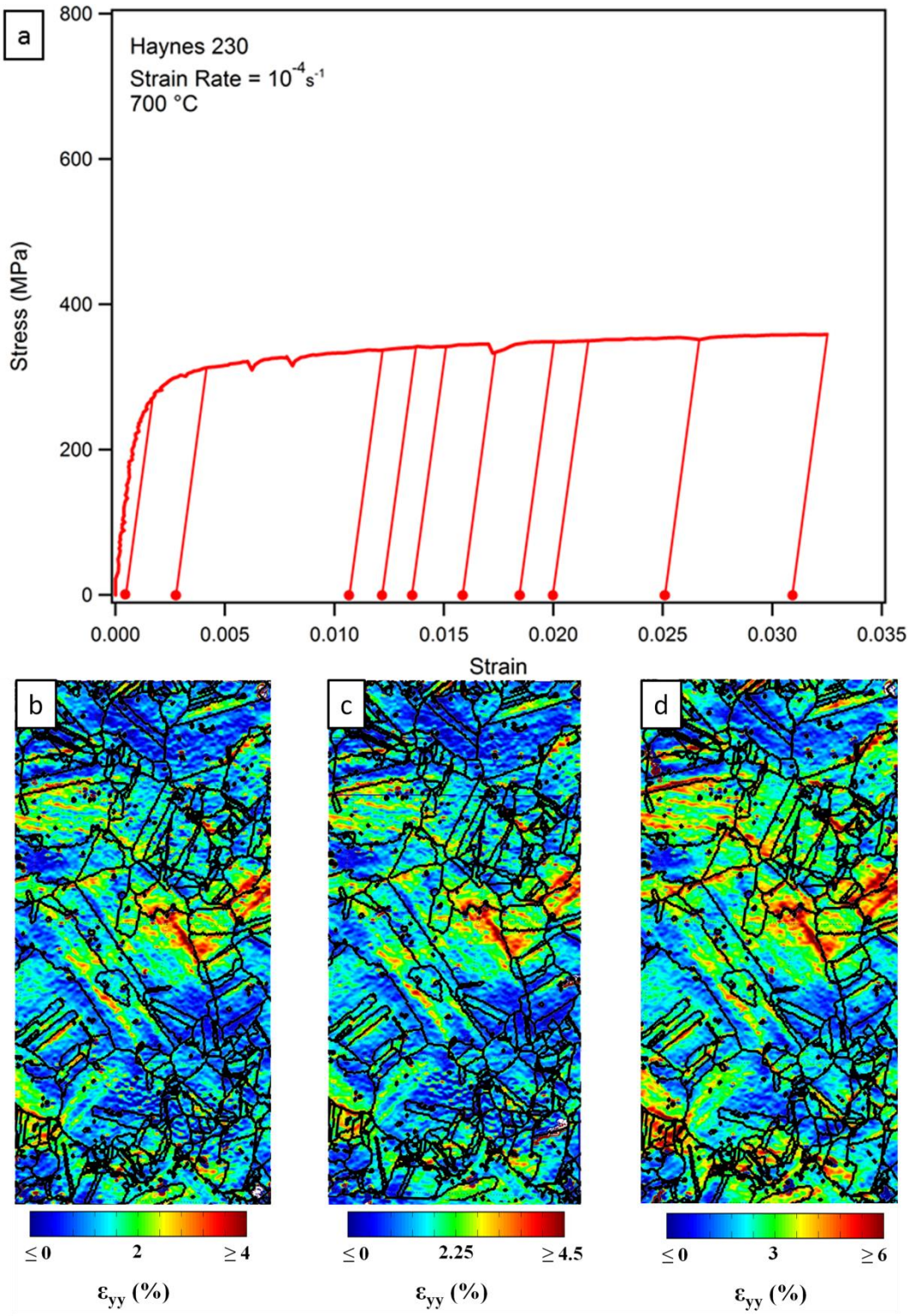

Fig. 5.4 - a) The stress-strain response of Haynes 230 experimented at 700 °C with the 10 steps of deformation indicated when the experiment was halted to image for DIC. The ε_{yy} strain field of the 1.05 mm by 0.525 mm area studied with the grain and twin boundaries overlaid at mean strains of a) 1.22%, b) 1.59%, and c) 2.51%. Note the scale bar changes for each strain field.

To quantitatively find results, the strains were analyzed globally. Fig. 5.5 presents these results. In Fig. 5.5a, a histogram depicts the changing strain values for four of the deformation steps. It is observed that there is a clear shift from a peak of concentrated values for Step 2 (mean ε_{yy} strain of 0.32%) to a broad extended distribution of strains in Step 9 (mean ε_{yy} strain of 2.53%). From this result and the heterogeneity shown in Fig. 5.4, it can be interpreted that some areas are deforming at a higher rate than others while certain areas are not deforming. A clearer picture of this is given in Fig. 5.5b which illustrates that the maximum strain is increasing at a quicker rate than the mean value. It is also noted that the minimum strain value is consistent throughout the entire experiment. The standard deviation of the ε_{yy} strain field, plotted in Fig. 5.5c, quantitatively shows the increase of heterogeneity perceived from the other figures.

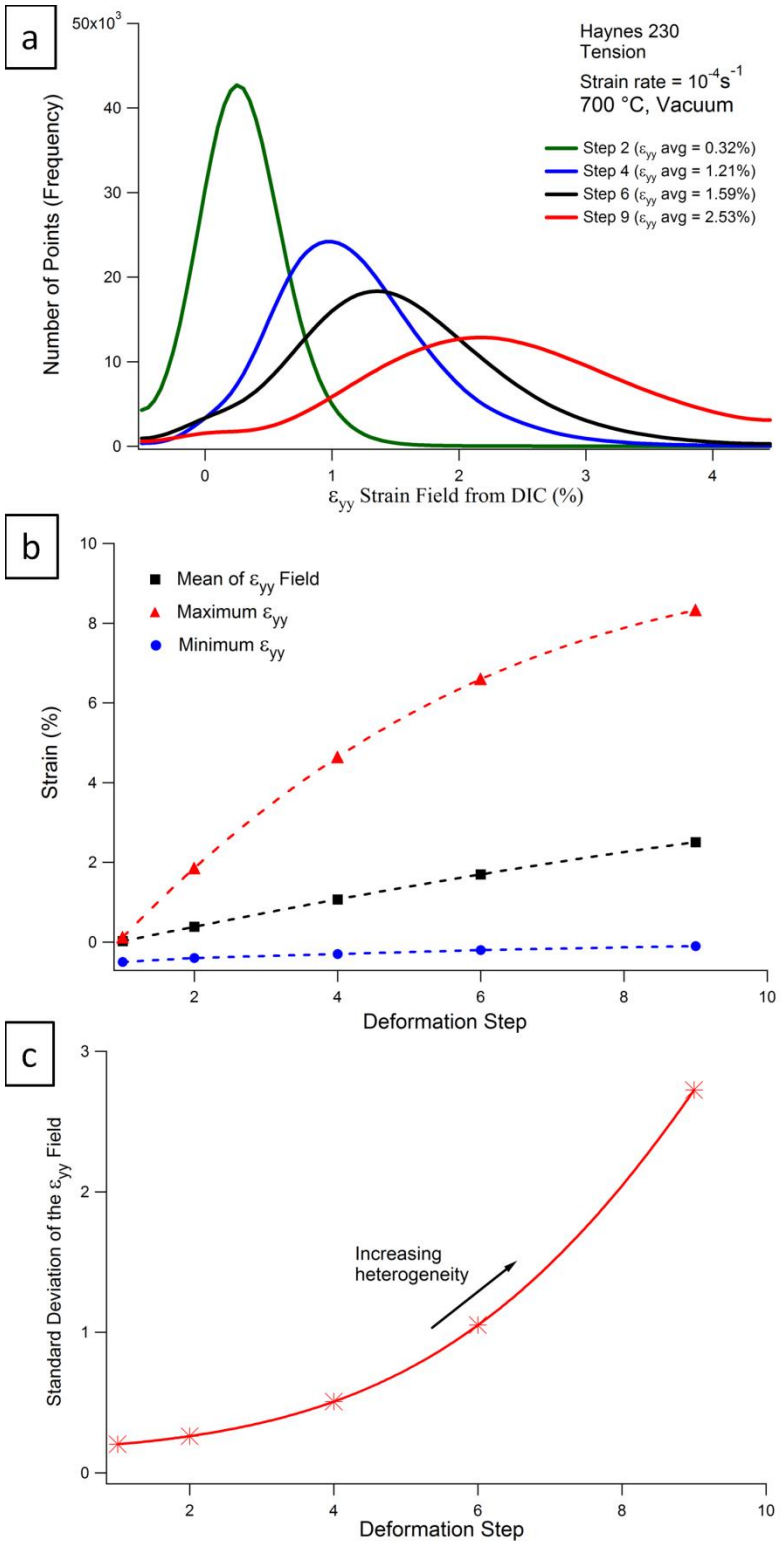

Fig. 5.5 - a) Histogram of the ε_{yy} strain values for four deformation steps showing the increasing strain values. b) The trends of the minimum, maximum, and mean values of the ε_{yy} strain field. c) The standard deviation of the ε_{yy} strain field showing an increasing heterogeneity in the strain field.

It is of value to compare these elevated temperature results to room temperature results. Previously, global trends have been measured using high resolution *ex-situ* DIC in another nickel-based superalloy, Hastelloy X [1]. Fig. 5.5 of this study will be compared to Fig. 6.3 found in [1]. The Hastelloy X experiment was performed in tension with 5 deformation steps reaching a mean ε_{yy} residual strain of 2.8%. The experiments parallel each other in terms of the experimental procedure, both being tensile experiments, and deformation to approximately 3%. The same trends are observed when comparing the histograms (Fig. 5.5a): at low average ε_{yy} strains the histogram has a high peak slightly above 0% strain; continual straining causes the histogram to flatten out and span from compressive strains to 4.5% strain and above. In both cases, there is an exponential growth in the standard deviation (Fig. 5.5c) showing both cases are undergoing high levels of strain heterogeneity. The clear differences between the elevated and room temperature cases are in the trend of the maximum ε_{yy} strain (Fig. 5.5b). In Hastelloy X, the maximum ε_{yy} trace shows a linear increase throughout the experiment in contrast to the Haynes 230 elevated temperature experiment which shows the maximum ε_{yy} approaching asymptotic behavior. It can be conjectured that the elevated temperature sample was approaching a threshold strain level in certain areas before cracking would occur. In fact, under certain highly strained GBs cracks were identified after the 10th deformation step. Local strain trends such as these could shed light onto a quantitative, physics-based approach to modeling if different grain boundaries show different threshold strain levels.

Since the EBSD data is rich with information about grain orientations and grain boundary types, it is possible to combine this with the DIC results to look at the activated slip systems. The method used can be found in [2]. For brevity only two slip systems (7 and 8) have been shown. The corresponding slip plane and slip direction for these systems are highlighted in Table 5.1. Fig. 5.6a (system 7) and Fig. 5.6b (system 8) show the results from deformation step 4. The dark blue areas (0% strain) indicate that that respective system has not been activated in the grain. The areas boxed and magnified show an annealing twin, a $\Sigma 3$ boundary using the CSL notation, inside of a grain. The Schmid factors for the twin

and grain are given in Table 5.1. Fig. 5.6a clearly shows that slip is transmitted through the grain and twin boundaries, while in Fig. 5.6b the Σ3 twin boundary blocks the slip transmission. This is important for studying crack initiation as this can determine the creation of a grain cluster when slip is transmitted or an area of strain concentration in the case of blocking. Further global analysis of this can be performed, including the relationship between strain and residual Burgers vectors [2].

Table 5.1 - Schmid factors for the 12 slip systems of the grain and twin shown in Fig. 5.7.

Slip System, α	**Slip Plane**	**Slip Direction**	**Schmid Factor (Twin)**	**Schmid Factor (Grain)**
System 1	(111)	$[1\bar{1}0]$	0.33	0.03
System 2	(111)	$[10\bar{1}]$	0.40	0.01
System 3	(111)	$[01\bar{1}]$	0.07	0.02
System 4	$(\bar{1}11)$	$[101]$	0.38	0.40
System 5	$(\bar{1}11)$	$[01\bar{1}]$	0.09	0.46
System 6	$(\bar{1}11)$	$[110]$	0.47	0.07
System 7	$(1\bar{1}1)$	$[\bar{1}01]$	0.37	0.27
System 8	$(1\bar{1}1)$	$[011]$	0.05	0.36
System 9	$(1\bar{1}1)$	$[110]$	0.33	0.09
System 10	$(11\bar{1})$	$[1\bar{1}0]$	0.46	0.19
System 11	$(11\bar{1})$	$[101]$	0.39	0.11
System 12	$(11\bar{1})$	$[011]$	0.07	0.08

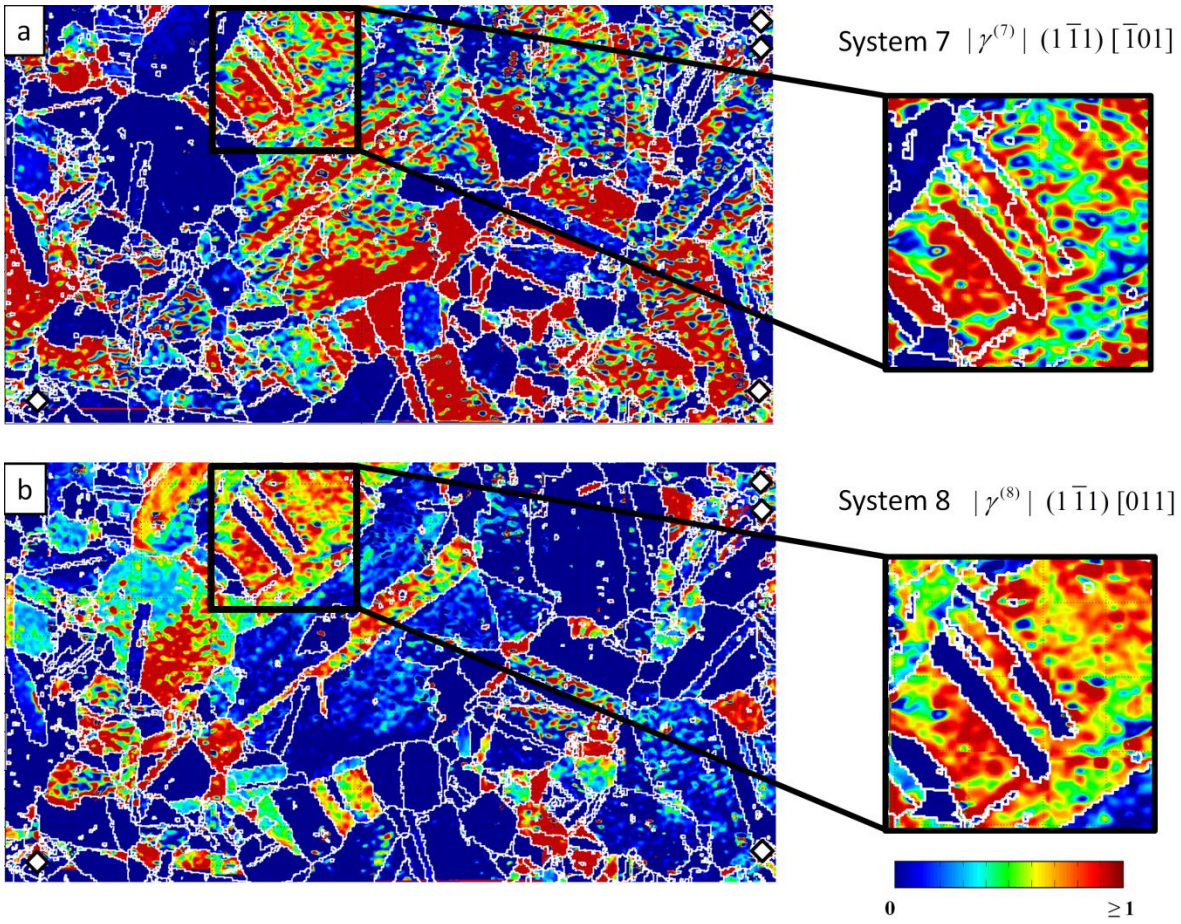

Fig. 5.6 - a) Slip system 7 and b) slip system 8 shear increments after deformation step 4. The dark blue areas are where the system has not been activated. a) Slip transmission between a grain and twin is depicted in the magnified box. b) Blockage of slip from the grain to the twin is shown in the magnified box. See Table 5.1 for the Schmid factor values.

Another part of the microstructure that must be noted is the carbides that are present in this material. Two types of carbides have been identified in several studies of Haynes 230: M_6C and $M_{23}C_6$ [3, 4]. As previously noted, the M in the M_6C carbide is assumed to be mostly the tungsten while the M in the $M_{23}C_6$ carbide is assumed to be chromium. The DIC analysis begins to show failed correlations after the third deformation step at the locations that EBSD revealed carbides. This indicates that the carbides are much more rigid than the rest of the material and play an important role in the deformation at high temperatures. In Chapter 3, it was indicated that carbides at grain or twin boundaries in Haynes 230 are likely to pin the boundary and prevent sliding reducing creep strain, but eventually will lead to a

failure of the boundary. This is a possible explanation for the large amount of strain concentrated at boundaries and the cracking observed in the 800 °C experiment. In order to glean all the information provided by this experiment, a further analysis of the grain boundary types with strain concentrations, active slip systems, and the impact on strain near carbides is required.

5.3 Summary

This study utilized a new experimental methodology for studying materials at high temperatures with high resolution digital image correlation in conjunction with microstructural data. Previous limitations of the speckle pattern changing due to the conditions in an elevated temperature environment were overcome by using stable alumina particles for a speckle pattern and preventing oxidation by experimenting in vacuum. Repeatability of this technique was proven by studying Haynes 230 under a tensile load at temperatures of 700 °C and 800 °C with multiple deformation steps. Strain heterogeneity was observed throughout along areas of slip activity, grain boundaries, and triple junctions with strains at these locations typically 2% or greater than the mean strain of the region. A comparison between this elevated temperature study and a room temperature study indicated that at elevated temperatures a critical strain level may exist at which grain boundaries fail and crack.

5.4 References

[1] W.Z. Abuzaid. Quantitative Understanding of the Role of Grain Boundaries in Polycrystalline Deformation via Multiscale Digital Image Correlation. Mechanical Science and Engineering, vol. Ph.D. Urbana, IL: University of Illinois at Urbana-Champaign, 2012.

[2] W.Z. Abuzaid, M.D. Sangid, J.D. Carroll, H. Sehitoglu, J. Lambros. Slip transfer and plastic strain accumulation across grain boundaries in Hastelloy X, Journal of the Mechanics and Physics of Solids 60 (2012) 1201-1220.

[3] L. Jiang, R. Hu, H. Kou, J. Li, G. Bai, H. Fu. The effect of M23C6 carbides on the formation of grain boundary serrations in a wrought Ni-based superalloy, Materials Science and Engineering: A 536 (2012) 37.

[4] G.J. Pataky, H. Sehitoglu, H.J. Maier. Creep deformation and mechanisms in Haynes 230 at 800 °C and 900 °C, Journal of Nuclear Materials 443 (2013) 484.

Chapter 6. Shape Memory Alloy Elastocaloric Cooling

This chapter represents a transition from the studying of Haynes 230 for the NGNP and Gen-IV initiative. The focus will be on SMAs and their temperature drop during the reverse martensitic transition. As elaborated on below, this temperature drop is due to the change of entropy during the phase change between stress-induced martensite and austenite. The schematic in Fig. 6.1 demonstrates the elastocaloric cooling phenomenon with the phase changes and their corresponding temperature changes labelled.

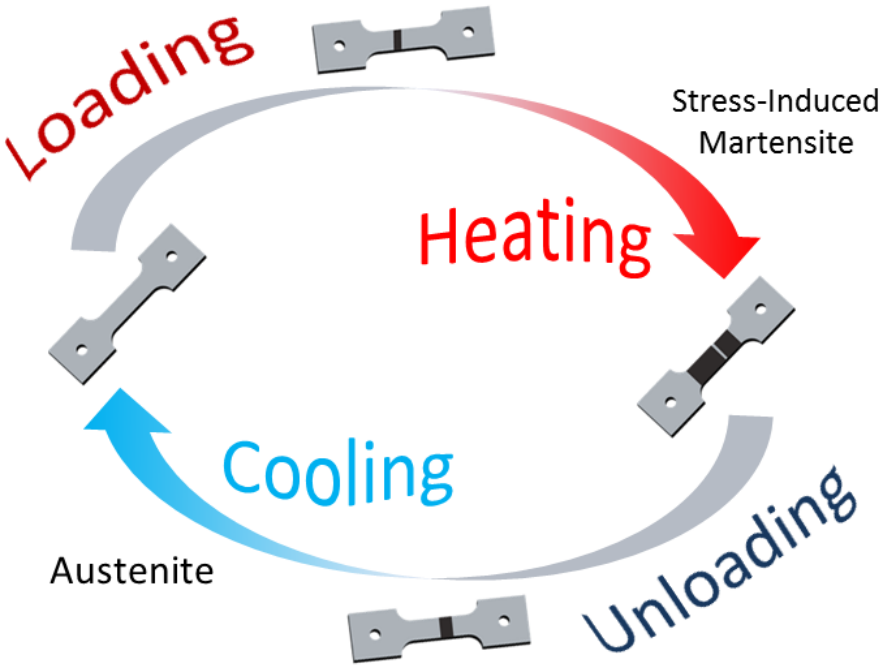

Fig. 6.1 – A schematic of the elastocaloric cooling effect. Upon loading, austenite (grey on the specimen) is transformed into stress-induced martensite (black on the specimen) and a rise of temperature is measured. Upon removal of the stress, the material returns to the austenite phase with a simultaneous large temperature drop.

6.1 Background

Solid state refrigeration technology has the potential to reduce the dependence on vapor compression for cooling and refrigeration. Vapor compression relies on refrigerants that are harmful to the environment due to their high global warming potentials (GWP), such as the common hydrofluorocarbon

(HFC) HFC-134a which has a GWP of 1,430 (100-year) [1]. The GWP indicates how much a chemical will contribute to global warming compared to the same mass of carbon dioxide. Originally, solid state refrigeration was proposed in the 1970s to take advantage of the magnetocaloric effect (MCE) [2]. Since then, much research has been carried out to maximize the potential and applications of the MCE [3]. Elastocaloric cooling in shape memory alloys (SMA) is an alternative solid state refrigeration solution without the necessity of a large magnetic field. The following study focuses on three potential SMAs to meet this demand for a practical, environmentally friendly solution.

Pseudoelastic SMAs have the ability to recover inelastic deformation upon unloading, eliminating the need to heat the material to elicit the shape memory effect [4]. This is of particular interest for elastocaloric cooling as repeated cycling without downtime is desired. In concert with the austenite to martensite transformation, during loading the exothermic stress-induced martensite transformation causes the temperature of the material to increase. When the stress is removed, a temperature decrease (ΔT) occurs due to the endothermic reverse martensitic transformation. The temperature change achieved upon unloading is due to the latent heat absorbed during the reverse martensitic transformation. Pseudoelastic SMAs avoid two issues associated with MCE: the memory effects associated with hysteresis and the narrow temperature range that limits the magnetocaloric effect [5].

The growing interest in elastocaloric cooling is evident when considering the recent increase in literature concerning the topic. Cu-Zn-Al has been featured in several studies to determine the entropy change [6], the experimental temperature change [5], and the heterogeneity of the cooling process [7]. A temperature change of 6 °C was observed in the experimental study [5]. There have also been multiple studies on the well-known SMA NiTi. NiTi wires with a diameter of 3 mm were studied and a maximum temperature change of 17 °C was observed [8]. TiNi thin films with a thickness of 20 μm were also investigated and a maximum temperature decrease of 16 °C during unloading was measured via IR camera [9, 10]. The present study was performed on NiTi, Ni_2FeGa, and CoNiAl. It is important to note

the lack of rare earth elements in all of these studies as this will decrease the cost of the alloys and elevate the usefulness of solid-state refrigeration.

The entropy of a system can be attributed to the sum of the contributions: vibrational, magnetic, and electronic entropies. Magnetic contributions are of importance for the magnetocaloric cooling effect. This study did not include magnetic fields, thus the magnetic contribution was not presently considered of importance. The next contribution, the electronic entropy, provides a significantly smaller addition to the entropy. Hence, the vibrational entropy will be the most important consideration for the elastocaloric cooling of SMAs.

In a crystalline material at finite temperature T, the vibrational modes of the lattice (phonons) contribute to the vibrational entropy S(T). An ideal SMA refrigerant (one that produces the largest ΔT) for elastocaloric cooling would maximize the entropy change: $\Delta S(T) = S_A(T) - S_M(T)$, where $S_A(T)$ is the entropy of the austenite phase and $S_M(T)$ is the entropy of the martensite phase at temperature T. If the tensile experiments are carried out under adiabatic conditions, the total entropy cannot change during the phase transition. Thus, the discrepancy $\Delta S(T)$ must be offset by an adiabatic change in temperature ΔT; physically, the temperature drops/increases as the atoms of the lattice absorb/emit phonons during their reorganization [6, 11]. As previously specified, this change from martensite to austenite will result in a decrease of temperature in the material. ΔT results from the inverse relationship between ΔS and the specific heat, C_p. Thus, it is imperative to find the SMAs which exhibit the largest ΔS with the smallest C_p. Further information concerning the ΔS of the SMAs in this study will be elaborated on in Section 6.4.2.

A dual camera combination was utilized in order to simultaneously capture images for digital image correlation while measuring the temperature of the materials. The experimental study spans across two single crystal orientations of NiTi, [148] and [112], two single crystal orientations of Ni_2FeGa, [001] and [011], and the [115] single crystal orientation in CoNiAl. The results presented include the measured

temperature change and the theoretical maximum temperature change based on the ΔS for each material and orientation. To these authors' knowledge there have been no studies on the elastocaloric cooling potential of Ni_2FeGa and CoNiAl. This study advances the current state of elastocaloric cooling information by presenting new experimental findings, including repeated cycling showing a consistent ΔT.

6.2 Experimental Details

6.2.1 Materials

The materials utilized in this study were presented in Chapter 1. For ease of referencing relevant data, the characteristic temperatures and specific heat magnitudes are repeated. For NiTi (Section 1.2.2.2), the characteristic temperature values were A_f = 0 °C, A_s = -15 °C, M_s = -55 °C, and M_f = -75 °C with a specific heat of C_p = 590 J/kg K. Ni2FeGa (Section 1.2.2.3) was found to have characteristic temperature values of A_f = 22 °C, A_s = 14 °C, M_s = 6 °C, and M_f = -3 °C with a specific heat of C_p = 460 J/kg K. The third SMA investigated, CoNiAl (Section 1.2.2.4) had characteristic temperatures of A_f = 45 °C, A_s = 22 °C, M_s = 16 °C, and M_f = 0 °C and a specific heat of C_p = 279 J/kg K.

6.2.2 Preparation and Experimental Procedure

Tensile experiments were performed on all three materials. The specimens were dog-bone shaped with a width of 3 mm, thickness of 1.75 mm, gage length of 8 mm, and total length of 26 mm. Both sides of the samples were mechanically polished with abrasive paper up to P2400 grit. One side was airbrushed with black paint in order to create a speckle pattern for DIC. The other side was painted with flat black paint to create uniform emissivity for the IR camera images.

A servo-hydraulic load frame was used for the experiments. Specimens were loaded with the speckle pattern facing a digital camera for DIC images and the solid black side facing the IR camera. The DIC camera setup was the same as described in Section 1.2.1. An area of 5 mm by 3 mm was captured with a resolution of 4.25 μm/pixel. Vic-2d was used to perform the DIC analysis. The IR camera was a closed-

cycle cooled DeltaTherm 1550 system from Stress Photonics. The system has the ability to capture images at a rate greater than 1000 fps. The system was calibrated for a temperature range of 15 °C to 115 °C by determining the intensities captured by the IR camera at known temperatures. Images captured were 320 pixels by 256 pixels. An MTS 632.29F-30 5 mm gage length extensometer was also used during the experiments. It could record strains of -10% and 30% for compression and tension respectively with an operating temperature range of -100 °C to 150 °C. The samples were loaded at a strain rate of 10^{-4} s^{-1} and unloaded at a rate of 2 x 10^{-2} s^{-1}. The faster unloading rate was used in order to approach adiabatic conditions, although not reaching them. The full loading and unloading sequence was captured by both cameras (IR and DIC).

6.3 Results

6.3.1 Stress-Strain Response

The endothermic temperature change during the reverse martensitic transformation was measured for NiTi, Ni_2FeGa, and CoNiAl. The tensile stress-strain curves for each of the five orientations are shown in Fig. 6.2. Unless noted, these experiments were conducted at room temperature. Multiple experiments were performed on each specimen in order to establish the repeatability and consistent ΔT of elastocaloric cooling. The [148] NiTi orientation was strained to 4.25% and a maximum stress of approximately 500 MPa. The [112] NiTi orientation results presented are for 4.75% strain, also a maximum stress of 500 MPa. The Ni_2FeGa experiments exhibited a much lower stress. The [011] orientation reached a maximum strain of 3.5% and maximum stress of 135 MPa, while the [001] orientation was strained to 10% with a maximum stress under 100 MPa. The CoNiAl specimen was pulled to 7.0% strain corresponding to a maximum stress of 175 MPa. The pseudoelasticity in each specimen was evident.

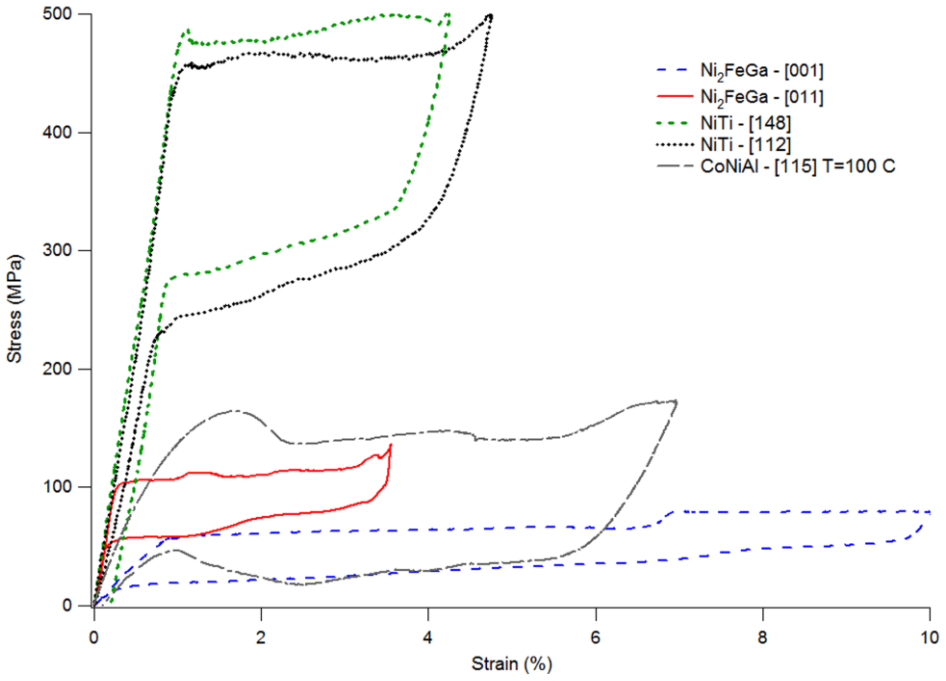

Fig. 6.2 - Tensile stress-strain curves for the shape memory alloys

6.3.2 Temperature Change

Each temperature change experiment was performed 3 to 5 times with the same maximum strain and stress. The IR camera captured the entire specimen during the experiment. The average temperature was taken over the entire gage section, and the ΔT reported was measured from the onset of unloading until the specimen was completely unloaded.

The findings of this study are presented in Fig. 6.3. This plot shows the temperature drop for each experiment performed for the 5 orientations. NiTi had the largest ΔT: 14.2 °C for the [148] orientation and 13.3 °C for the [112] orientation. For Ni_2FeGa, the [011] oriented specimen had an average ΔT of 7.6 °C and the [001] specimen had an average of 8.4 °C. The CoNiAl experiment was performed at 100 °C by heating the grips with variable heating cable and allowing the gage section of the specimen to equilibrate at the desired temperature. This specimen had the least ΔT measured, 3.1 °C. Due to the constant flux of heat into the specimen during the experiment, the ΔT measured may not reflect the true temperature change as the conditions were the furthest from adiabatic between the three materials

included in this study. These results reflect an expected finding of the ΔT being material dependent, with little dependence on the orientation, because ΔS is a material property.

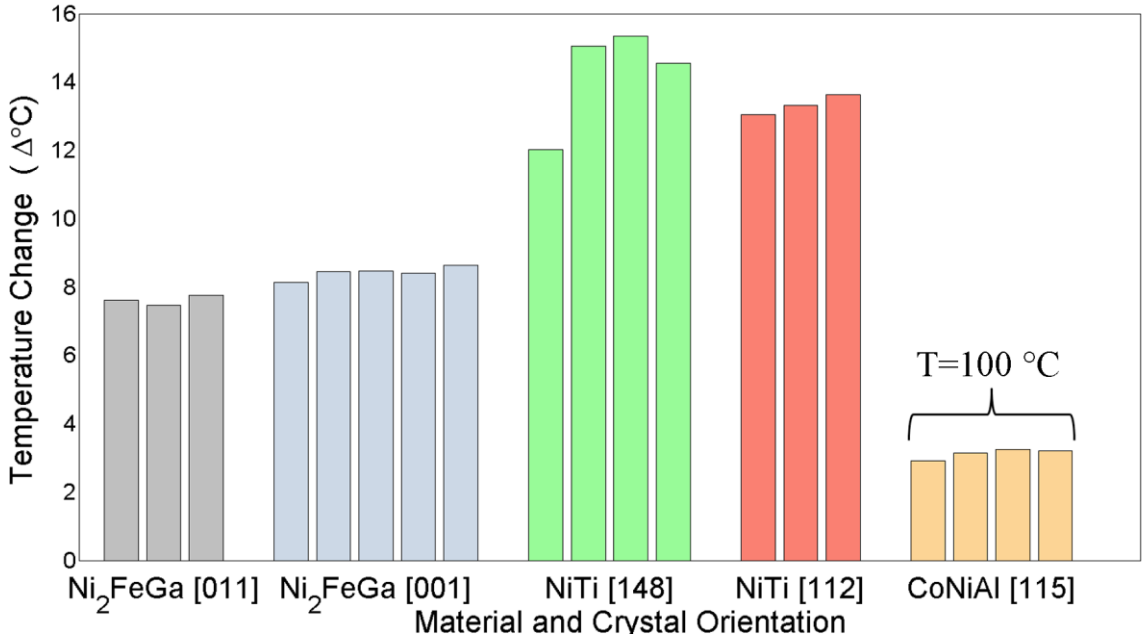

Fig. 6.3 - Temperature change, ΔT, of each experiment for each material

Additional experiments were performed to capture the ΔT of two consecutive tensile cycles. The loading parameters were kept the same as the previous results, with a maximum strain of 3.5% for the [011] oriented Ni_2FeGa specimen and 4.25% for the [148] oriented NiTi specimen. The average gage section temperature versus time plots are given in Fig. 6.4. Both specimens returned to ambient temperature between loading cycles (26 °C for Ni_2FeGa and 31 °C for NiTi) and show almost identical temperature profiles for both cycles. The small, sharp temperature increases occurring during loading represent the exothermic reactions taking place during the austenite to martensite transformations. The ΔT in both cycles corresponded to those found in the previous experiments, approximately 8 °C for Ni_2FeGa and 14 °C for NiTi.

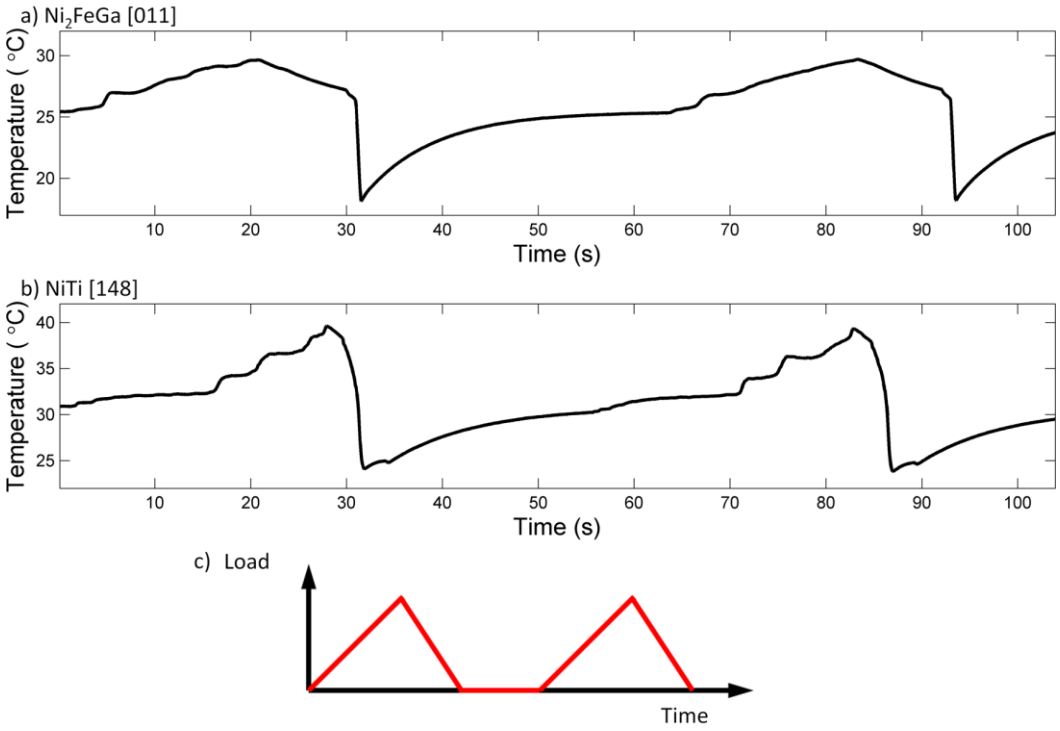

Fig. 6.4 - Temperature versus time plots for the a) [011] oriented Ni_2FeGa specimen and b) [148] oriented NiTi specimen. c) Schematic describing the experiment of two consecutive cycles with a hold period between tensile cycles.

6.3.3 Temperature Change and Strain Relationship

A large consideration must be given to the fatigue life necessary for solid state refrigeration to be viable. To meet typical refrigeration demands for 10 years, the SMAs must undergo 78 million stress-induced phase transformations [8]. Reducing the strain the material undergoes per cycle could prolong the life of the refrigerant, but the SMA must still undergo an acceptable ΔT in order act as a refrigerant. A strain versus ΔT experimental matrix was performed on the Ni_2FeGa [001] oriented single crystal. The results are shown in Fig. 6.5. A minimal ΔT was measured at 2% and less. At a maximum of 3% strain, a temperature drop of approximately 5.5 °C was measured and continued to climb linearly with a ΔT of 6.5 °C at 7% strain. Referencing Fig. 6.2, 3% strain lies in the middle of the first stress-induced martensite transformation and 7% strain is at the edge of the second stress-induced martensite. A further discussion of the implications of these results will be presented in Section 6.4.1.

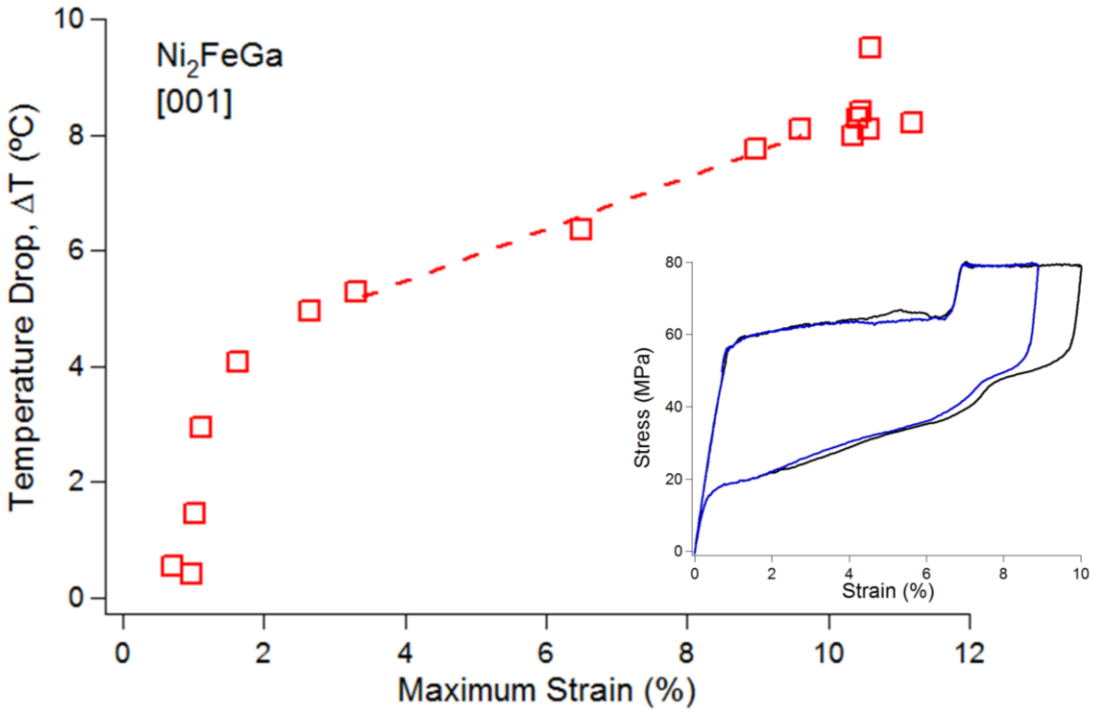

Fig. 6.5 - The temperature change, ΔT, as a function of maximum tensile strain. The inset shows the stress-strain curves for maximum strains of 8.35% and 10%

6.3.4 Transformation Bands

The dual camera experimental setup allowed for the simultaneous capture of the strain fields and the sample temperature. This capability provided a means to expound on the relationship between the transformation bands and temperature change during a tensile cycle. The stress-strain curves for the [011] oriented Ni_2FeGa specimen (Fig. 6.6a) and the [112] oriented NiTi specimen (Fig. 6.6b) with DIC strain fields and the gage section temperatures are shown in Fig. 6.6. The isolation of snapshots during the experiments provided a clearer picture of the strain and temperature evolutions.

Starting with the Ni_2FeGa specimen, the sample was at ambient temperature (approximately 29 °C) at 0% strain. As the stress-induced martensitic transformation began, a localized strain band of 4% strain was featured in the center of the gage section with indications of transformation occurring at the top of the gage section as well. The transformation band widened, with a corresponding increase of temperature in the same area, until the maximum strain was achieved and the temperature was 31 °C. Unloading

corresponded to a vertical drop of stress and the initiation of the reverse martensitic transformation, as demonstrated by the reduction in strain values. The IR camera images showed an immediate decrease in temperature of approximately 5 °C, with an area of undercooling at the location of the transformation. At the completion of unloading, the sample returned to 0% strain with a ΔT of 8.2 °C. Fig. 6.6b presents the same trends for the NiTi specimen. In the elastic regime, the specimen temperature was close to ambient temperature and temperature increases were not observed until the stress-induced martensitic transformation occurred. Two transformation bands met and combined as further straining occurred. The exothermal temperature increase was greater in the NiTi sample compared to the Ni_2FeGa sample. During unloading, reverse martensitic transformations occurred at both ends of the specimen and moved towards the middle of the specimen causing the large endothermal ΔT of 13.9 °C.

The exothermic reaction during the loading portion of the tensile cycle differed by material. The Ni_2FeGa specimen saw a maximum increase of 5 °C, but then decreased to 2 °C above ambient temperature before unloading. By contrast, NiTi saw a larger temperature increase of 7 °C during the stress induced martensitic transformation, with no subsequent drop before unloading. This corresponded to a net temperature change, ambient temperature minus minimum temperature, of only 7 °C. The differences between the average and localized temperature change are illustrated in Fig. 6.6c. The average temperature was 28.4 °C, but along the transformation bands undercooling of approximately 26 °C was observed. These areas are indicated by dotted black lines in Fig.6.5c. This discovery indicated that the reversed martensitic transformation has a very local endothermic response, and the surrounding material was dissipating heat into the transformed austenitic material.

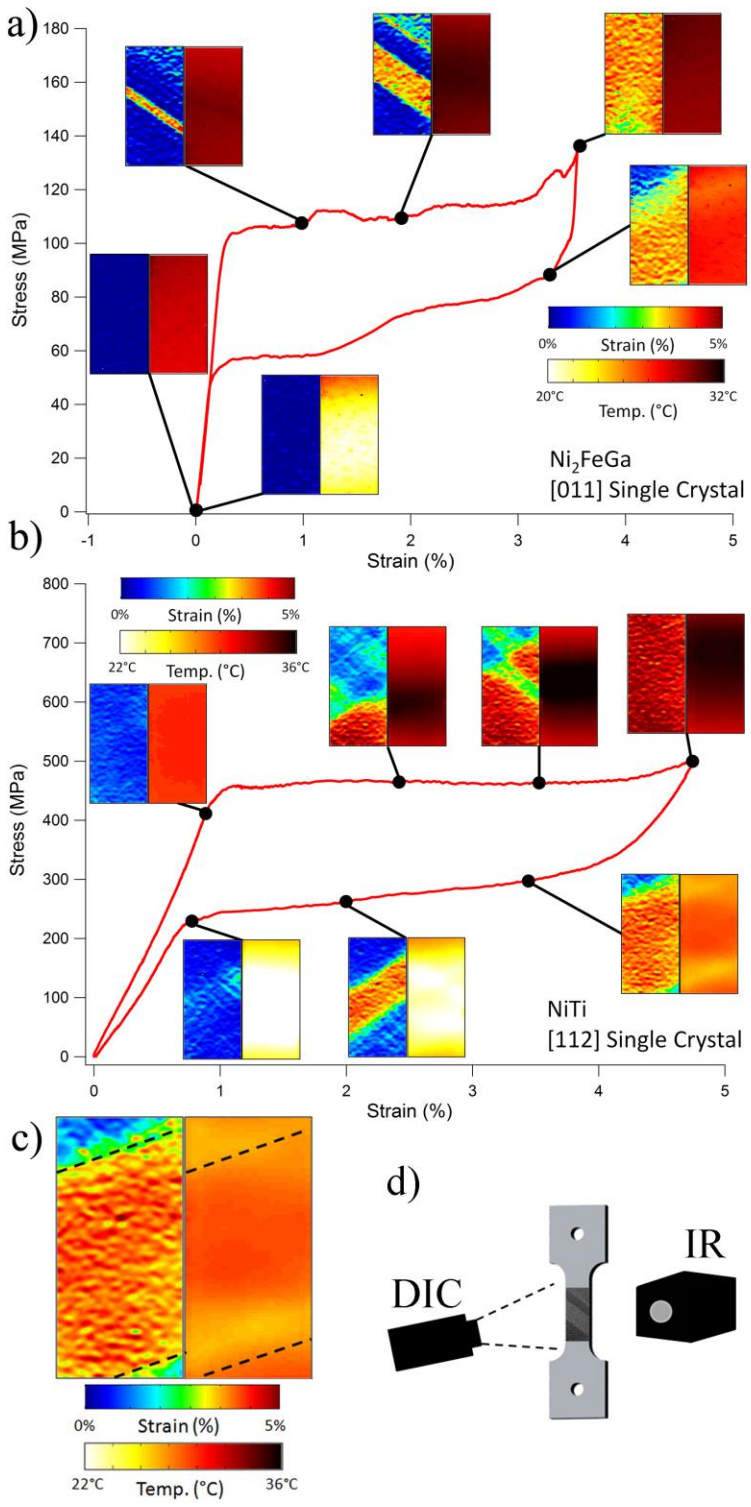

Fig. 6.6 - Tensile stress-strain curves of the a) [011] oriented Ni_2FeGa specimen and b) [112] oriented NiTi specimen with selected DIC strain fields and temperature gradient of the gage section. c) During the reverse martensitic transformation in the [148] NiTi single crystal, the transformation band edges corresponded to a localized undercooling as indicated by the dotted black lines. d) Schematic of the two camera setup with the DIC camera in front and the IR camera behind the sample.

6.4 Discussion

The results of this study contain significant findings for the furthering of elastocaloric cooling. The following section will elucidate the potential of NiTi and Ni_2FeGa for elastocaloric cooling and the ramifications of the differences between the theoretical maximum and experimentally found ΔT values.

6.4.1 Fatigue Considerations for Elastocaloric Cooling

In order to be a practical alternative to vapor compression, the longevity of the SMAs employed for elastocaloric cooling must be explored. Since NiTi has been the focus of several studies besides this one [8-10, 12-14] and yields the greatest ΔT, it will be the first material of focus. The repeatability and consistency of the ΔT shown in Fig. 6.4 are promising findings when considering that MCE has significant changes between the first and second cycles. Other researchers showed that the magnitude of the measured ΔT was reduced by approximately 3.6 °C after only 127 cycles though [12]. Initial discoveries indicated that NiTi could be the most effective SMA for elastocaloric cooling if the ΔT was stabilized, but fatigue life must also be considered. Previous studies on a similar composition, 50.8 at.% Ni, yielded fatigue lives that fall far short of those desired for an elastocaloric cooling refrigerant. The [112] orientation with a strain range, Δε, of 3% had a fatigue life of 4 cycles or 14 cycles depending on the heat treatment [15]. The same study included the [148] orientation with minimal improvement with the same strain range, 185 or 224 cycles [15]. Another study on polycrystalline NiTi with the nominal composition of 50.8 at.% Ni presented a table comparing Δε to the cycles to failure, N_f. The longest fatigue life was 13,495 cycles with a maximum strain of 0.70% and a life of only 340 cycles for a maximum strain of 4.50% [16]. Other studies also collaborate these low fatigue lives at high strains [17, 18]. The current study has found that NiTi has the largest ΔT, but the previously reported fatigue lives fall far short of the estimated 78 million stress-induced martensitic transformations required for a 10-year life as a refrigerant.

Ni_2FeGa has proven to have a much more promising fatigue life. A previous study of the exact same material showed a fatigue life of 13,579 cycles at a maximum strain of 10% for the [001] oriented crystal

and runout (over 10^7) at 3% strain [19]. It is of great importance to note that these failures were at the fillet section, thus the lower bounds of the fatigue life. In the same study, the [011] oriented specimen had a fatigue life of 6,427 cycles at a maximum strain of 1%. This presents a substantial increase in the fatigue life of Ni_2FeGa compared to NiTi. This study presents the first experimental findings concerning the ΔT of Ni_2FeGa and measurements indicated a significant magnitude. The results from Fig. 6.5 showed that a temperature change of approximately 6 °C is achievable at 4% maximum strain. This was an increase of 1% of $\Delta\varepsilon$ compared to the results in Efstathiou *et al.* that achieved runout [19]. Another advantage of Ni_2FeGa was the low stresses required to initiate transformation. The [001] orientation underwent full transformation to a maximum strain of 10% while the stresses remained under 100 MPa. The NiTi specimens both required a stress of 500 MPa to complete transformation. A further analysis of the fatigue implications needs to be investigated including changes in ΔT after repeated cycling, but preliminary results indicate that the much longer fatigue life of Ni_2FeGa points to it as a material which should receive serious consideration for future elastocaloric studies. Furthermore, this SMA does not rely on expensive and scarce rare earth metals.

6.4.2 Theoretical Temperature Change Considerations

The experimental results observed approach adiabatic conditions, but do not represent the theoretical maximum obtainable temperature change (ΔT_{th}). Two methods of measurement to find ΔT_{th} were employed. Both use the Clausius-Clapeyron relationship given in Eq. (6-1) to find ΔS, the entropy of transformation per unit volume [4].

$$-\Delta S = \frac{d\sigma}{dT}\varepsilon_0 = -\frac{\Delta H}{T_0} \tag{6-1}$$

In this expression, $\frac{d\sigma}{dT}$ is the Clausius-Clapeyron slope, ε_0 is the transformation strain, ΔH is the enthalpy of the transformation per unit volume, and T_0 is the thermodynamic equilibrium temperature

between the two phases. The quantity $\frac{d\sigma}{dT}$ describes the dependence of the critical stress required to induce martensitic transformation under tension (0.1% strain) on the orientation and temperature. Experiments were performed for each of the five orientations included in this study and the results are given in Fig. 6.7. Lattice deformation theory (LDT) was utilized to find the transformation strain for each material and orientation [20]. To find ΔT_{th}, fully adiabatic conditions were assumed and the theoretical maximum elastocaloric adiabatic temperature change was estimated using Eq. (6-2) [6].

$$\Delta T_{th} = -\frac{T}{C_p}\Delta S \tag{6-2}$$

ΔS was found using Eq. (6-1), T is the ambient temperature (the ambient temperature of each experiment was used as it varied from 25 °C to 36 °C depending on the day of the experiment), and C_p is the specific heat given in Section 6.2.1 for each material. The calculated ΔT_{th} using the Clausius-Clapeyron slope are given in Table 6.1.

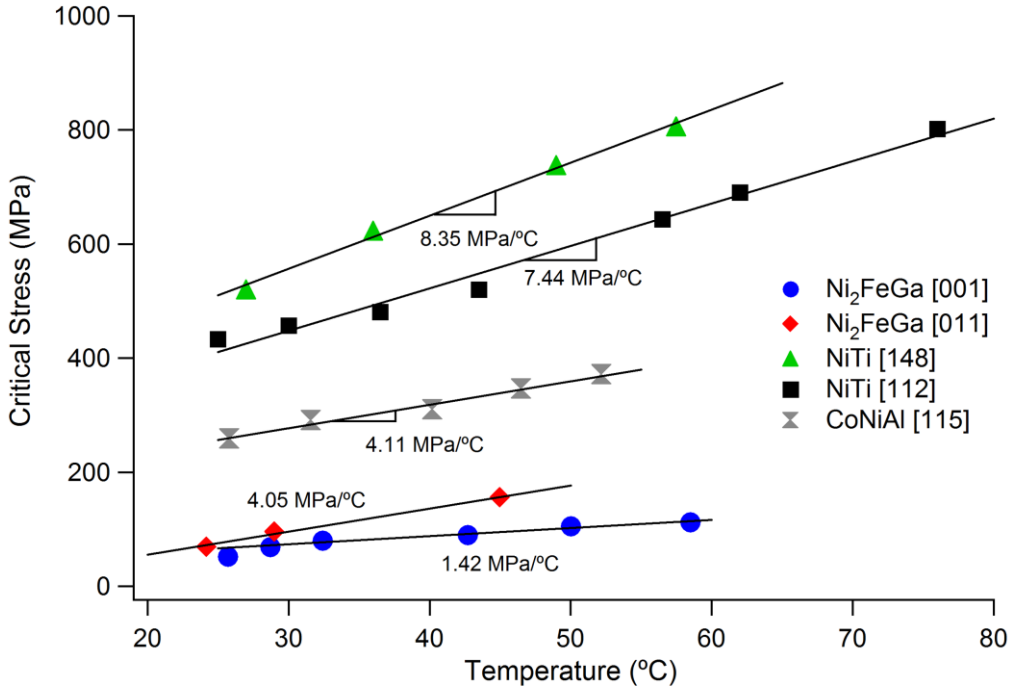

Fig. 6.7 - Critical stress (0.1% strain) as a function of temperature used to find the Clausius-Clapeyron slopes.

Table 6.1 - ΔT_{th} calculated using the Clausius-Clapeyron slope

	ε_0 (%)	dσ/dT {MPa/°C}	ΔS {J/kg-K}	C {J/kg-K}	T {K}	ΔT_{th} {K}	ΔT {K}
NiTi							
[148]	8.34	8.35	-69.64	590	303	35.76	14.2
[112]	9.5	7.44	-70.68	590	302	36.18	13.3
Ni_2FeGa							
[011]	4.1056	4.05	-16.63	460	302	10.92	7.6
[001]	14.5486	1.42	-20.66	460	309	13.88	8.4
CoNiAl							
[115]	10.71	4.11	-44.02	279	303	47.80	3.1

For the second method to find ΔS, a DSC analysis was performed on four samples of each orientation ranging from 20 mg to 60 mg by scanning at 40 °C/min, and ΔH was found by averaging the areas taken under the DSC curves. Tong and Wayman presented the accepted approximation for T_0 given in Eq. (6-3) [21].

$$T_0 = \frac{1}{2}(M_s + A_f) \tag{6-3}$$

The values of M_s and A_f were previously given for each of the materials investigated in Section 6.2.1. ΔT_{th} was calculated using Eq. (6-2) and the results using the enthalpy of the transformation are given in Table 6.2.

Table 6.2 - ΔT_{th} calculated using the enthalpy change during transformation

	T_0 {K}	ΔH {J/g}	ΔS {J/kg-K}	C {J/kg-K}	T {K}	ΔT_{th} {K}	ΔT {K}
NiTi							
[148]	245.5	12.51	-50.96	590	303	26.17	14.2
[112]	260	10.83	-41.65	590	302	21.32	13.3
Ni_2FeGa							
[011]	288.5	5.14	-17.82	460	302	11.70	7.6
[001]	281	4.51	-16.05	460	309	10.78	8.4
CoNiAl							
[115]	303.5	2.684	-8.84	279	303	9.60	3.1

As indicated in Tables 6.1 and 6.2, the theoretical maximum temperature change was higher than the experimentally found temperature change. The ΔS in Tables 6.1 and 6.2 for Ni_2FeGa were consistent with the value reported in the literature [22]. ΔT_{th} being greater than the experimentally found ΔT was consistent with other elastocaloric cooling studies. A difference of 50% was reported for Cu-Zn-Al [5] and a difference of 25% was reported for NiTi wires [8]. One explanation focuses on the unloading strain rate as it has a direct impact on ΔT. The quicker the unloading rate, the closer the experiment is to adiabatic conditions. In the study by Mañosa *et al.*, the unloading strain rate was 1.5×10^{-1} s^{-1} compared to the 2×10^{-2} s^{-1} in the current study [5].

6.4.3 Ambient Temperature Impact

The inclusion of CoNiAl in this study provided an opportunity to discover the ability of SMAs to be refrigerants in a high temperature environment. CoNiAl was experimented on at a start temperature of 100 °C with an average ΔT of 3.1 °C. Mañosa *et al.* provided a plot of the elastocaloric and magnetocaloric adiabatic temperature changes as a function of temperature [5]. At 100 °C, only gadolinium, a rare earth element, was reported as having a measured temperature change. The ΔT was

stated at approximately 1 °C. This showed that CoNiAl provides a much more viable cooling option in high temperature situations compared to other reported materials.

In addition to the ability to have a significant ΔT, it is desired that a material has a minimal exothermal reaction during the stress induced martensitic transformation, or at the very least one that is dissipated rapidly. In this study, NiTi had the highest measured temperature rise. As a refrigerant, an increase of temperature is a disadvantageous trait for a material. Ni_2FeGa had a minimal increase compared to NiTi with a chronicled longer fatigue life. Further studies on the impact of environmental temperatures need to be performed for both of these alloys in order to compare their ΔT to that of CoNiAl.

6.5 Summary

- An experimental study was carried out on three SMAs in order to measure the adiabatic temperature change. The ΔT was measured experimentally for the first time in Ni_2FeGa (average 8 °C) and CoNiAl (average 3 °C). NiTi measured the highest average ΔT of 14 °C.
- This study identifies a new potential elastocaloric refrigerant, Ni_2FeGa, and underscores its potential advantages for long term operations.
- The ΔT of two consecutive tensile cycles was recorded and the temperature profiles showed a symmetric, consistent temperature change.
- Simultaneous DIC and IR camera measurements during the tensile cycling of SMAs indicated that the reverse martensitic transformations exhibited a localized temperature undercooling.

6.6 References

[1] G.J.M. Velders, D.W. Fahey, J.S. Daniel, M. McFarland, S.O. Andersen. The large contribution of projected HFC emissions to future climate forcing, Proceedings of the National Academy of Sciences 106 (2009) 10949-10954.

[2] G.V. Brown. Magnetic heat pumping near room temperature, Journal of Applied Physics 47 (1976) 3673-3680.

[3] A.M. Tishin, Y.I. Spichkin. The Magnetocaloric Effect and its Applications, Taylor & Francis, 2003.

[4] K. Otsuka, C.M. Wayman. Shape Memory Materials, Cambridge University Press, 1998.

[5] L. Mañosa, S. Jarque-Farnos, E. Vives, A. Planes. Large temperature span and giant refrigerant capacity in elastocaloric Cu-Zn-Al shape memory alloys, Applied Physics Letters 103 (2013).

[6] E. Bonnot, R. Romero, L. Mañosa, E. Vives, A. Planes. Elastocaloric Effect Associated with the Martensitic Transition in Shape-Memory Alloys, Physical Review Letters 100 (2008) 125901.

[7] E. Vives, S. Burrows, R.S. Edwards, S. Dixon, L. Mañosa, A. Planes, R. Romero. Temperature contour maps at the strain-induced martensitic transition of a Cu-Zn-Al shape-memory single crystal, Applied Physics Letters 98 (2011).

[8] J. Cui, Y. Wu, J. Muehlbauer, Y. Hwang, R. Radermacher, S. Fackler, M. Wuttig, I. Takeuchi. Demonstration of high efficiency elastocaloric cooling with large ΔT using NiTi wires, Applied Physics Letters 101 (2012).

[9] H. Ossmer, C. Chluba, B. Krevet, E. Quandt, M. Rohde, M. Kohl. Elastocaloric cooling using shape memory alloy films, Journal of Physics: Conference Series 476 (2013).

[10] H. Ossmer, F. Lambrecht, M. Gültig, C. Chluba, E. Quandt, M. Kohl. Evolution of temperature profiles in TiNi films for elastocaloric cooling, Acta Materialia 81 (2014) 9.

[11] X. Moya, S. Kar-Narayan, N.D. Mathur. Caloric materials near ferroic phase transitions, Nature Materials 13 (2014) 439-450.

[12] C. Bechtold, C. Chluba, R. Lima de Miranda, E. Quandt. High cyclic stability of the elastocaloric effect in sputtered TiNiCu shape memory films, Applied Physics Letters 101 (2012).

[13] J. Cui. Shape Memory Alloys and Their Applications in Power Generation and Refrigeration. MRS Online Proceedings, vol. 1581: Cambridge Journals Online, 2013.

[14] K. Mukherjee, S. Sircar, N.B. Dahotre. Thermal effects associated with stress-induced martensitic transformation in a Ti-Ni alloy, Materials Science and Engineering 74 (1985) 75.

[15] K. Gall, N. Yang, H. Sehitoglu, Y. Chumlyakov. Fracture of precipitated NiTi shape memory alloys, International Journal of Fracture 109 (2001) 189-207.

[16] C. Maletta, E. Sgambitterra, F. Furgiuele, R. Casati, A. Tuissi. Fatigue of pseudoelastic NiTi within the stress-induced transformation regime: a modified Coffin-Manson approach, Smart Materials and Structures 21 (2012).

[17] G. Eggeler, E. Hornbogen, A. Yawny, A. Heckmann, M. Wagner. Structural and functional fatigue of NiTi shape memory alloys, Materials Science and Engineering: A 378 (2004) 24.

[18] K.N. Melton, O. Mercier. Fatigue of NITI thermoelastic martensites, Acta Metallurgica 27 (1979) 137.

[19] C. Efstathiou, H. Sehitoglu, P. Kurath, S. Foletti, P. Davoli. Fatigue response of NiFeGa single crystals, Scripta Materialia 57 (2007) 409.

[20] T. Saburi, S. Nenno. The shape memory effect and related phenomena, Solid to Solid Phase Transformations (1981) 1455-1479.

[21] H.C. Tong, C.M. Wayman. Characteristic temperatures and other properties of thermoelastic martensites, Acta Metallurgica 22 (1974) 887.

[22] Y.I. Chumlyakov, I.V. Kireeva, E.Y. Panchenko, E.E. Timofeeva, Z.V. Pobedennaya, S.V. Chusov, I. Karaman, H. Maier, E. Cesari, V.A. Kirillov. High-temperature superelasticity in CoNiGa, CoNiAl, NiFeGa, and TiNi monocrystals, Russian Physics Journal 51 (2008) 1016-1036.

Chapter 7. Conclusions and Future Work

This work consisted of studying phenomena related to the deformation of two types of materials. Haynes 230 was studied at elevated temperatures and an emphasis was made to relate deformation to the microstructure. The recognized phenomenon of phase transformations in SMAs was examined for a potentially new use. This section will report the conclusions from the work reported.

7.1 Conclusions

Three distinct loading conditions at elevated temperatures and their effects on Haynes 230 were examined during this work. The elevated temperatures consisted of 700 °C, 800 °C, and 900 °C. Although a set design temperature has yet to be designated, it has been established that the minimum outlet temperature of the IHX in the VHTR will be up to 100 °C. Distinct differences in the material behavior at these temperatures were identified during this work.

A propagating crack in a component that is part of a nuclear plant is a serious concern due to the potential catastrophic consequences. Using room temperature fatigue crack growth rates as a baseline, the fatigue crack growth rates at 900 °C were measured to be an order of magnitude higher, up to rates of 10^{-2} (mm/cycle). Two distinct areas were investigated: the wake of the crack and the area in front of the crack tip. Crack closure was investigated and determined to be consistent between the two temperatures, eliminating any notions of oxide-induced closure. The role of microstructure is manifested through the irreversibility of slip at the crack tip as dislocations emitted during forward loading and interacting with other microstructural features do not completely return upon loading reversal. A quantification of this was made by measuring strain irreversibility which is directly related to slip irreversibility. The strain irreversibility in the reverse plastic zone was measured using digital image correlation and values an order of magnitude greater were measured in the 900 °C sample compared to the room temperature sample.

In the second study of Haynes 230, creep was investigated at 800 °C and 900 °C. Both *in-situ* and *ex-situ* experiments were performed. The *in-situ* experiments were used to measure the creep strains

and then determine the minimum creep rates. By comparing the minimum creep rates, it was determined that the 800 °C creep rate limiting mechanism was dislocation climb (n ~ 5) while the 900 °C mechanism was synonymous with the solute drag mechanism (n ~ 3). To further understand the microstructure's role, an *ex-situ* experiment was performed at 900 °C with a stress of 50 MPa. The experiments were halted at 2 hours and 10 hours and similar areas of strain concentrations were identified: triples junctions and serrated grain boundaries. The triple junctions were found to have a larger strain increase, ~1.0% to ~3.0%, compared to the serrated grain boundaries (~1.0% to ~2.0%). The serrated grain boundaries restrict failure by preventing grain boundary sliding until a critical strain level has developed compared to triple junctions which are the stimulus for void formation and growth. Increasing the $M_{23}C_6$ carbides through solutionizing treatments could potentially increase the life of Haynes 230.

In order to use microstructural information from EBSD, a high resolution *ex-situ* technique was developed for deformation at high temperatures. Previous issues with speckle pattern degradation due to the elevated temperature environment were eliminated by utilizing a vacuum chamber and selecting alumina to air blast onto the specimen surface. Two tensile experiments on Haynes 230 were performed with this technique: one at 700 °C and another at 800 °C. Global strain trends from the sample deformed at 700 °C were compared to room temperature results of Hastelloy X. The maximum strain trend indicated a critical strain level before cracking may be present. Strain heterogeneity was present from the onset of the experiment and details about activated slip systems were discussed.

In the final study of this work, three shape memory alloys, which demonstrated pseudoelasticity, were investigated in order to measure their temperature change during the reverse martensitic transformation. NiTi had the largest temperature change (ΔT~14 °C), but its poor fatigue properties will limit its usefulness. Ni_2FeGa, an alloy with a proven long fatigue life, was measured to have a significant temperature drop as well (ΔT~8°C). The CoNiAl experiment was at a temperature of 100 °C. It had the highest measured temperature drop (ΔT~3°C) at 100 °C currently recorded in the literature. Consecutive tensile cycles revealed a nearly symmetric temperature profile for all specimens included. The

temperature changes were found to be a local phenomenon as undercooling was measured at the edges of transformation bands by comparing IR thermography and DIC.

A resounding theme in this work has been to relate elevated temperature deformation to microstructural phenomena. Slip irreversibility has been quantified through strain irreversibility at the tip of a fatigue crack; local strain concentrations at serrated grain boundaries and triple junctions have been measured; an elevated temperature technique was developed and performed on tensile experiments for sub-grain level strain measurements to shed light on the role of boundaries. Each of the studies in this work has had the goal to advance the development of physics-based models by providing new insight into materials behavior for the scientific community. To aid in development of new alloys, suggestions have been made. For elastocaloric cooling, established shape memory alloys were investigated to determine baseline temperature change magnitudes. With the theoretically maximum temperature changes calculated, further work can be performed to develop near adiabatic techniques.

7.2 Future Work

The work in this thesis has generated several new possible avenues for future research, some of which are currently being pursued. The techniques established and data measured have advanced the scientific community's knowledge, but further investigations can answer specific research questions and will be discussed.

The high resolution techniques being developed, such the one included in Chapter 4, provide valuable information concerning the local deformation behavior with respect to the microstructure. The current downside to 2-D DIC is that it is purely a surface measurement. The grains identified at the surface may only be a few microns deep, and the third dimension orientation and shape are not known. Since the ultimate goal is to develop accurate physics-based models, this becomes a significant issue. A common modeling technique is to create columnar grains. Although many successfully studies have been produced with this method, it is unrealistic for most materials. By combining the current DIC surface

techniques and using serial sectioning to establish a complete understanding about the microstructure, a further refinement between experiments and models can be established.

To elaborate on this, tensile stages have been developed to allow for running *in-situ* DIC experiments inside of an SEM or under an optical microscope. There are two important opportunities present with these tensile stages. First, the *ex-situ* high resolution techniques can be adopted and used for *in-situ* experiments. This will provide a much greater measurement resolution and produce more accurate analyses. For example, the noise level in the room temperature fatigue crack growth experiment (Chapter 2) was on the order of the strain irreversibility measurements. Increasing the magnification and capturing a higher detailed strain field, the strain irreversibility magnitudes at a fatigue crack tip will then be able to be quantified with a greater confidence. Linking microstructural data to these strain fields also opens up the ability to quantify the fatigue crack growth rates compared to specific grain (or twin) boundaries. This could be a significant achievement in terms of material development as materials could be modified through grain boundary engineering to increase the life of a component for damage tolerant designs.

The second advantage of the SEM stages is for immediately serial sectioning a sample after deformation has been recorded. EBSD will be performed on the sample surface as it is in the current techniques. Images captured with the SEM during deformation can be used for DIC to determine the displacements. After this is completed, if the ability is present, a FIB inside an SEM can immediately remove a predetermined amount of material and EBSD performed again. This will be performed until a certain depth is achieved, or the entire sample has been scanned. This will immediately overcome the current disadvantage of not knowing what is beneath the specimen surface. In order to improve the state of current physics-based models, it is necessary to then feed in this complete collection of data about a specimen, instead of the assumption of columnar grain, to improve predictive capabilities.

The final recommended future work concerns the use of SMAs for elastocaloric cooling. A few studies in the literature have identified a change in the temperature drop after continual cycling. The study in this thesis performed at most 10 cycles on single sample. No significant changes were observed

but after 100s or 1000s of cycles, the temperature change could drastically be reduced. By performing experiments and measuring the temperature every 100 cycles, a temperature profile versus cycles can be constructed and SMAs with adequate results can move forward in terms of being candidate solid state refrigerants. This must also be a concern for tailoring SMAs to have the greatest entropy change. Temperature change will be maximized when alloys with a greater entropy change are identified. During these material developments, long fatigue life and temperature change stability (which will be related to residual martensite) are necessities.

Appendix: Least Squares Regression

The least squares regression used during this study utilized the vertical DIC displacements to find the effective stress intensity factors. This was an ideal analysis technique as it was based off the unadulterated experimental data. Crack closure effects were inherently included in the analysis, because the crack opening displacements were influenced by any crack closure phenomena present. Only the vertical displacements were used since the crack only opened in the tensile, mode I manner.

The vertical displacements as a function of the mode I stress intensity factor, K_I, T-stress, and rigid body motion for plane stress are

$$v = \frac{K_I}{\mu}\sqrt{\frac{r}{2\pi}}\sin\left(\frac{\theta}{2}\right)\left[\frac{1}{2}\left(\frac{3-\nu}{1+\nu}\right)+1-\cos\left(\frac{\theta}{2}\right)\right]-\frac{1}{2\mu}\left(\frac{\nu}{1+\nu}\right)Tr\sin(\theta)+Ar\cos(\theta)+B \quad \text{(A.1)}$$

where A is the rigid body rotation coefficient, B is the rigid body translation coefficient, T is the T-stress term, r is the distance from the crack tip, θ is the angle from the crack line ahead of the tip, ν is Poisson's ratio, and μ is the shear modulus. Thousands of vertical displacements, v, for each level of the load were known from the DIC correlations at their specific locations given by r and θ. The shear modulus and Poisson's ratio were known for the material at each temperature. A least squares regression was then employed to find the four unknowns (K_I, T, A, and B). Details of a similar least squares approach are given in [1,2].

References

[1] S.R. McNeill, W.H. Peters, M.A. Sutton, Estimation of stress intensity factor by digital image correlation, Engineering Fracture Mechanics, 28 (1987) 101.

[2] J. Carroll, C. Efstathiou, J. Lambros, H. Sehitoglu, B. Hauber, S. Spottswood, R. Chona, Investigation of fatigue crack closure using multiscale image correlation experiments, Engineering Fracture Mechanics, 76 (2009) 2384.